

Review Article

Review on field assisted metal additive manufacturing



Chaolin Tan ^{a,1}, Runsheng Li ^{b,1}, Jinlong Su ^{a,*}, Dafan Du ^{c,**}, Yang Du ^{d,***}, Bonnie Attard ^e, Youxiang Chew ^a, Haiou Zhang ^f, Enrique J. Lavernia ^g, Yves Fautrelle ^h, Jie Teng ⁱ, Anping Dong ^c

^a Singapore Institute of Manufacturing Technology (SIMTech), Agency for Science, Technology and Research (A*STAR), 5 Cleantech Loop, 636732, Singapore

^b College of Mechanical and Electronic Engineering, China University of Petroleum (East China), Qingdao, 266580, China

^c Shanghai Key Lab of Advanced High-temperature Materials and Precision Forming and State Key Lab of Metal Matrix Composites, School of Materials Science and Engineering, Shanghai Jiao Tong University, Shanghai, 200240, China

^d Department of Mechanical and Aerospace Engineering, Princeton University, Princeton, NJ, 08540, USA

^e Department of Metallurgy and Materials Engineering, University of Malta, Msida, MSD 2080, Malta

^f School of Mechanical Science and Engineering, Huazhong University of Science and Technology, Wuhan, 430074, China

^g Department of Materials Science and Engineering, University of California at Irvine, Irvine, CA, 92697, USA

^h EPM Consulting, 2 Allée du Chateau, 38240, MEYLAN, France

ⁱ College of Materials Science and Engineering, Hunan University, Changsha, 410082, China

ARTICLE INFO

Handling Editor: Dragos Axinte

Keywords:

Additive manufacturing
3D printing
Hybrid additive manufacturing
Multi-fields
Auxiliary fields
Melt pool dynamics

ABSTRACT

Additive manufacturing (AM) offers unprecedented design freedom and manufacturing flexibility for processing complex components. Despite the numerous advantages of AM over conventional manufacturing methods, there are still some issues and bottlenecks that hinder the wide-scale industrial adaptation of AM techniques. The emerging field-assisted additive manufacturing (FAAM) is a designation that combines different auxiliary energy fields (e.g., ultrasound, magnetism, etc.) to overcome limitations in AM by benefiting from the intrinsic advantages of auxiliary fields. This work provides an up-to-date and dedicated review of FAAM in metallic materials, assisted by mainstream auxiliary magnetic, acoustic, mechanical, and thermal fields, as well as some emerging fields. The work principle and interaction mechanism between the field and the deposited metallic materials are elucidated. FAAM processes simulation and modelling are also reviewed. The auxiliary fields can affect the melt pool convection and dynamics, alter the temperature profile and thermal history during material solidification and induce stress or plastic deformation to the deposited materials. Hence, the effects of the auxiliary fields on the melt pool dynamics, solidification kinetics, densification behaviour, microstructure and texture, mechanical properties and fatigue performance are reviewed and discussed in detail. The perspectives on the research gap and further development trends of FAAM are also discussed.

1. Introduction

Fundamentally, the manufacturing methodologies are classified into three categories: (i) subtractive manufacturing (e.g., traditional machining), (ii) isostatic manufacturing (e.g., powder metallurgy and forging), and (iii) additive manufacturing (AM) such as laser powder bed fusion (LPBF) and laser directed energy deposition (LDED) [1]. The emerging AM (also called 3D printing) integrates multidisciplinary fields, including information technology, novel material technology,

manufacturing technology, etc [2]. AM is considered one of the top ten disruptive technologies in the 21st century that plays a crucial role in bringing about the Industrial Revolution 4.0.

The advantages of AM can be summarized as follows: (i) **Flexibility**: high freedom in geometric design and optimization [3]. (ii) **Customization**: customized and low-volume production [4]. (iii) **Acceleration**: accelerated prototyping and reduced manufacturing life cycle [5]. (iv) **Sustainability**: high materials and energy efficiency, waste reduction and environment friendly [6]. (iv) **Consolidation**: excellent capability in functional integration and part consolidation since AM can effectively

* Corresponding author.

** Corresponding author.

*** Corresponding author.

E-mail addresses: jinlongsu96@foxmail.com (J. Su), dafand@sjtu.edu.cn (D. Du), [yangdu@princeton.edu](mailto.yangdu@princeton.edu) (Y. Du).

¹ These authors contributed equally to this work.

Nomenclature	
AF	Acoustic field
BD	Build direction
CA	Cellular Automata
CET	Columnar-to-equiaxed transition
CSF	Continuum surface force
DF	Deformation field
EF	Electric field
EBM	Electron beam melting
FCG	Fatigue crack growth
FAAM	Field-assisted additive manufacturing
FDM	Finite difference method
FEM	Finite element method
FVM	Finite volume method
δ	Fracture elongation
HT	Heat treatment
HIP	Hot Isostatic Pressing
HDMR	Hybrid deposition and micro-rolling process
IHT	In-situ heat treatment
LAM	Laser additive manufacturing
LDED	Laser-directed energy deposition
LPBF	Laser powder bed fusion
LSP	Laser shock peening
MHP	Machine hammer peening
MF	Magnetic field
MHD	Magnetohydrodynamics
NIST	National Institute of Standards and Technology O
OM	Optical microscope
ΔH	Rolling reductions
S-N	Stress versus the number of cycles to failure
G	Temperature gradient
R	The growth rate of the solid/liquid interface
TF	Thermal field
TEMC	Thermoelectric magnetic convection
TEMF	Thermoelectric magnetic force
UTS	Ultimate tensile strength
USV	Ultrasonic vibration
ΔT	Undercooling rate
VOF	Volume of fluid
VOSET	Volume-of-fluid and level set
VED	Volumetric energy density
WAAM	Wire arc additive manufacturing
YS	Yield strength

consolidate manufacture and assembly into one part with a single process, improving the components' reliability due to the reduced amount of assembling [7]. (v) **Performance:** the rapid cooling and solidification rate results in extremely fine microstructure, which together with the internal high-density dislocations, lead to superior or comparable mechanical strength to the cast and forged parts for many materials [8].

The printing of metals is the fastest-growing sector of AM due to its capability to manufacture parts that cannot be made by other processes

while minimizing the number of processing steps [9]. Typical metal AM includes LPBF, LDED, electron beam melting (EBM) and wire arc additive manufacturing (WAAM). Among these, the field-assisted AM are primarily based on LPBF, LDED and WAAM. The schematics, technical parameters, metallurgical features, merits, and typical applications of LPBF, LDED and WAAM are summarized in Fig. 1. Due to different deposition principles and technical parameters, each of these three technologies has its own metallurgical characteristics, advantages, and

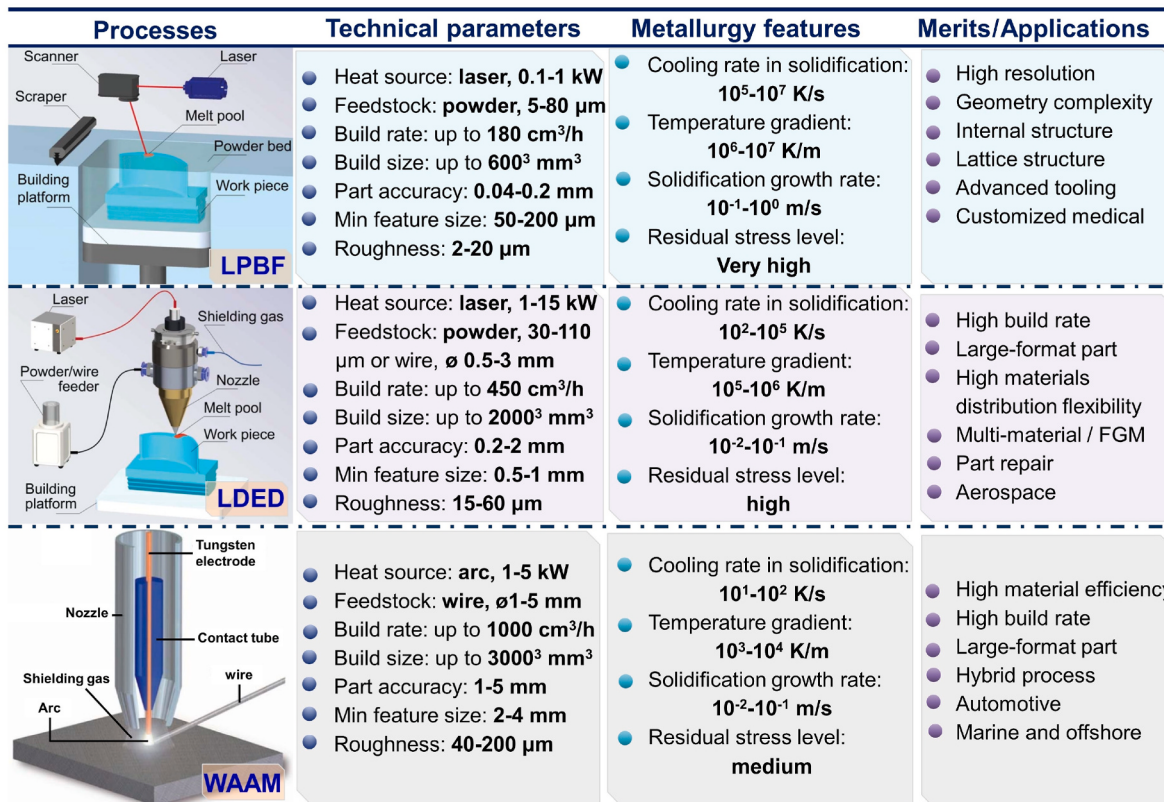


Fig. 1. The outline of typical metal additive manufacturing technologies used in field-assisted additive manufacturing (FAAM) [1,9-13].

scope of applications. LPBF has a lower build rate but an excellent capability in processing complex geometries, such as lattice structures, advanced tooling (e.g., mould inserts with conformal cooling channels), customized medical implants, etc. In contrast, the LDED and WAAM have a lower dimension resolution while a much higher deposition rate than LPBF, making them suitable for large format component fabrication. Besides, the increased flexibility of materials feeding in LDED and WAAM enables the deposition of multi-materials within the same layer and across the layers. The flexible toolpath in LDED enables the repairing of large freeform parts. Originating from different thermal histories and solidification behaviour between processes, the grain size in AM-processed metallic materials follows the order of LPBF < LDED < WAAM, and its strength is in the order of LPBF > LDED > WAAM in general.

Despite the exciting advantages of AM over conventional manufacturing methods (e.g., machining, casting, and forging processes), there also co-exist some issues and bottlenecks in metal AM, such as defects in poor-printability materials, large and highly columnar dendrites resulting in anisotropic mechanical properties, poor fatigue performance, etc. To solve these problems and reap the full potential of AM technologies, novel methodologies have been investigated for tailoring microstructures, innovating equipment and devices, and introducing new concepts [14]. Field-assisted additive manufacturing (FAAM) is a designation that combines different technologies to overcome limitations in AM and benefit from the intrinsic advantages provided by the application of auxiliary fields.

As outlined in Fig. 2, the typical auxiliary fields applied in AM are magnetic, acoustic, mechanical, and thermal fields. Besides, there are also some emerging FAAM technologies which use plasma field, electric field, and coupled multi-fields as the auxiliary energy fields. FAAM has

been applied to a vast wide range of metallic materials, including Al alloys, Ti alloys, Ni-based superalloys, Mg alloys, and steels. The auxiliary fields have a significant influence on the melt pool convection and dynamics, temperature profile and microstructural solidification behaviour, etc. The application of auxiliary fields in AM brings several improvements to the AM process, notable amongst which there are: (i) Improve formation quality and surface roughness; (ii) improve the printability and densification of materials; (iii) reduce residual stress or alter residual stress condition (e.g., from tensile to compressive); (iv) affect the solidification behaviour and tune the microstructure; (v) alleviate anisotropy in mechanical properties and enhance mechanical performance; (vi) improve fatigue performance, etc.

The motivation of this work is to provide an up-to-date and dedicated review on FAAM in metallic materials, including the mainstream magnetic, acoustic, mechanical, and thermal fields assisted AM, as well as some emerging fields in AM (e.g., electric and plasma fields). The work principle and field-material interaction mechanisms are elucidated, and the subsequent effects of the auxiliary fields on the process, materials, and performance in AM metallic materials are reviewed and discussed in detail. The perspectives on the research gap and further development trends of FAAM are also discussed. This critical review aims to provide researchers with complete state-of-art information on FAAM, which could help identify the deficiency and strengths of each FAAM technology and advance the maturity and technology readiness levels and therefore, promoting the transformation of FAAM technologies from lab to industrial applications.

2. Magnetic field assisted additive manufacturing (M-FAAM)

In metal AM, the presence of an imposed external magnetic field

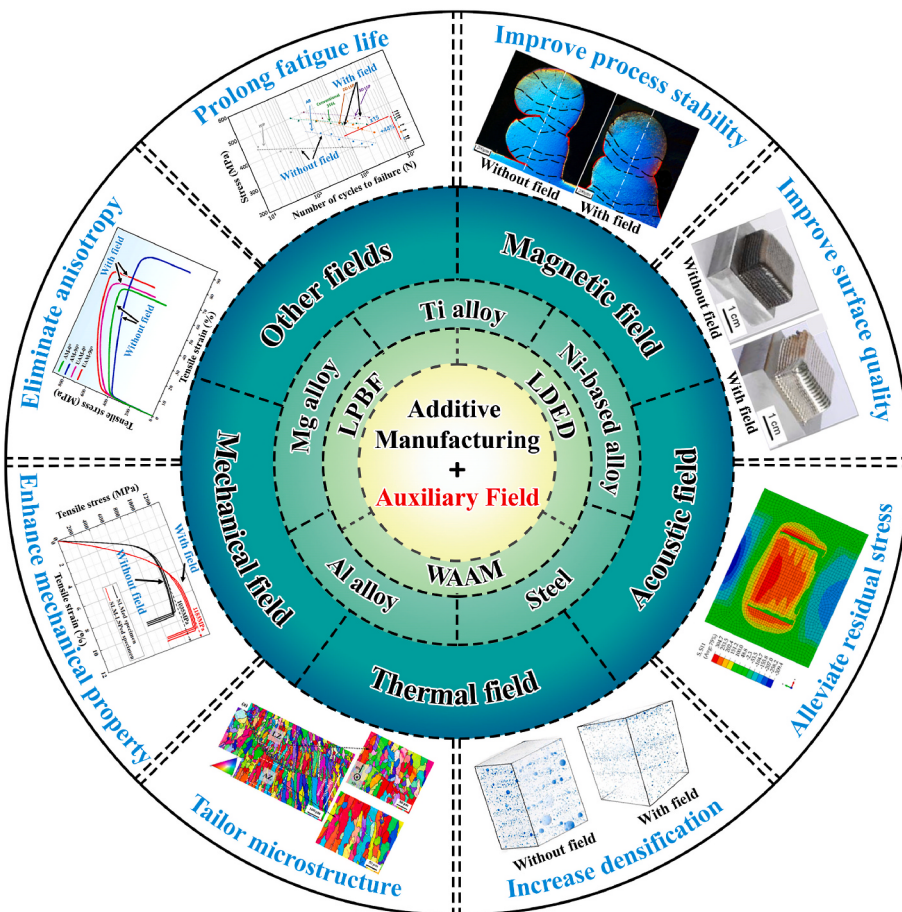


Fig. 2. An overview of the multi-type of field-assisted additive manufacturing (FAAM) technologies. Image sources from Refs. [15–22].

(MF) will influence the melt pool dynamics and its solidification mechanism. In this section, the fundamental effects of a static MF on the solidification of metal as well as the mechanisms that are associated with melt pool dynamics are discussed. The discussion builds on a review of research progress in the field of static MF-assisted AM from the perspectives of materials, methods, and applications. In addition, the challenges faced by static M-FAAM and future development trends are also discussed.

2.1. Work principle of magnetic field in additive manufacturing

2.1.1. Magnetic field and materials interaction mechanism

As a clean, efficient, and non-contact method, MF has attracted wide research attention for applications to processing metallic materials. For instance, a variety of appealing phenomena can be achieved by applying the MF in casting, including magnetic orientation [23,24], magneto-thermodynamics [25] and magnetohydrodynamics (MHD) [25–27]. Therefore, many types of MF, including static MF [28–32], travelling MF [33,34], rotating MF [35–37] and pulsed electromagnetic

fields [38–40], have been adopted in metallic materials processing.

During the metallic materials processing, the MF typically affects the solidification process through two mechanisms: the MHD effect caused by the Lorentz force and the magnetization effect resulting from the magnetic force [41]. There are many types of MFs designed to understand how MHD affects the solidification behaviour of the melt pool. As demonstrated in Fig. 3a and b, the Marangoni flow could generate the Lorentz force and restrain the melt flow when the flow direction is unparallel to the MF direction. Moreover, the MHD effect could also affect the melt flow due to the induced electric current, which is related to the generalized electric field (E) following Ohm's law:

$$\vec{j} / \sigma = \vec{E} + \vec{u} \cdot \vec{B} - S \vec{\nabla} T \quad (1)$$

where \vec{E} , σ , \vec{u} , \vec{B} , $\vec{\nabla} T$ and S denote the electric field, electrical conductivity, velocity, MF flux intensity, temperature gradient and Seebeck coefficient, respectively.

Assuming that the liquid is incompressible, the fluid flow is governed

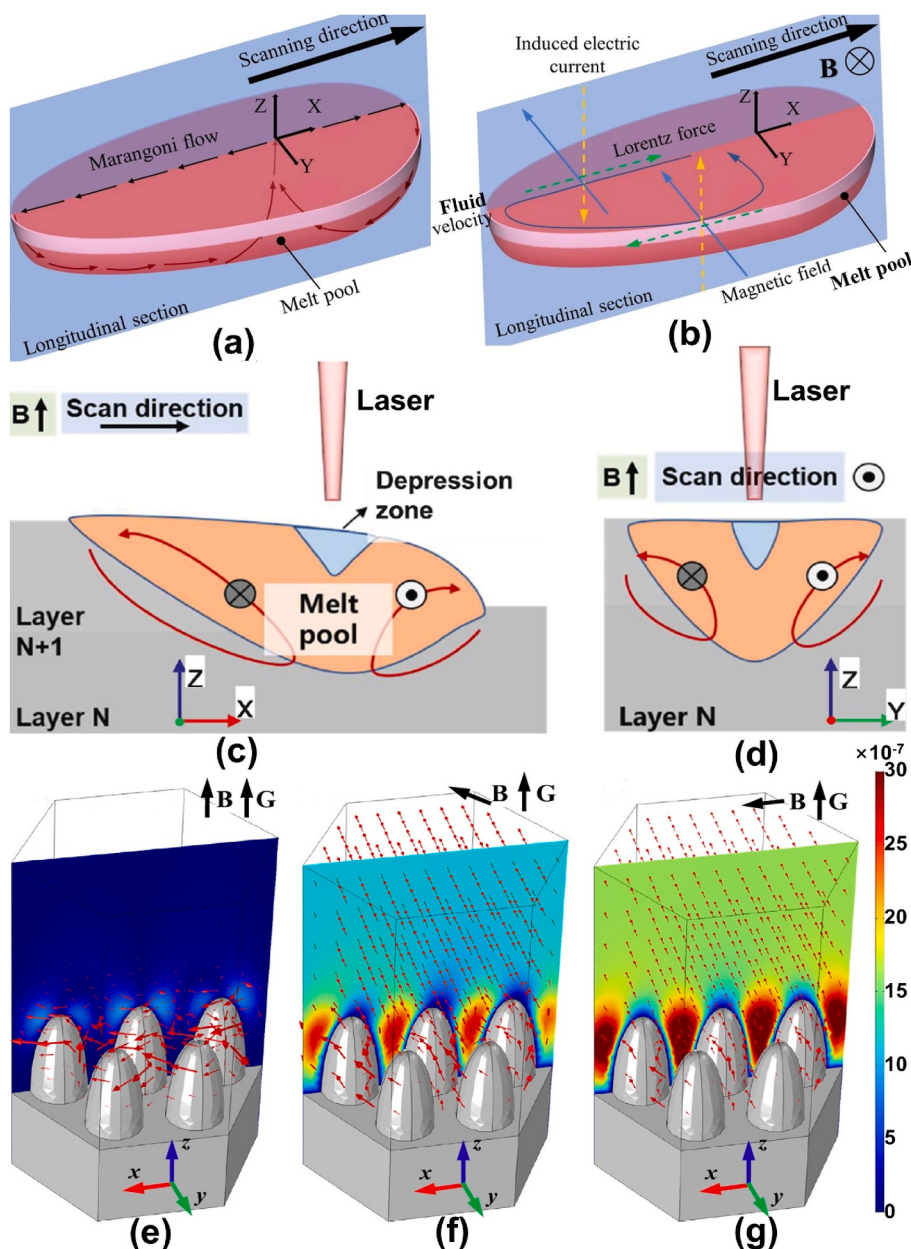


Fig. 3. Schematic illustration of the mechanism of the magnetic field during additive manufacturing: (a) Marangoni flow in the melt pool without magnetic field [43]; (b) induced current and Lorentz force restrains the melt flow with applied magnetic field; (c) and (d) induced thermoelectric magnetic convection (TEMC) at the melt pool scale in XZ and YZ plane, respectively [44]; and the induced thermoelectric magnetic force (TEMF) in different positions (e) bottom, (f) side and (g) tail of the melt pool at the dendritic scale [45].

by the Navier-Stokes equation, which can be written as

$$\begin{aligned} \frac{\partial(\rho \vec{u})}{\partial t} + \rho(\vec{u} \cdot \nabla \vec{u}) &= -\nabla p + \mu \nabla^2 \vec{u} + \vec{j} \times \vec{B} \\ &= -\nabla p + \sigma E \times \vec{B} + \sigma(\vec{u} \times \vec{u}) \times \vec{B} - \sigma S \vec{\nabla} T \times \vec{B} + \rho v \nabla^2 \vec{u} \end{aligned} \quad (2)$$

where ρ is the density, μ is the dynamic viscosity, and p is the pressure. As shown in Equation (2), the restraining effect is caused by the braking force demonstrated as the term $\sigma(\vec{u} \times \vec{u}) \times \vec{B}$, and the forced convection can be demonstrated as the term $\sigma S \vec{\nabla} T \times \vec{B}$. Due to the high-temperature gradient $\vec{\nabla} T$ in the melt pool, the Seebeck effect between solid and liquid phases cannot be ignored, which would induce a thermoelectric current as shown in Fig. 3c and d. This force would result in the thermoelectric magnetic force (TEMF) in the liquid phase, which functions as thermoelectric magnetic convection (TEMC) at the melt pool scale. Under the different MF directions, the induced TEMF and TEMF will be different according to the Lorentz force. For example, the TEMC will be in the X-axial direction if the MF direction is face-up instead of a convention loop in the XY plane, as shown in Fig. 3c and d. The melt pool shape and microstructure will be changed accordingly. Overall, there has been some work to understand the effect of MF in melt pool convection during solidification; however, more work to study the effects of different MF directions on the microstructure and mechanical properties is required to further understand this effect. The TEMF acting on the dendrite in the mushy zone changes the normal dendritic growth behaviour since it breaks the dendrites and forms fragments, as shown in Fig. 3e–g. As illustrated in Fig. 3e–g, the thermoelectric magnetic effect at the cell/dendritic scale could induce TEMC between dendrites. Due to the different locations in the melt pool, the dendrites encounter different thermoelectric magnetic effects. As shown in Fig. 3g, with a vertical static MF, the dendrites at the tail of the melt pool perform the strongest thermoelectric magnetic effects.

As the result of the inherent magnetic properties of all materials, magnetism can be effectively used to control the microstructure of the materials during solidification. The magnetism can be characterized using magnetic susceptibility as defined according to the equation:

$$M = \chi H \quad (3)$$

where χ , M and H are the volume magnetic susceptibility, the magnetic magnetization, and the MF intensity, respectively. Magnetic susceptibility is closely related to some magnetic effects, such as the magnetic force and its orientation. The magnetization body force acting on the materials can be calculated as follows:

$$\vec{F}_m = \mu_0 (\vec{M} \nabla) \vec{H} = \frac{\chi}{\mu_0} (\vec{B} \nabla) \vec{B} \quad (4)$$

where \vec{F}_m is proportional to the square of \vec{B} , which can levitate the substances and separate phases with different magnetic susceptibility. Moreover, the magnetization energy of the materials induced by the magnetization force can be defined as:

$$E_m = - \int_0^H \mu_0 \vec{M} d\vec{H} \quad (5)$$

The magnetization energy can influence the characteristics of the phase boundaries, the kinetics of phase transformation, and grain texture [41,42]. The typical metallic alloys used in AM (e.g., Al alloys, Ti alloys and Ni-based superalloys) are usually non-ferromagnetic materials, and the applied MF intensity for AM is lower than 1 T. Therefore, the magnetism effect in AM can be neglected in most present studies.

2.1.2. Set-up of magnetic field assisted metal additive manufacturing

Even though AM is proven to be helpful in processing a broad range of materials with complex structures (such as topologically optimized

structures), the temperature gradients in AM vary in directions parallel and perpendicular to the build direction, leading to the anisotropic of microstructures and consequently mechanical behaviours. To solve these challenges, researchers have studied the influence of magnetic field on the LPBF [45–47], LDED [48–50] and WAAM [51–54] processes.

In the LPBF process, a typical setup is to place the magnets on both sides of the build plate (see Fig. 4a) or at the bottom of the build plate (see Fig. 4b and c). However, due to building chamber space limitations, the addition of MF in the LPBF process is not as flexible as LDED. In the LDED process, the permanent magnets can be assembled to the side (Fig. 4d) or under (Fig. 4e) the build plate [48]. Additionally, the permanent magnets [50] or electric magnets [55] can be equipped on the nozzle, and the MF could move with the nozzle as shown in (Fig. 4f), which is more flexible and controllable in both academic research and industrial application.

In the WAAM process, as shown in Fig. 4g–i, the external MF will interact with an internal magnetic source generated by arc electric current flow, producing an integrated MF to interact with the arc current and form an external force. MF assist WAAM has been widely studied to overcome the methodological drawbacks and improve the properties of processed materials [51–54,56].

2.2. Effect of magnetic field on densification

2.2.1. Porosity and densification

Due to the non-equilibrium rapid solidification of materials during AM and the associated segregation present in such processes, defects (e.g., porosity and cracking) in solidified materials are common within the AM-processed metallic parts. Different porosity formation mechanisms exist and can be summarized as follows: (i) lack of fusion caused by insufficient energy input, which typically results in irregularly shaped pores [57], (ii) keyhole pores form due to excessive energy input. These are usually roughly spherical and concentrate at the bottom of the melt pool. The keyhole pores are caused by keyhole fluctuation and vapour depression instability [58,59], (iii) gas pores from the powder or entrapment of the shielding inert gas into the melt pool [60]. Gas pores tend to be smaller than keyhole porosity or lack of fusion pores.

Auxiliary MF has shown feasibility to reduce porosity in AM of metallic materials. For instance, the porosity of LPBF fabricated AlSi10Mg alloys was evidently decreased with auxiliary 0.12 T vertical MF (see Fig. 5a), which was possibly due to the reduction of Marangoni convection and release of trapped gas in the melt pool, as illustrated in Fig. 5b [45]. To further understand the relationship between porosity changes and static MF, LPBF of AlSi10Mg alloys within a wide range of laser energy densities were performed, and the results in Fig. 5c showed that the relative density increases with increasing MF intensity within the lower energy density range ($\leq 60 \text{ J/mm}^3$) [44]. This trend was attributed to the TEMF generated by MF, increasing the depth of the melt pool and consequently its energy absorption capacity.

Similarly, the porosity of the LDED fabricated Inconel 718 was decreased from 0.3% to 0.2% with a 0.2 T vertical MF [50]. In related studies, the density of LPBF-processed SS316 alloys increased with static and alternating MF addition, in which the melt flow inhibition by MF is considered responsible for the density increment [47]. Further porosity formation mechanism in M-FAAM was revealed by real-time and in-situ high-speed X-ray imaging, which demonstrated that a higher MF density is beneficial for achieving less porosity since the external MF can stabilize and slow down convection drastically within the melt pool [61]. However, it has also been reported that the applied MF increased the porosity in LDED-processed purity nickel by up to 12.9% [62]. In this study, the authors suggested that the magnetically trapped plasma may play an important role in pore formation, and further work is needed to unveil more details on the governing mechanisms. Therefore, the applied MF should be carefully optimized along with AM process parameters to achieve an improvement in densification.

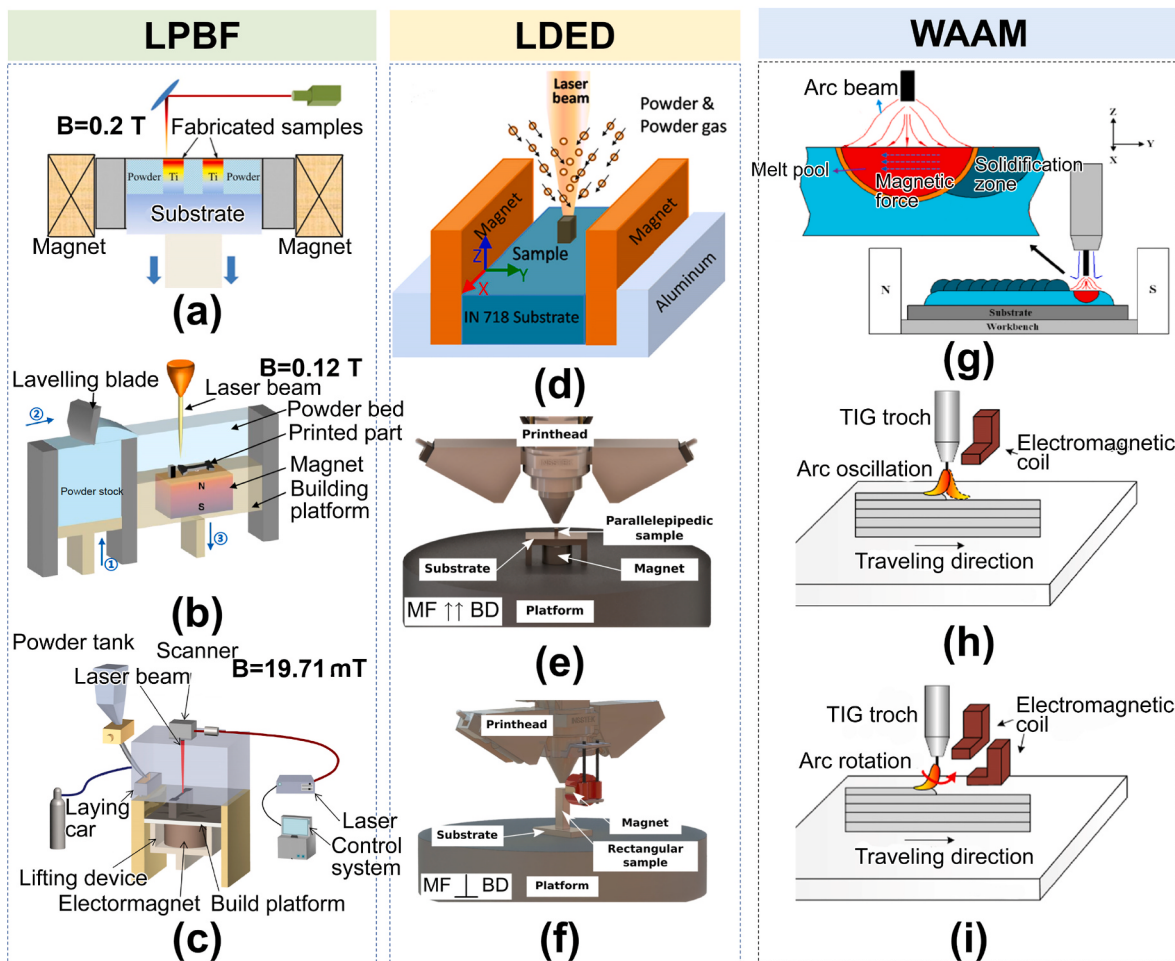


Fig. 4. Schematics of additive manufacturing with the auxiliary magnetic field (MF). LPBF with (a) horizontal static MF [46], (b) vertical static MF [45], and (c) vertical static and high-frequency MF [47]; LDED with (d) horizontal static MF [48], (e) vertical and (f) horizontal MF [50]; WAAM with (g) horizontal static MF [52], (h) one direction and (i) two perpendicular directions electric-induced MF [54].

2.2.2. Cracks

Cracking plays a significant role in the mechanical property of AM fabricated parts [63,64]. There are three primary types of cracks in AM-fabricated parts: (i) Solidification cracking is caused by the insufficient feeding of remaining liquid to accommodate the solidification shrinkage strain between cell/dendrite arms. (ii) Liquation cracking resulting from the incipient melting of grain-boundary precipitates during rapid heating to below the liquidus temperature of bulk material. (iii) Solid-state cracking due to the propagation of cracks that nucleated as hot tears.

To address cracking, many solutions have been proposed, such as optimised powder composition for improved printability [65–67] and nanoparticle addition to change the solidification mechanism and control solidification microstructures during AM [68–70]. Apart from these approaches, auxiliary MF offers another way to suppress cracking in AM-processed parts, as it could also change the solidification behaviour of the melt pool. Limited work has been done to study the effect of MF on the cracking of AM parts. Seidel et al. applied an MF to minimize hot cracking in the LDED-processed MAR-M-247 nickel superalloy (Fig. 6), in which the hot cracking was drastically reduced through the application of an auxiliary MF while liquation cracking still occurred for all approaches [55]. The relationship between the modified Marangoni convection by MF and the cracks is still not properly elucidated. As Martin et al. [68] reported, cracks can be restrained by promoting the columnar-to-equiaxed transition (CET) since the refined equiaxed grains could allow grain rotation and prevent crack initiation and growth.

2.2.3. Forming quality

As a result of the process limitations inherent to LPBF, research on the influence of MF on the forming quality of AM fabricated components has been primarily centred on LDED and WAAM processes. For example, Simth et al. [71] studied the application of MF-assisted LDED to produce components from magnetic feedstock materials (i.e., nickel powder). In this study, a solenoid coaxially aligned to the laser beam was used to manipulate the quality of the track. As shown in Fig. 7a, the mean track area and height increase dramatically with an application of 93.5 mT MF. The MF could be used as an adaptive control technique. In fact, switching the solenoid off resulted in narrower and shorter tracks with a smaller cross-section area; and the powder catchment efficiency was increased from 25.1% to 28.5% by MF due to the improved powder stream focus (Fig. 7c) [62]. Besides, Wang et al. [52] also investigated the influence of a static MF on the forming quality in WAAM of Inconel 625 alloys. As shown in Fig. 7d and e, the horizontality of the sample deposited with MF is significantly improved compared with that deposited without MF. It is postulated that Lorentz forces push the melt pool to the sides, and the melt pool flows more uniformly under the effect of arc stirring by MF, which improved the melt pool flowability to achieve a better surface horizontality.

2.3. Effect of magnetic field on microstructural evolutions

2.3.1. Grain size and texture

Due to the high melt pool cooling rates in AM, the fabricated metallic

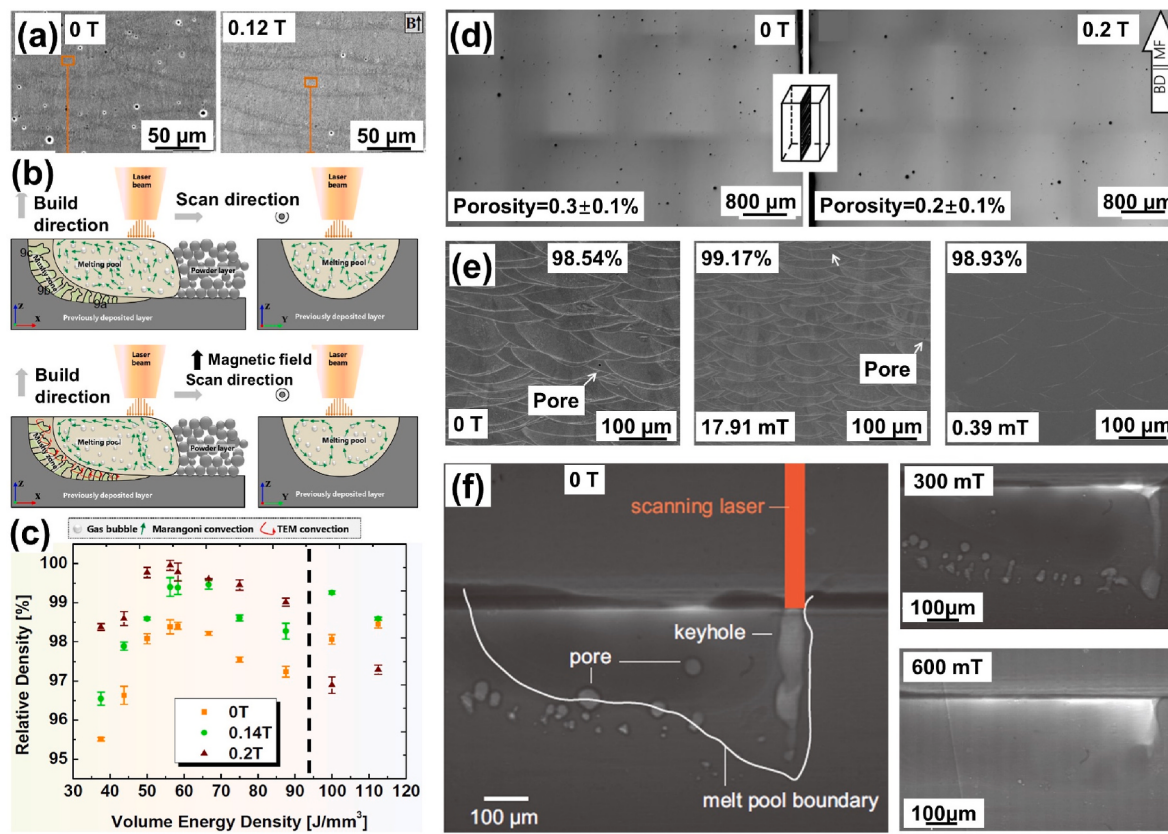


Fig. 5. Evolutions of porosity and densification of AM fabricated parts with the auxiliary magnetic field (MF). (a) Pore morphology in LPBF AlSi10Mg alloys without and with MF [45], (b) schematic diagram illustrating the mechanism of porosity decrease after applying MF [45]; (c) Densification behaviour in LPBF AlSi10Mg alloys for a wide volume energy density range [44], (d) Porosity decreased from 0.3% to 0.2% with an applied vertical MF in LDED Inconel 718 alloys [50], (e) MF (static and alternating) increased the density of LPBF SS316 alloys [47], and (f) In-situ synchrotron radiation study illustrating porosity changes in LPBF-processed 4140 steel [61].

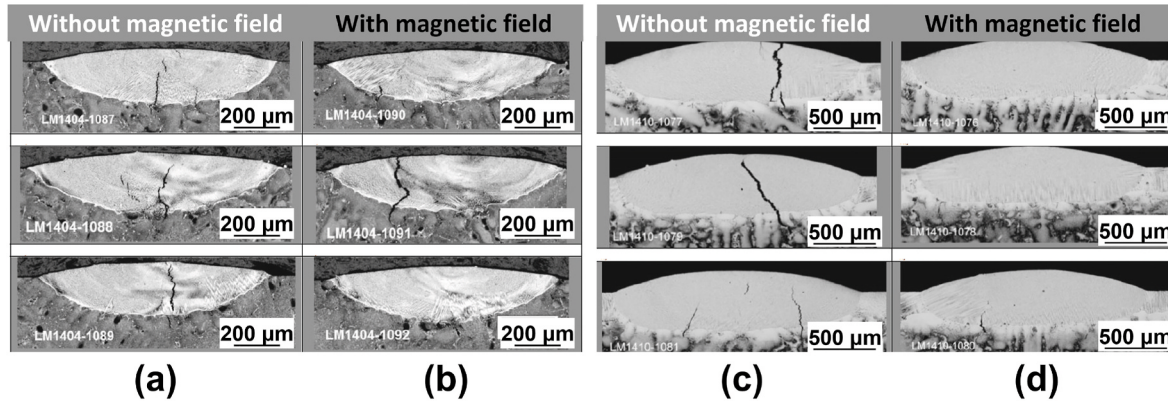


Fig. 6. Effect of magnetic field on the cracks in the LDED fabricated Mar-M-247 alloys. (a) and (c) without magnetic fields, and (b) and (d) with magnetic fields [55].

parts generally exhibit finer grains and sub-grain structures than traditional casting processes, together with a grain alignment along the build direction. The deployment of auxiliary MF could affect the grain size and texture of AM-processed metallic materials. It was reported that a 0.2 T MF led to further grain refinement and dramatically weakened the prevalent <001> texture (Fig. 8a and b) in LPBF-processed AlSi10Mg [44]. The main reason for the grain refinement in the M-FAAM fabricated samples is attributed to the high TEM force acting on the cell/dendrite, which causes the fragments to act as new nuclei, as illustrated in Fig. 8c [45]. Similarly, the auxiliary MF has been reported to refine the grains in LDED-fabricated Ti6Al4V alloys (Fig. 8d) [47]. Moreover,

the restraint of the melt pool flow also increase the constitutional undercooling at the solid/liquid interface, therefore increasing the number of nuclei [44]. However, the auxiliary MF was also reported to coarsen the grain size and promote the epitaxial growth of long columnar grains in LDED of Inconel 718 alloys (Fig. 8e) [48]. This phenomenon was mainly attributed to the restrained melt flow by MF during the solidification process. As discussed in Section 2.1.1, MF could influence the melt convection in two aspects, including the TEMC effect and damping effect, of which development plays a significant role in the solidification depending on the physical properties of alloys, length scale and MF density. Huan et al. [53] also showed that the coarse columnar

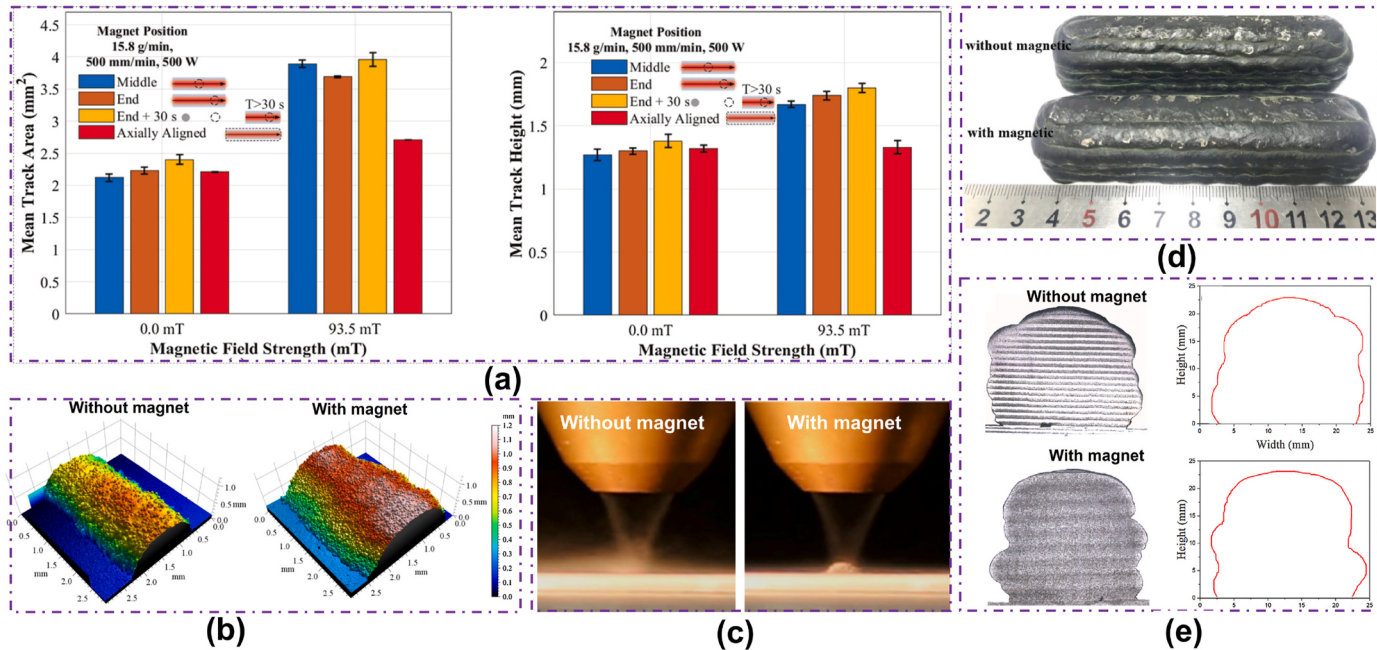


Fig. 7. Effect of auxiliary magnetic field (MF) on the powder catchment efficiency and surface morphology. (a) Powder catchment efficiency increased by an applied MF [62], (b) shape of LDED deposited tracks without and with an MF [62], (c) powder stream changed by an applied MF [62], and (d) WAAM fabricated parts and (e) the corresponding contour of samples [52].

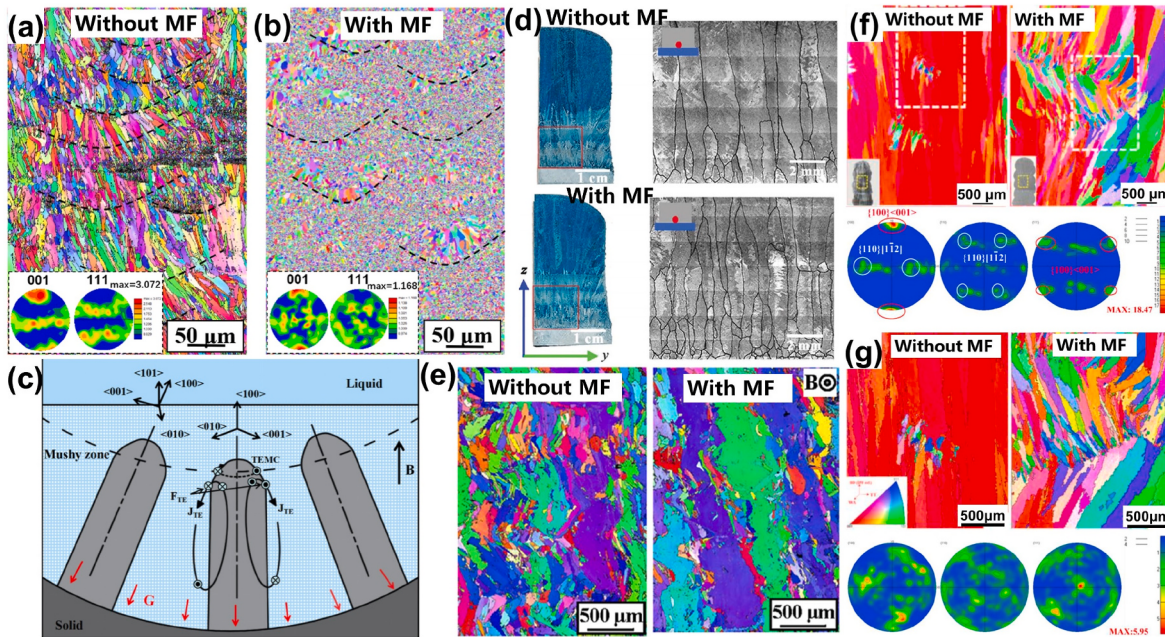


Fig. 8. Effect of auxiliary magnetic field (MF) on the grain and texture in AM. (a) and (b) The inverse pole figures of LPBF fabricated AlSi10Mg alloys without and with a static MF respectively [44], (c) schematic showing the influence of a static MF on the grain morphology and texture during AM [45], (d) MF refined the grains in LDED-fabricated Ti6Al4V alloys, (e) IPF images show the effect of MF on the grain size of LDED fabricated Inconel 718 alloy [48], and (f) and (g) inverse pole figures and corresponding pole figures of the WAAM-fabricated Inconel 718 alloys without and with alternating MF respectively [53].

crystals crossing several passes are interrupted and the grain growth direction is significantly changed with the alternating MF during WAAM of Inconel 718 alloys (Fig. 8f and g).

2.3.2. Dendrite morphology and microsegregation

During the rapid solidification in AM, the sub-grain morphology will consist of fine dendritic or cellular structures depending on the cooling rate and thermal gradient prevalent in the melt pool. Fig. 9 compares the

microstructure of AM fabricated parts with and without auxiliary MF, and the results show that MF dramatically changes the dendritic structure. Fig. 9a shows that the cellular dendrite size increased from 5.0 to 7.1 μm with a vertical static MF [50]. Besides, the effects of static MF on the dendrite morphology of WAAM-fabricated Inconel 625 alloys were also investigated, and the results show that the sub-grain structure gradually changes from dendritic to cellular when applying MF [52].

In addition to the grain refinement, a columnar to equiaxed

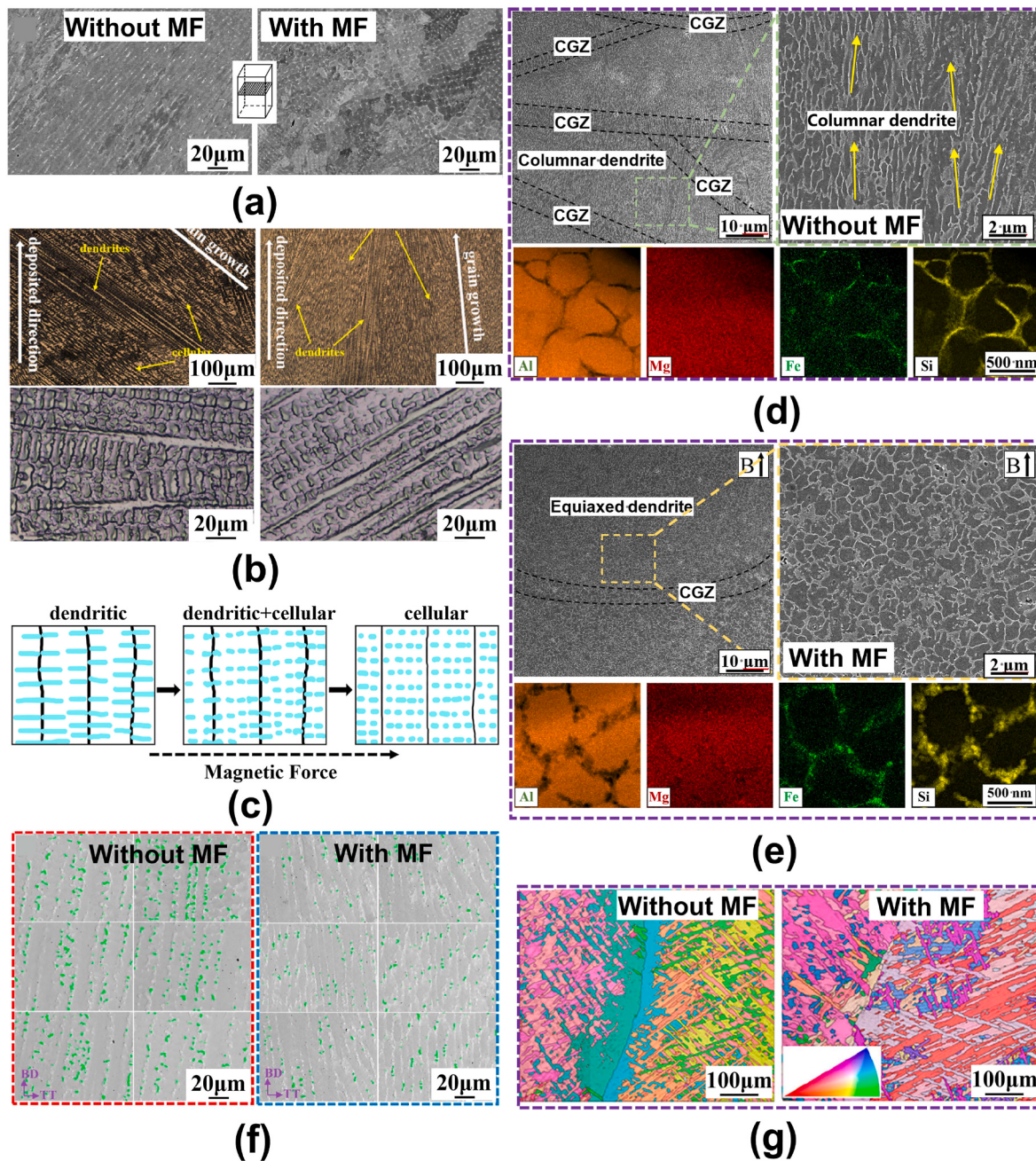


Fig. 9. Effect of auxiliary magnetic field (MF) on microstructural morphology evolutions in AM. (a) Dendrite morphology evolution of LDED fabricated Inconel 718 [50], (b) dendrites evolutions and corresponding (c) schematics of Inconel 625 deposited by WAAM with auxiliary MF [52,53], (d) columnar to (e) equiaxed dendrite transition (along with element mapping) in LPBF AlSi10Mg alloys [44], (f) dendrite spacing and Laves phase volume decreasing with the applied MF in WAAM Inconel 718 [53], and (g) phase transition in LDED Ti6Al4V alloys [49].

transition caused by MF in LPBF-processed AlSi10Mg alloy has also been reported [44]. Moreover, the continuous eutectic Si phase at the cell boundary changes to a discontinuous morphology, which is thought to be caused by the TEMC effect as it increases with increasing MF at the cell/dendrite scale and causes the degeneration of the regular Si structure [44]. This result is similar to the one obtained by Huan et al. [53], as shown in Fig. 9g. Accompanied by the decreasing of dendrite spacing, the volume fraction of the Laves phases is significantly reduces from 2.4% to 1.3%, and the long-striped Laves phases are inhibited considerably when applying MF. In LDED fabricated Ti6Al4V alloys, continuous α grain boundaries transform to discontinuous α grain boundaries [49]. Currently, there is a lack of quantitative study investigating the effect of MF on microsegregation in AM. However, due to the significant

thermoelectric magnetic effect at both dendrite and melt pool scales, microsegregation at the dendrite scale could be improved theoretically. Moreover, the typical inherent dislocation lines in the AM-processed Ti6Al4V sample change to planar dislocation arrays and tend to form the grain boundaries with the applied MF. The reason for modification of the dendrite structure in the AM alloys is thought to be attributed to the thermoelectric magnetic effect at the cell/dendrite scale. On the one hand, the induced TEMC increases with increasing MF, and promotes the solute diffusion at the tip of the dendrite; on the other hand, the TEMF acting on the solid phase is strong enough (10^6 – 10^7 N/m³ at 0.1 T [44, 49]) to break up the columnar cell/dendrite structure. Both grain refinement and microstructural homogenization should result in the improvement of the tensile properties and fatigue behaviour.

2.4. Effect of magnetic field on mechanical properties

The mechanical properties of the reviewed AM-processed materials with various types of MF are summarized in Table 1. The yield strength (YS), ultimate tensile strength (UTS) and fracture elongation (δ) of M-FAAM fabricated materials are mostly higher than those manufactured by pure AM. The MF-assisted LPBF-processed AlSi10Mg showed a high UTS of 420 MPa and δ of 8.8%; comparable to wrought Al2 \times \times to Al7 \times \times series alloys (Fig. 10b) [45]. Similarly, the MF enhanced the ductility and strength of LPBF-processed SS316 simultaneously [47], in which the UTS of samples is slightly improved with an applied MF while the δ is significantly increased from 38.4% to 52.6% under a 19.71 mT static MF and to 45.7% under a 0.39 mT alternating MF, respectively.

The results reported by Zhao et al. [49] showed that the applied MF intensity increases the ductility from 3.4 to 10.8% while decreasing the tensile strength of the LDED-fabricated Ti6Al4V alloy (i.e., the strength reduces dramatically for conditions fabricated with vertical and horizontal MFs). The decrease in strength is mainly attributed to the fact that the dislocations can pass through from the discontinuous α grain boundaries to adjacent β grain, reducing dislocation strengthening and increasing the ductility [49]. As for the WAAM, the mechanical properties of the samples deposited with MF also exhibit higher hardness value [52] and higher UTS and δ in general [52,53].

As discussed in the previous sections, the presence of a MF during AM can significantly reduce porosity, inhibit crack formation and promote grain refinement, which can improve mechanical properties. With an applied MF, the MHD effect could restrain the natural fluid flow in the melt pool. Meanwhile, due to the significant Seebeck effect caused by the high-temperature gradient, the TEMF could act on the liquid to create convection at both the dendritic and the melt pool scales. As mentioned before, the fluid flow magnitude and pattern modification by the MF depends on the physical properties of the alloys and MF density.

The results reviewed in this section suggest that the application of an MF to AM process can potentially yield beneficial effects under a broad set of conditions and for a wide range of metals and alloys. Even though the MF has been successfully employed in AM processes, the mechanism of the MF on the fluid flow is not yet been fully understood, and further efforts are required to understand the thermoelectric and

magnetohydrodynamics in the melt pool.

3. Acoustic field assisted additive manufacturing (A-FAAM)

The A-FAAM has gained increasing interest in the past few years. In this section, the work principle of acoustic field (AF) assisted metal AM is reviewed. Besides, the effects of auxiliary AF on the densification behaviour, microstructure evolution and mechanical properties of the AM fabricated materials are discussed in detail. In A-FAAM, the acoustic energy introduced by ultrasonic vibration (USV) is combined with the AM process to form acoustic streaming and cavitation effects to govern the melting and solidification process, thereby tailoring the microstructure and properties of the deposited materials. Notably, A-FAAM is only reported for the directed energy deposition processes such as WAAM and LDED, and it could not be applicable to the LPBF process since the USV will scatter the powder layer.

3.1. Work principle of acoustic field in additive manufacturing

According to the AF source configuration in AM system, A-FAAM technologies can be divided into two types, i.e. substrate USV-assisted AM (Fig. 11a and b) and moving USV-assisted AM (Fig. 11c and d). In the substrate USV-assisted AM, the USV is placed at the bottom of the substrate, and acoustic energy is directly transmitted to the substrate, as shown in Fig. 11a and b [72,73]. The substrate USV set-up is simple and easy to fulfil and non-contact with the melt pool. However, the ultrasonic intensity decreases significantly with increasing build height and is therefore not suitable for fabricating tall parts. Todaro et al. [72] studied the relationship between the ultrasonic intensity and the building height and reported that the ultrasound intensity drops from the peak value to zero with the build height increases to \sim 62.5 mm, indicating that the height of the deposited sample should be controlled at a realizable value to achieve significant microstructural refinement. For the moving USV set-up, as shown in Fig. 11c and d, the ultrasonic head moves synchronously with the arc/laser beam [74,75]. The moving USV process has a constant ultrasonic intensity during AM and, therefore, can be used for fabricating large-format components. However, the contamination problem (e.g., the introduction of interstitial

Table 1
Mechanical property of AM fabricated parts with the assistance of various magnetic fields.

AM	MF	Material	MF intensity (mT)	Mechanical property	Property with MF	Property without MF	Units	Property increment	Ref.
LPBF	Vertical static	AlSi10Mg	120	UTS	420 \pm 10	325 \pm 15	MPa	+29.23%	[45]
				δ	8.8	6	%	+46.67%	
	Vertical static	SS316	19.71	UTS	661.0 \pm 9.3	658.2 \pm 8.0	MPa	+0.46%	[47]
				δ	52.6 \pm 3.1	38.4 \pm 1.3	%	+36.98%	
LDED	Vertical alternating	SS316	0.39	UTS	682.2 \pm 4.1		MPa	+3.65%	
				δ	45.7 \pm 0.8		%	+19.01%	
	Horizontal static	CP-Ti	100	UTS	794	766	MPa	+3.66%	[46]
				δ	35	28	%	+25%	
WAAM	Horizontal static	Inconel 718	200	UTS	1063 \pm 2	1056 \pm 11	MPa	+0.66%	[50]
				δ	23 \pm 1	23 \pm 1	%	0	
	Vertical static	Inconel 718	200	UTS	831 \pm 31	821 \pm 22	MPa	+1.22%	
				δ	27 \pm 7	23 \pm 5	%	+17.39%	
	Horizontal static	Ti6Al4V	550	UTS	864.4 \pm 13.6	869.6 \pm 23.3	MPa	-0.58%	
		Vertical sample		YS	775.0 \pm 0.8	782.3 \pm 18.2	MPa	0.94%	
				δ	12.6 \pm 1.7	11.2 \pm 1.1	%	+12.5	
		Inconel 625	20	UTS	740 \pm 14	695 \pm 11	MPa	+6.47%	[52]
	Horizontal static	Inconel 625	20	YS	436 \pm 13	384 \pm 1	MP	13.54%	
				δ	48.7 \pm 1.9	46.4 \pm 1	%	+4.96%	
	Alternating	Inconel 718	/40 A, 20 Hz	UTS	917	934	MPa	+1.85%	[53]
				δ	34.5	35	%	+1.45%	
	Vertical static	Ti6Al4V	2	UTS	895 \pm 20	833 \pm 23	MPa	+7.44%	[54]
		Arc oscillation		YS	832 \pm 18	785 \pm 26	MPa	+5.99%	
				δ	11.3 \pm 1.4	12 \pm 1.8	%	-5.83%	
	Vertical & Horizontal static	Ti6Al4V	2	UTS	885 \pm 22	833 \pm 23	MPa	+6.24%	
		Arc rotation		YS	818 \pm 25	785 \pm 26	MPa	+4.20%	
				δ	11.8 \pm 1.9	12 \pm 1.8	%	-1.67%	

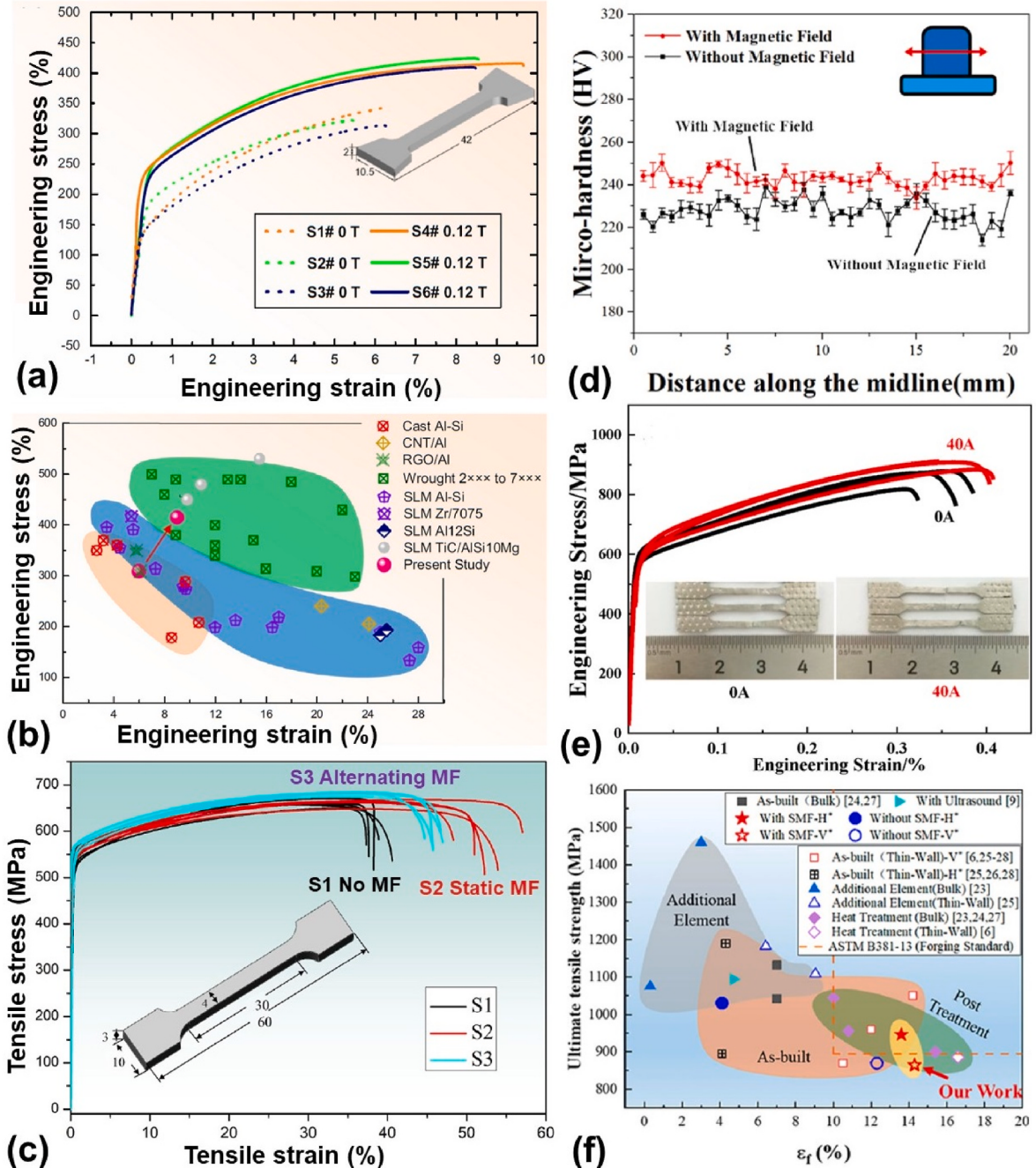


Fig. 10. Effect of auxiliary magnetic field (MF) on mechanical properties of AM-processed different materials. (a) LPBF-processed AlSi10Mg alloys without MF and with a 0.12 T static MF [45], (b) the LPBF-processed AlSi10Mg alloys assisted by MF compared with the literature [45], (c) the comparison of the LPBF-processed SS316 alloys without and with (static and alternating) MFs [47], (d) the hardness of WAAM-processed Inconel 625 with and without a static MF [52], (e) WAAM-processed Inconel 718 with and without MF [53], and (f) LDED-processed Ti6Al4V alloys with a static MF, showing better ductility but a weaker strength [49].

atoms O and C) is the primary concern due to the direct contact between the ultrasonic head and the deposited material.

Notably, acoustic streaming and cavitation are the two main mechanisms contributing to the interaction between AF and materials [78]. Among them, the cavitation effect is the main factor that affects microstructural refinement. In the USV-assisted AM process, ultrasound can induce cavitation into the melt pool, thereby breaking up dendrites and acting as a heterogeneous nucleation catalyst during crystallization, as shown in Fig. 12a. The degree of cavitation is mainly affected by the ultrasonic intensity I , which is defined by Ref. [72]:

$$I = \frac{1}{2} \rho c (2\pi f A)^2 \quad \text{Eq. (6)}$$

where ρ , c , f , A represent the density of melt metals, the sound velocity in the liquid, the angular frequency of the ultrasound and the oscillation amplitude, respectively. The angular frequency of the ultrasound and the oscillation amplitude both positively determine the ultrasonic intensity. To achieve significant microstructural refinement, the ultrasonic intensity should be higher than the threshold required for cavitation in molten metals ($\sim 100 \text{ W cm}^{-2}$ for light metals [79]). According to the characteristics of ultrasound waves, the amplitude A of the USV can be

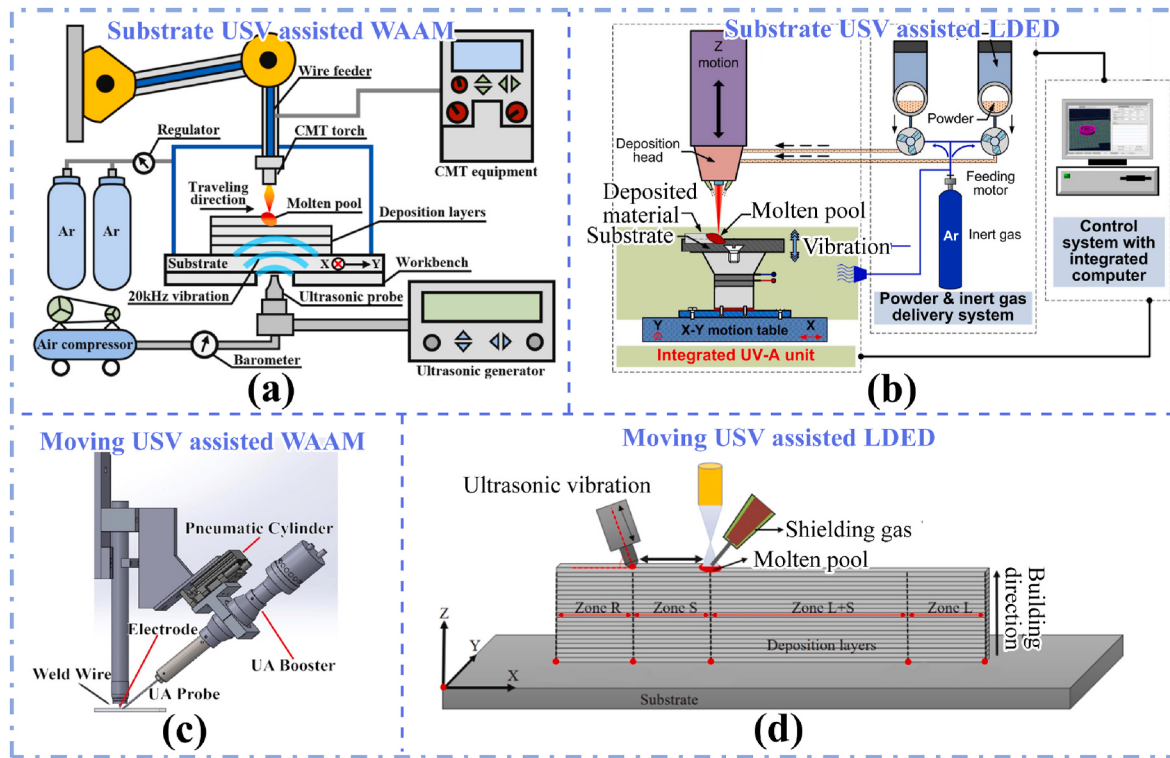


Fig. 11. Additive manufacturing with the auxiliary acoustic field. (a) Substrate ultrasonic vibration (USV)-assisted WAAM [73], (b) substrate USV-assisted LDED [76], (c) moving USV-assisted WAAM [77], and (d) moving USV-assisted LDED [74].

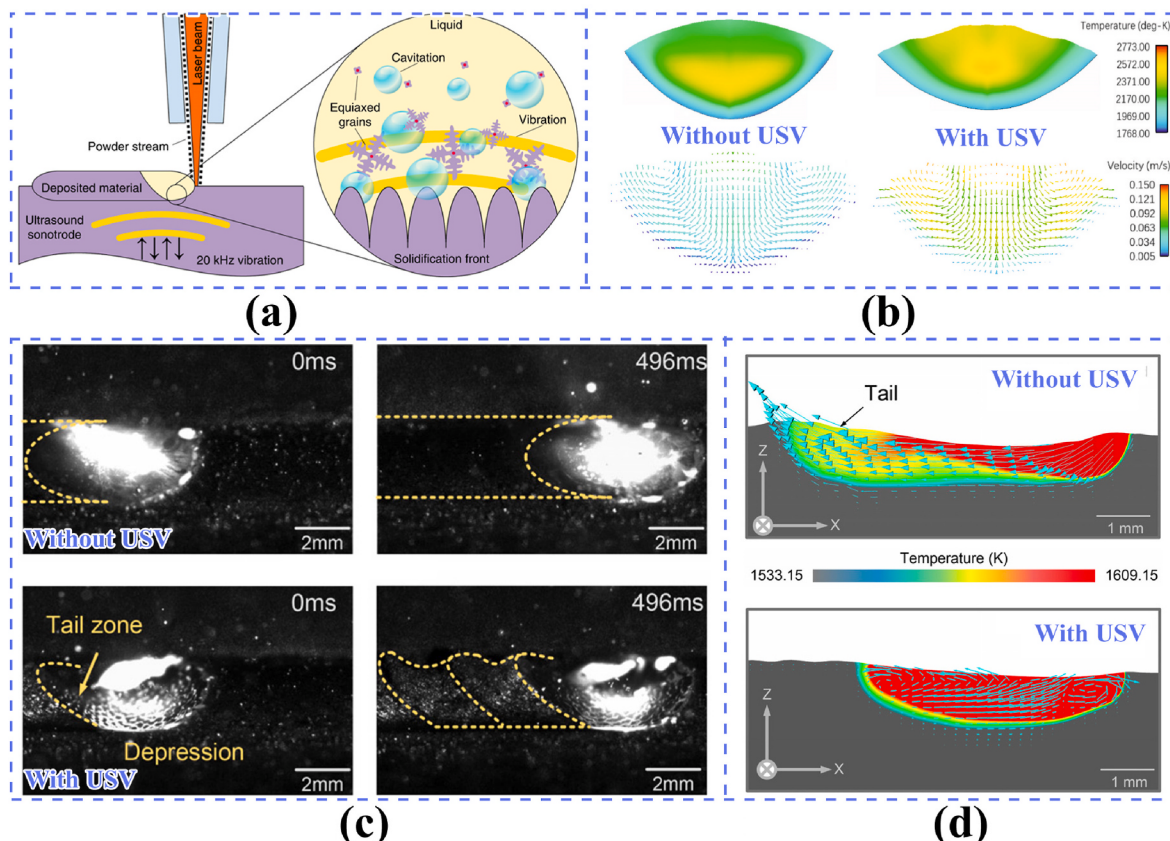


Fig. 12. Effects of auxiliary acoustic field on the melt pool dynamics. (a) Schematic of USV-assisted AM [72], (b) simulation results of temperature field and flow field in the melt pool [78], (c) snapshots of the melt pool and (d) the corresponding flow field simulation [81].

calculated by:

$$A = A_0 \cos \frac{2\pi f}{v} d \quad \text{Eq. (7)}$$

where A_0 denotes the amplitude at the sonotrode working face, v is the sound velocity in the materials, and d is the distance from the ultrasound sonotrode. Due to the collapse of cavitation bubbles during USV, pressure will be generated in the melt pool. Based on Eq. (7), the internal sound pressure (P_{sound}) generated at a certain location of the melt pool can be calculated by Ref. [79]:

$$P_{sound} = \rho c v = \rho c 2\pi f A_0 \cos \frac{2\pi f t}{v} \quad \text{Eq. (8)}$$

where t is the time for ultrasonic action in the melt pool. Notably, the undercooling degree (ΔT_m) is affected by the P_{sound} to a large extent [80]:

$$\Delta T_m = \frac{T_m(V_L - V_S)P_{sound}}{\Delta H} \quad \text{Eq. (9)}$$

where T_m , ΔH , V_L and V_S are the theoretical crystallization temperature, the latent heat of phase transformation, the volume per unit mass of the solid and liquid phases, respectively. Based on Eq. (8) and Eq. (9), the increase in the f and A is favourable for achieving higher undercooling. The higher undercooling can further increase the nucleation rate during AM, refining the grains significantly. The threshold value of sound pressure (P_B) for ultrasonic cavitation can be calculated by Ref. [74]:

$$P_B = P_0 - P_v + \frac{2}{3\sqrt{3}} \left[\frac{\left(\frac{2\sigma}{R_0} \right)}{P_0 - P_v + \frac{2\sigma}{R_0}} \right]^{1/2} \quad \text{Eq. (10)}$$

where P_0 , P_v , σ , R_0 are the liquid static pressure, the saturation vapour pressure, the surface tension coefficient, and the initial radius of the bubble, respectively. For achieving significant microstructural refinement, both the ultrasonic intensity and sound pressure should be higher than the threshold required for cavitation in molten metals.

Apart from the cavitation effects, acoustic streaming is another crucial factor which plays an important role in the solidification process. Notably, an ultrasound-induced inertial force (S_u) could be induced into the melt pool during USV, and the S_u can be calculated by the following equation [81]:

$$S_u = -\rho f^2 A \sin(f t) \quad \text{Eq. (11)}$$

The inertial force of the ultrasound can stir and mix the melt pool, thereby accelerating the flow rate, increasing the diffusion rate and reducing the temperature gradient of the melt pool, as shown in Fig. 12b [78]. Therefore, the USV can homogenize the distribution of alloying elements and alleviate the thermal stress of deposited material. The degree of acoustic streaming is also positively related to the ultrasonic intensity and the direction of USV. For USV-assisted AM, the ultrasound is generally implemented in the vertical direction for achieving sufficient cavitation and acoustic streaming effects. In terms of the melt pool flow characteristics, Yang et al. [81] reported that the inertial force generated by the USV drives the melt pool to flow forward and backward along the scanning direction, which leads to the bulge and depression appearing alternately on the surface of the melt pool shown in Fig. 12c. According to the corresponding flow field simulation result in Fig. 12d, the tail region of the melt pool decreases with the application of auxiliary USV. In addition, the USV can also enlarge the melt pool during AM because the USV generate a higher temperature in the melt pool and promote Marangoni convection which was proportional to the square of the melt pool size [76].

3.2. Effect of acoustic field on densification

In terms of densification, the proper auxiliary USV treatment can reduce the internal micro-pores and micro-cracks within the deposited material. The main reason is that the fluidity of the melt pool can be increased by the acoustic field due to the induced acoustic streaming and stirring effects. Therefore, gas bubbles easily float upward and escape from the melt pool before solidification, which reduces porosity significantly. It is reported that acoustic streaming plays a dominant role in affecting porosity, especially under a large ultrasonic amplitude [80]. The USV also leads to a more uniform temperature distribution in the melt pool, which helps prohibit the formation of micro-cracks. For instance, Ning et al. [82] reported that the application of USV reduced the porosity of the LDED-built 17-4 PH steel from 0.68% to 0.35%, as shown in Fig. 13a. Similar effects have also been reported in LDED-built AISI 630 steel where the application of USV reduced the internal micro-pores and micro-cracks (Fig. 13b). Todaro et al. [83] studied the influence of USV on defect formation in the LDED-built 316 L steel (Fig. 13c), and the defect-free 316 L samples can be obtained with proper USV assistance. Additionally, the USV also demonstrated the capability to improve the relative density of metal matrix composites. As shown in Fig. 13d, the large pores in the LDED-built Ti-TiB composites are drastically reduced by the application of USV [84].

3.3. Effect of acoustic field on microstructural evolutions

3.3.1. Grain refinement and CET

As previously discussed, auxiliary USV can bring ultrasonic cavitation and acoustic streaming effects to the melt pool, promoting nucleation and crystallite formation during AM [74,75,81]. The cavitation bubble cloud mechanically breaks the dendrites into pieces during solidification and promotes grain nucleation and refinement [76,85,86]. As a result, both grain refinement and CET have been reported in various AM-built alloys with auxiliary USV [72,83,87,88], and the ultrasonic frequency and amplitude play a decisive role in the degree of grain refinement [87,89]. Wang et al. [87] investigated the effect of auxiliary USV on the microstructure and mechanical properties of an LDED-built Inconel 718 alloy. As presented in Fig. 14a, the cellular size of the Inconel 718 alloy was refined significantly with auxiliary USV. Meanwhile, the Laves phase of the Inconel 718 alloy changed from long columnar shape into spherical particles. For USV-assisted LDED-built Ti6Al4V, Todaro et al. [72] documented that the CET and grain refinement of prior-β grains and α lath were achieved, as shown in Fig. 14b. Similarly, Zhang et al. [88] report grain refinement through the deployment of USV in the LDED of an Al-12Si alloy, in which the grain size of the primary α-Al was refined from 277.5 μm to 87.5 μm.

3.3.2. Texture alleviation

Due to the high thermal gradient along the build direction (BD), the predominant <001>/BD texture is a common feature for most AM-built metallic parts that will result in undesirable mechanical anisotropy [90]. To address this challenge, USV treatment has been adopted as a feasible solution for alleviating the predominant <001>/BD texture. For instance, the grains of the LDED Inconel 625 alloys and 316 L stainless steels showed more random orientations with auxiliary ultrasound, i.e., the <001> texture was weakened significantly in the two alloys as observed from the corresponding {001} pole figures (Fig. 14c and d) [72,83]. Similar results were also found in ER321 stainless steel processed by USV-assisted LDED [75]. This can be attributed to the high nucleation rate and dendrite-tip fragmentation caused by USV-assisted AM, which suppresses the typical epitaxial growth along BD by enabling nucleation ahead of the solidification front through the dendrite tips, essentially acting as a nucleation agent.

3.3.3. Uniform dispersion of alloy elements and reinforcements

For AM-built Ni-based superalloys, the elemental micro-segregation

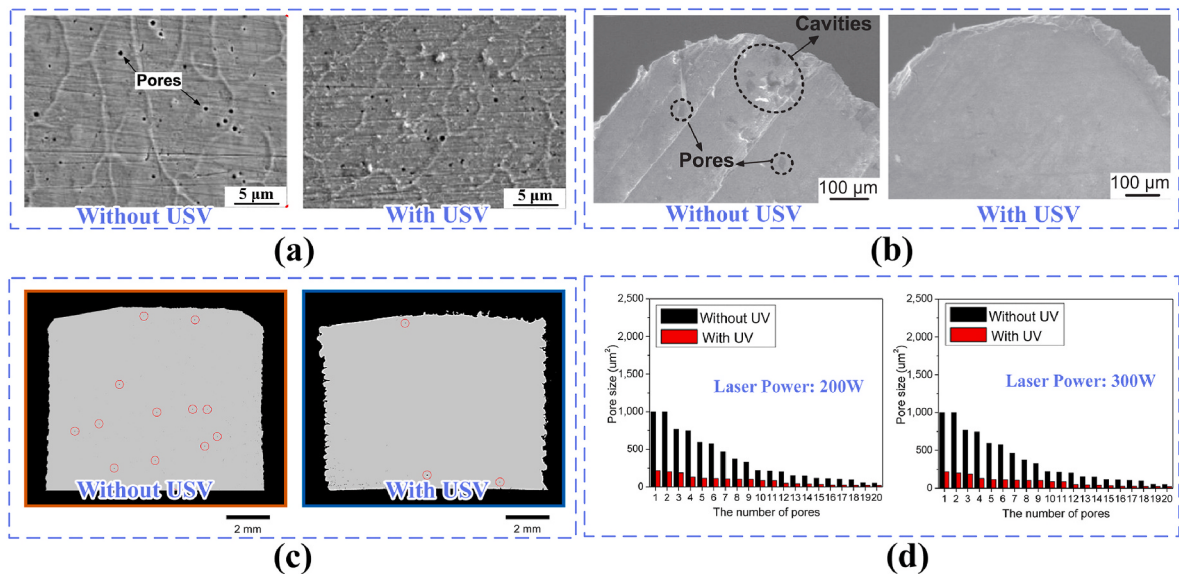


Fig. 13. Densification behaviour of the AM fabricated parts with auxiliary ultrasonic vibration (USV). (a) Comparisons on porosity of LDED-built 17-4 PH steel without and with USV [82], (b) comparisons on porosity of LDED-built AISI 630 steel without and with USV [76], (c) comparisons on porosity of LDED-built 316 L without and with USV [83], and (d) variations of pore size of LDED-built Ti-TiB composite without and with USV [84].

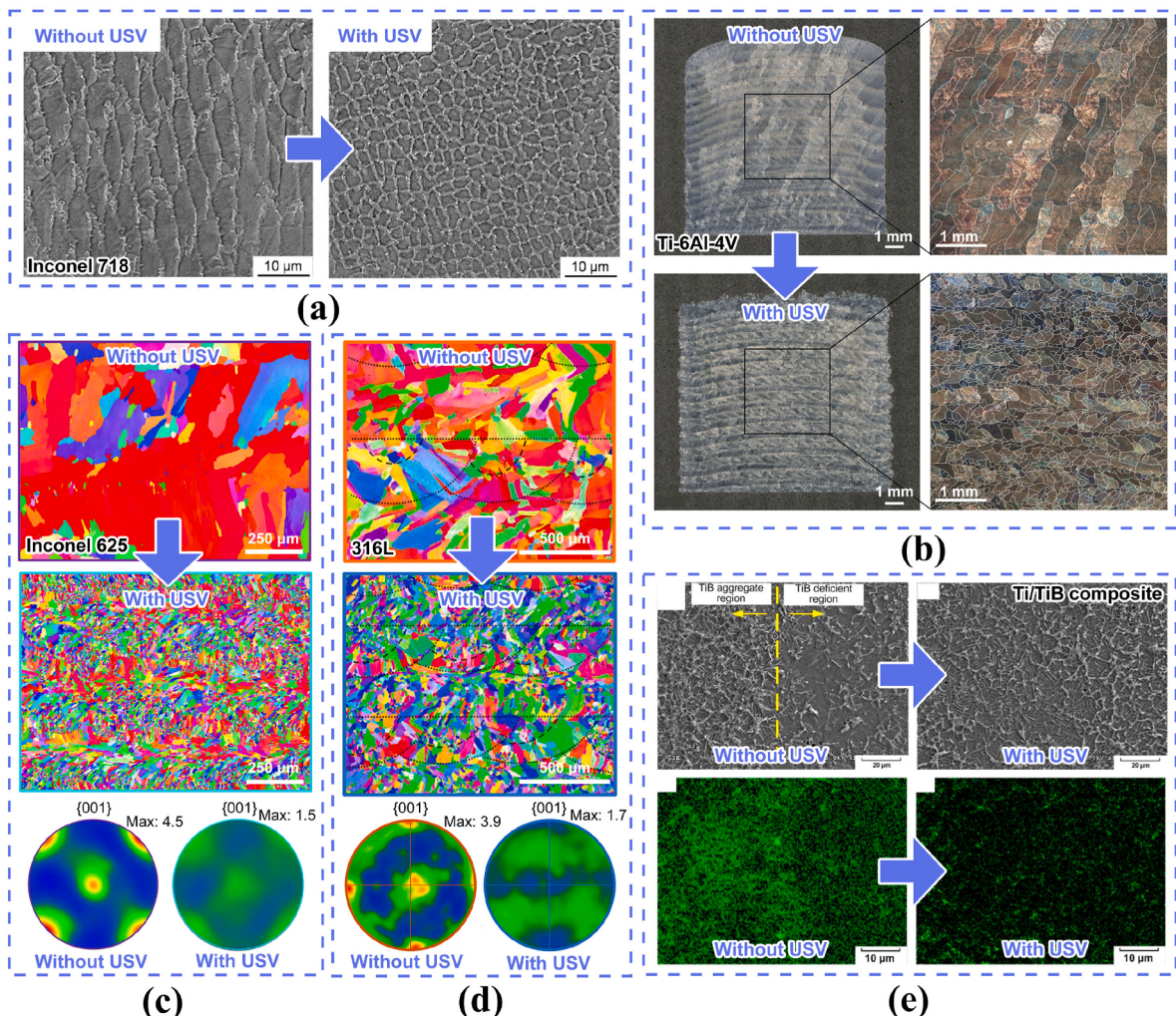


Fig. 14. Effects of auxiliary ultrasonic vibration (USV) on the microstructure of the LDED-built (a) Inconel 718 [87], (b) Ti6Al4V [72], (c) Inconel 625 [72], (d) 316 L [83] and (e) Ti/TiB composite [84].

is still a challenge that needs to be resolved. Due to the micro-segregation of Nb and Mo, the Laves phase typically forms in these alloys during solidification, which deteriorates their mechanical properties [91]. To this end, Chen et al. [73] adopted an auxiliary USV in a WAAM-built Inconel 625 alloy. Interestingly, the dissolution of the Nb element is promoted, suggesting that the ultrasound reduces the elemental segregation in the alloy. This may be attributed to a combination of factors; the increased equiaxed growth ahead of the melt pool will result in finer interdendritic structures and therefore smaller regions of interdendritic fluid high in Nb and lower percentages of Laves phase. Additionally, the enhanced mixing promoted by the USV field will also offset the formation of a fluid of different elemental composition ahead of the solidification front.

The application of USV fields in particle-reinforced metal matrix composites has also shown a lot of promise in reducing the agglomeration of reinforcements which is still a common challenge when processing these materials [92,93]. With USV assistance, the dispersion of reinforcement particles in metal matrix composites can be more uniform [94]. For instance, Ning et al. [84] adopted the auxiliary USV in the LDED of Ti-TiB composites and reported that the application of USV promoted the dispersion of TiB whiskers effectively (Fig. 14e). This is because the USV-induced shear force breaches the TiB agglomerates during deposition. In fact, grain refinement and quasi-continuous network-shaped TiB microstructures were achieved in the Ti/TiB composite with auxiliary USV, as shown in Fig. 14e. Due to the improved dispersion of reinforcements and grain refinement, the hardness of the Ti/TiB composite was also enhanced efficiently.

3.4. Effect of acoustic field on mechanical properties

As the application of auxiliary USV can reduce porosity, alleviate residual stress and refine the grains of AM-processed metals and alloys, the mechanical properties (e.g., strength, ductility, and hardness) are also positively affected. These have been summarized in Table 2. Ning et al. [82] studied the effect of USV on the LDED-built 17-4 PH steel and reported that the hardness of the steel was enhanced by the USV as a result of the reduced porosity and grain refinement, as exhibited in Fig. 15a. Todaro et al. [72] reported that the yield strength and ultimate tensile strength of the LDED-built Ti6Al4V alloy was enhanced by 12% (Fig. 15b) without noticeable reduction in ductility with auxiliary USV. Wang et al. [87] proposed that the ultrasonic frequency plays a significant role in the strengthening efficiency of the LDED-built Inconel 718, and the hardness of the material increases with an increase in ultrasonic

frequency, as shown in Fig. 15c [87]. Yang et al. [81] employed the USV alternately in an LDED-built Inconel 718 alloy, and an alternating coarse- and fine-grained microstructure was formed, enhancing the YS by 28% without an evident reduction in ductility (Fig. 15d). In addition, Yuan et al. [75] reported that the YS of ER321 stainless steel built by LDED was enhanced by 11.9% under the auxiliary USV (Fig. 15e). The underlying mechanisms are related to the weakened texture strength and homogenized grain structure.

For most AM fabricated parts, mechanical anisotropy exists between the build and transverse directions, originating from the strong texture and the columnar grain morphology formed by the large thermal gradient along the BD. Thanks to the weakened texture and CET, the mechanical anisotropy of AM-built parts can also be alleviated effectively with the auxiliary USV. As shown in Fig. 15f, the mechanical anisotropy of the USV-assisted WAAM-built Inconel 625 alloy was reduced significantly compared to the same alloy without the USV treatment [73], which is attributed to the weakened texture intensity and the formation of fine equiaxed grains.

4. Thermal field assisted additive manufacturing (T-FAAM)

Thermal field, also known as auxiliary heating, is the most common auxiliary energy field used to improve the process stability of metal AM. This section reviews the work principle of various thermal field (TF) assisted metal AM techniques. Moreover, the effects of the auxiliary thermal field on the densification behaviour, residual stress, microstructure and mechanical properties of the AM fabricated materials are discussed systematically.

4.1. Work principle of thermal field in additive manufacturing

According to the different objects being heated, the T-FAAM can be divided into three categories, i.e., substrate heating, raw material heating and deposited material heating. The features of these T-FAAM techniques and their applications are summarized in Table 3.

4.1.1. Substrate heating

Substrate heating is the most common approach for altering the temperature field during deposition and has been widely incorporated into most metal AM routes (e.g., LPBF, LDED, and WAAM). Considering that low-temperature substrate heating (typically ≤ 200 °C) is common in many commercial AM equipment, this review will mainly focus on high-temperature (i.e., >300 °C) substrate heating as it can serve as a

Table 2
Mechanical properties of AM fabricated parts with auxiliary acoustic field (AF).

AM	Auxiliary USV	Material	Frequency (kHz)	Amplitude (μm)	Mechanical property	Property with AF	Property without AF	Units	Property difference	Ref
WAAM	Substrate USV	AISI 630 steel	20	NM	YS	972.3	447.0	MPa	117.5%	[76]
					UTS	2204.5	904.3	MPa	143.8%	
					δ	9.99	4.80	%	108.1%	
	Substrate USV	Inconel 625	20	50	YS	431.3	379.2	MPa	13.7%	[73]
LDED	Substrate USV	Ti6Al4V	20	30	UTS	747.8	666.9	MPa	12.1%	
					δ	65.0	63.2	%	2.8%	
					YS	1094	980	MPa	11.6%	[72]
					UTS	1137	1015	MPa	12.0%	
LDED	Substrate USV	Inconel 718	19.8	10	δ	4.7	5.1	%	-7.8%	
					YS	551.5	428.6	MPa	28.7%	[81]
					UTS	831.2	722.8	MPa	15.0%	
					δ	36.8	37.7	%	2.4%	
LDED	Substrate USV	AISI 630 steel	NM	NM	YS	974.0	449.2	MPa	116.8%	[82]
					UTS	2203.8	905.7	MPa	143.3%	
					δ	9.96	4.79	%	107.9%	
	Substrate USV	Inconel 718	41	5	Hardness	280.6	236.1	HV	18.8%	[89]
Moving USV	ER321 steel	20	16	YS	367	328	MPa	11.9%		
				UTS	663	646	MPa	2.6%		
				δ	60	59	%	1.7%		

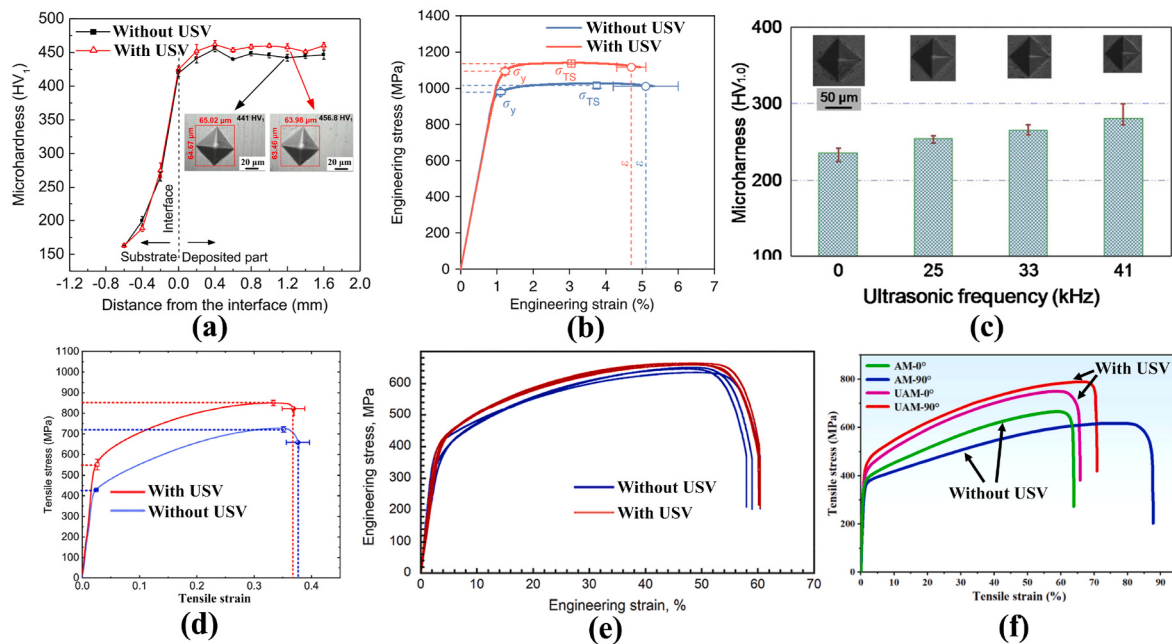


Fig. 15. Effects of auxiliary ultrasonic vibration (USV) on the mechanical properties: (a) the hardness of LDED-built 17-4 PH steel without and with USV [82], (b) the tensile properties of LDED-built Ti6Al4V alloy without and with USV [72], (c) the effect of USV on the microhardness of the LDED-built Inconel 718 alloy [87], the tensile properties of the (d) LDED-built Inconel 718 alloy [81], (e) LDED-built ER321 steel [75] and (f) WAAM-built Inconel 625 alloy [73] without and with USV (UAM represent the USV-assisted WAAM).

Table 3
Summary of thermal fields used for assisting metal AM.

Thermal fields	Heating methods	Applications	Advantages	Disadvantages	Ref.
Substrate heating	Resistance/Induction heating	Reduce thermal gradient, alleviate thermal stress and crack sensitivity.	Simple set-up, wide applicability and low cost.	Not suitable for fabricating tall components.	[19, 95]
Raw material heating (Hot-wire)	Arc heating	Increase deposition rate and energy efficiency. Reduce the demand for high laser power.	High heating efficiency, low cost and wide applicability.	The arc light of the arc striking part is harmful to the operator's skin.	[16]
	Resistance heating	Increase deposition rate and energy efficiency. Reduce the demand for high laser power.	Simple set-up, great controllability and safety.	Poor process stability due to arc spatter.	[16]
	High-frequency induction heating	Increase deposition rate and energy efficiency. Reduce the demand for high laser power.	Rapid heating rate, high accuracy and low consumption	High cost.	[16]
Deposited material heating	Hybrid-source heating	Reduce thermal gradient and cooling rate. Improve process stability.	High flexibility and high adaptability.	Complex set-up and high cost.	[20, 96, 97]
	In-situ induction heating	Reduce thermal gradient and cooling rate. Improve deposition rate.	High flexibility.	High cost.	[98, 99]
	In-situ laser diodes heating	Alleviate thermal stress and crack sensitivity.	High flexibility.	High set-up complexity and high cost.	[100, 101]

more useful auxiliary heat source. A typical schematic of the substrate heating is presented in Fig. 16a, and the substrate heating can be held before or during deposition. The substrate heating process is known to reduce the temperature gradient during AM, thereby alleviating thermal stress and crack sensitivity. Besides, it could also increase the deposition rate [19, 95]. The substrate's heat source can be either resistance heating or induction heating. The advantages of the substrate heating process are the simple set-up, broad applicability and low-cost. However, the limitation is that the temperature will drop rapidly with an increased build height, and therefore substrate heating is not suitable for the fabrication of tall parts.

4.1.2. Raw material heating

In contrast, raw material heating could overcome the spatial limitation of components faced in substrate heating. Raw material heating is mainly adopted in the wire-feed AM processes, i.e., wire-feed LDED and WAAM processes, also known as the hot-wire process [104, 105]. The

hot-wire process was initially developed for gas tungsten arc welding/cladding and is now utilized as an auxiliary thermal field for wire-feed AM processes [15, 106]. After pre-heating the raw wire material to an elevated temperature, the wire is softened before being delivered to the melt pool, thus improving the tolerance of the wire to different feeding angles and positions. This could also reduce the demand for high laser power to form a stable melt pool in wire deposition, improving energy efficiency (Fig. 16b) [16]. Based on the different heat sources, the hot-wire process can be further divided into arc hot-wire, resistance hot-wire, and high-frequency induction hot wires [16]. The advantages and disadvantages of these processes are listed in Table 3.

4.1.3. Deposited material heating

The deposited material heating aims to heat the deposited object during material deposition. Three kinds of deposited material heating methods have been reported: (i) hybrid-source heating [107], (ii) in-situ induction heating [108] and (iii) in-situ laser diode heating [100].

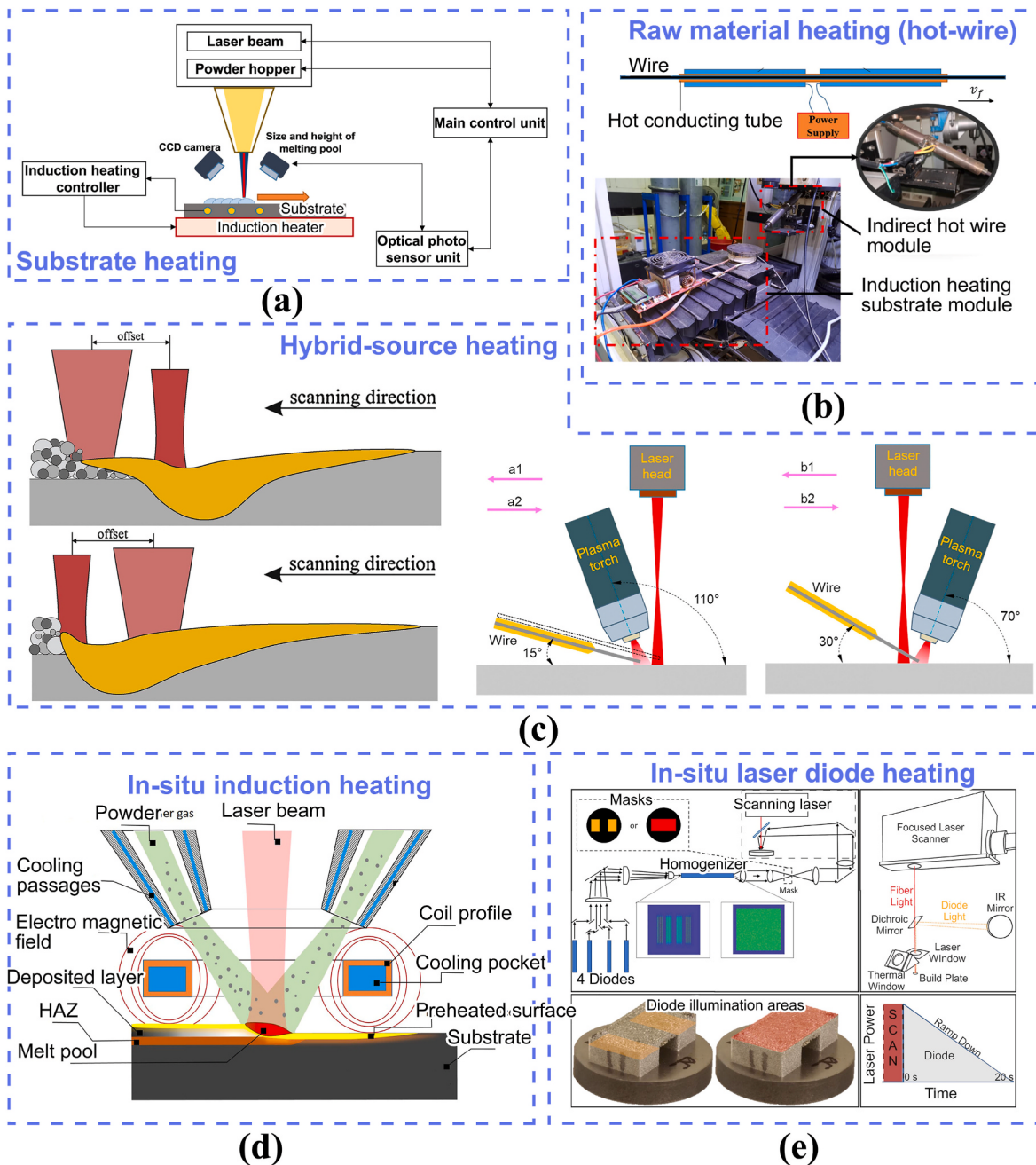


Fig. 16. Additive manufacturing with the auxiliary thermal field. (a) substrate heating [102], (b) hot-wire process [16], (c) hybrid AM process [96,97], (d) in-situ induction heating [103], and (e) in-situ laser diodes heating [100].

The hybrid-source heating in AM process means that one or more auxiliary heat sources (laser beam/plasma arc) are integrated into the regular AM system [107]. Notably, the hybrid-source heating in AM is similar to dual-beam laser welding, in which the use of auxiliary beams is well established for pre-heating [109] or post-heating [110] the surface and hereby improving the welding quality. The metallurgical characteristics of dual-beam welding are very similar to the dual-beam AM, which could provide significant guidance for hybrid-source heating in AM. Up to now, several combinations of hybrid heat-source AM processes have been reported, for instance, arc-assisted LDED [96], laser-assisted WAAM [20], and secondary laser-assisted LPBF [97]. During the hybrid heat-source AM process, the auxiliary heat source is adopted to tailor the temperature field in and around the melt pool (Fig. 16c). Generally, a lower-power energy source is for auxiliary heating, while the higher-power energy source is for melting. Two

scanning strategies for the hybrid heat-source AM process exist, as shown in Fig. 16c. If the auxiliary heat source scans in front of the main heat source, the auxiliary heat source will pre-heat the vicinity area of the melt pool. Otherwise, if the main heat source moves first, the auxiliary heat source will serve as an in-situ annealing treatment to homogenize the temperature field and reduce the thermal gradient and cooling rate. The merits of the hybrid heat-source AM mainly include improved control flexibility, reduced distortion, improved quality, and higher build efficiency. However, it also has some limitations, including increased process complexity and high equipment cost.

In-situ induction heating and in-situ laser diode heating have also been reported as possible auxiliary heat sources. Fan et al. [98] investigated the in-situ induction heating assisted LDED by adding a moving heating coil around the laser beam (Fig. 16d). Compared with the widely adopted substrate pre-heating method, the in-situ induction heating

during AM exhibits much higher flexibility in tailoring the thermal history, microstructure, and properties of the AM-fabricated parts. Roehling et al. [100] reported a novel in-situ laser diode heating method for the LPBF process (Fig. 16e). By illuminating the surface of the deposited alloy with laser diodes during deposition, the temperature gradient and the residual thermal stress of the fabricated parts can also be reduced effectively [101]. However, further investigation on these processes is required due to the high complexity of the equipment.

4.2. Effect of thermal field on densification

Eliminating cracks is one of the major motivations for applying a thermal field. The basic mechanism is that the auxiliary thermal field can reduce the thermal gradient and cooling rate, thereby making the temperature field more uniform and alleviating the thermal stress of the deposited sample during AM. For instance, Kempen et al. [111] reported that the cracks in LPBF M2 tool steel parts have been diminished by preheating the substrate to 300 °C due to the reduced thermal gradient and cooling rate. Meanwhile, the grain size will be increased by the auxiliary thermal field, which also contributed to a higher cracking resistance.

Tungsten is a typical refractory metal with exceptional high-temperature properties. However, it has long suffered from its intrinsic high ductile-to-brittle temperature (200–400 °C) and thus is difficult to be fabricated by AM [112]. To address this challenge, substrate pre-heating has been adopted to improve the relative density and printability of tungsten. Ievković et al. [113] proposed that substrate pre-heating can be used to prevent the crack formation of the LPBF-built pure tungsten, but pre-heating up to 400 °C is not sufficient. In another work, Müller et al. [114] investigated the LDED processed tungsten by pre-heating the substrate up to 600–1000 °C, and the results indicate

pre-heating up to 1000 °C is more beneficial for material consolidation and crack mitigation (Fig. 17a). This phenomena can be attributed to that the high-temperature preheating avoids the ductile-to-brittle transformation during AM and thereby eliminating most of the cracks.

In addition, auxiliary heating is also a promising solution to inhibit cracking encountered in Ni-based alloys, such as IN738LC and Hastelloy. For instance, Xu et al. [115] fabricated IN738LC alloy through LDED combined with substrate heating at elevated temperatures (800–1050 °C) and reported that the total crack length was reduced significantly, as shown in Fig. 17c. The reason can be attributed to the reduced thermal stress and reduced precipitation rate of γ' phase, which reduced the shrinkage stress during LDED. Similarly, Mertens et al. [19] studied the effects of the substrate heating on the LPBF-built Hastelloy X alloy and reported that pre-heating at 400 °C not only diminishes the cracking but improves the relative density as well (Fig. 17d).

WAAM-built Al alloys suffered from the formation of pores after solidification, which originated from hydrogen contaminants of the wire surface. To address this challenge, Fu et al. [15] adopted the hot-wire process for WAAM of 2024 Al alloy, and the porosity was significantly reduced by heating the wire during deposition (Fig. 17b). The related mechanism for densification is attributed to that the hydrogen contaminants on the wire surface were evaporated by heating the wire. The hot-wire treated sample with coarse grains also exhibited less pore nucleation tendency. Meanwhile, with a proper auxiliary hot-wire process, the deposition rate of WAAM of 2024 Al alloy was increased by three times (from 86 to 301 cm^3/h). Besides, the auxiliary thermal field can also be used to eliminate the lack of fusion defects due to the extra thermal energy input. For the low-power pulsed laser wire feeding deposition, the auxiliary heating and hot-wire can eliminate the lack of fusion defects effectively [16].

In addition to improving density and eliminating cracks, the surface

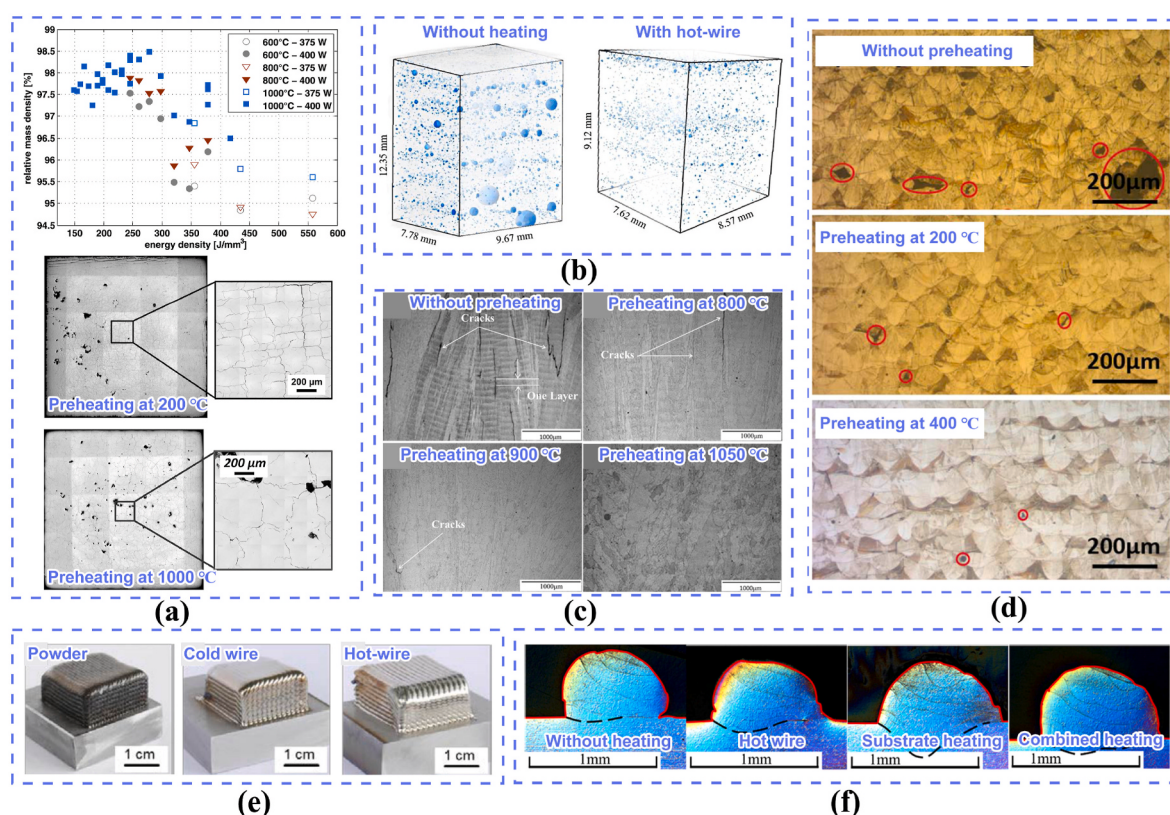


Fig. 17. Densification behaviour of the AM fabricated parts with the auxiliary thermal field. (a) Relative density and optical images of the LDED-built tungsten samples under different pre-heating temperatures [114], (b) 3D distribution of defects in the WAAM-built 2024 Al samples either with or without hot-wire process [15], and optical images of (c) the LDED-built IN738LC and (d) the LPBF-built Hastelloy X alloys under different pre-heating temperatures [19,115], and (e) the LDED-built IN718 and (f) the WAAM-built 304 L stainless steel with various auxiliary heat sources [16,17].

quality and process stability could also be enhanced through auxiliary heating. For instance, Bambach et al. [17] compared the LDED-processed IN718 alloy prepared from powder, cold-wire, and hot-wire. Due to the extra thermal energy of the hot wire, the scan speed can be doubled and thereby reducing the linear laser heat input by half. Thus, surface oxidation was avoided successfully in the hot-wire treated sample (Fig. 17e). Moreover, the deposition rate of the hot-wire process is up to $100 \text{ cm}^3/\text{h}$ which is higher than that of the cold-wire process. Sang et al. [16] investigated the effects of various auxiliary heating methods (hot-wire, substrate heating, and combined hot-wire and substrate heating) on an LDED-built 304 stainless steel, and indicated that the surface roughness and macroscopic profile accuracy of the deposited material improved significantly through combined hot-wire and substrate heating (Fig. 17f). The improvement in surface quality and macroscopic profile accuracy could be ascribed to the stable melt pool induced by the auxiliary thermal field [111]. For pure Mg built by LPBF, substrate heating also has been used to make the deposited tracks flatter and the surface smoother, which can be attributed to that the auxiliary substrate heating minimises the thermal energy required by the laser and hereby improving the wettability [116].

4.3. Effect of thermal field on residual stress

Residual stress formation is challenging for AM processing due to the intrinsic high cooling rate characterising most of the AM processes. Although post-heat treatments are widely adopted to eliminate residual stress of the deposited materials, the extremely high residual stresses generated during a build often leads to crack development of the deposited material during the process (Fig. 17c). To address this problem, an auxiliary thermal field can be incorporated into AM processing routes to reduce the thermal gradient and cooling rate, and thereby alleviating the thermal residual stress.

Ding et al. [18] studied the effects of substrate pre-heating on the residual stress of the LDED-built 12CrNi2 steel through experimental analysis and finite element simulation. The results indicated that the residual stress on the surface of the 12CrNi2 low-alloy steel decreases with an increased pre-heating temperature (Fig. 18a–f). Bai et al. [117] compared the effects of pre-heating and post-heating on residual stress of the deposited material using finite element simulation, and proposed that pre-heating is more favourable for eliminating the residual stresses (Fig. 18g and h). Ali et al. [118] reported that the residual stress of LPBF-built Ti6Al4V can be fully eliminated by pre-heating the substrate to 570°C . Roehling et al. [100] proposed that the in-situ laser diode heating can also eliminate the residual stress in the LPBF-built 316 L

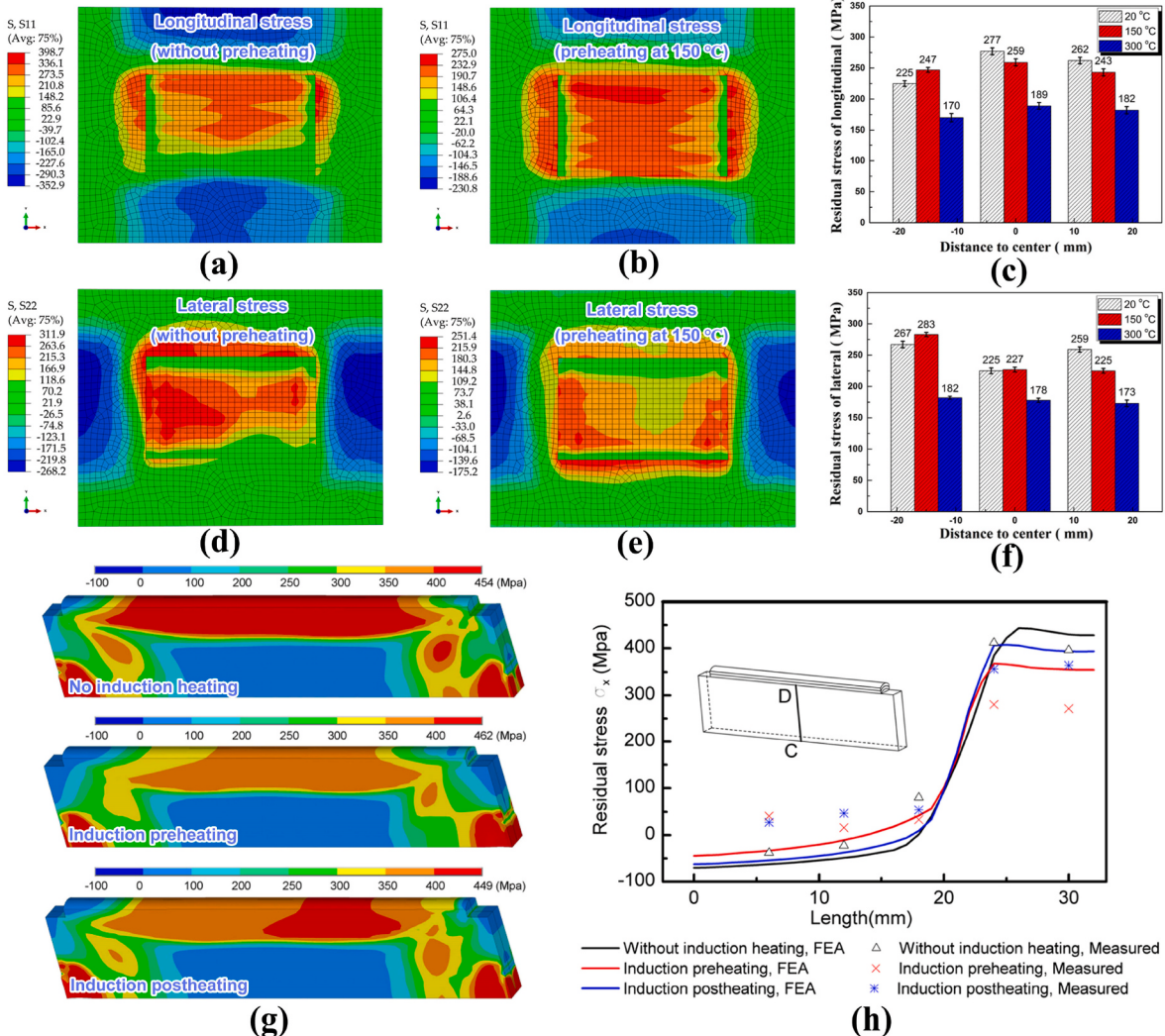


Fig. 18. Residual stress of the AM fabricated parts with the auxiliary thermal field. (a)–(f) Residual stress distribution simulation in an LDED-built 12CrNi2 low alloy steel either with and without auxiliary pre-heating [18]. (g)–(h) Residual stress distribution simulations of a WAAM-built ER70S-6 under different in-situ induction heating processes [117].

steel without evident variation in the microstructure. Fang et al. [119] proposed that the phase transition processes have a significant influence on the elimination of residual stress by auxiliary heating. For alloys with martensite transformation (e.g., Ti), pre-heating not only decreases the temperature gradient but suppresses the martensite transformation as well, thereby further reducing the residual stress effectively.

4.4. Effect of thermal field on microstructural evolutions

An optimized in-situ auxiliary thermal field can not only eliminate the defects and residual stress but also bring a more favourable microstructure to AM-processed parts. By combining an auxiliary thermal field with the AM process, it has been reported that the grain size, phase fraction, and phase morphology of the AM-fabricated alloy can be modified.

The columnar grain structure is a common microstructural feature for AM-fabricated alloys due to the prevailing solidification conditions that favour the epitaxial growth [120,121]. As the columnar-to-equiaxed transition (CET) can be achieved by decreasing the temperature gradient (G) or increasing the growth rate of the solid/liquid interface (R), auxiliary heating is considered a feasible method for inducing CET via reducing G. For instance, Xu et al. [115] reported that CET is achieved in an LDED-built IN-738LC alloy by pre-heating the substrate to 1050 °C (Fig. 19a). Li et al. [122] obtained CET in a WAAM-built Ti-6.5Al-3.5Mo-1.5Zr-0.3Si alloy through hot-wire process. As shown in Fig. 19b, the prior- β grains of the alloy became equiaxed and refined with an increased hot-wire current (i.e., increased wire temperature). The reason for the occurrence of CET can be attributed to the decreased G. Fan et al. [95] reported that in-situ induction heating is also feasible for achieving more equiaxed grains in the LDED-built Ti6Al4V alloy. By increasing the current density of the induction heating coil, the area of grains with an equiaxed morphology is enlarged significantly (Fig. 19c).

The in-situ heat treatment (IHT) effect induced by the auxiliary thermal field is another crucial factor which influences the microstructural evolution. For instance, auxiliary heating can result in an IHT of the AM-built Ti alloys [99,118,123–125]. It is known that the AM-built $\alpha + \beta$ Ti alloys are generally composed of acicular martensitic α' phase due to the high cooling rate, which generally results in a low ductility [126]. As a result, a post-heat treatment is usually required to achieve

the equilibrium $\alpha + \beta$ microstructure, minimize residual stresses and improve the ductility of the alloy [126]. However, a post-heat treatment inevitably increases the manufacturing lead time and cost; thus, auxiliary heating is a more cost-effective solution. Vrancken et al. [123] demonstrated that substrate pre-heating at even 400 °C could be used to induce the in-situ decomposition of martensitic α' in LPBF Ti6Al4V alloy. Ali et al. [118] further investigated the effects of substrate pre-heating temperature between 100 °C and 770 °C on the microstructural evolution of LPBF Ti6Al4V and reported that pre-heating at 570 °C not only promoted the in-situ decomposition of α' but also enhanced yield strength and ductility of the alloy by 3.2% and 66.2%, respectively. For the LDED Ti6Al4V alloy, Fan et al. [98] demonstrated that in-situ induction heating can also promote the decomposition of the martensite α' (Fig. 19d). The related thermodynamic and kinetic origin for the IHT of AM Ti alloys are as follows. During TF-assisted AM, the metastable phase (e.g., martensitic α') and metastable factors (e.g., dislocations, nano stacking faults) will be decomposed, which decrease the Gibbs free energy of the system. Meanwhile, the alloying elements partitioning (e.g., β -stabilizers) is also one of the main thermodynamic factors that contributed to the in-situ decomposition of α' . Besides, the kinetic origin for the in-situ decomposition of martensite α' is the thermal energy induced by auxiliary TF. In contrast from conventional post heat treatment, the IHT effects induced by applied thermal field are also highly dependent on the deposition time and deposited size, which means thermal field parameters (including heating time and temperature) should be controlled/adapted according to the size and shape of the deposited parts.

4.5. Effect of thermal field on mechanical properties

As discussed above, auxiliary heating plays a significant role in modifying the microstructure, densification, and residual stress of the AM-fabricated parts during deposition. Therefore, it is understood that the mechanical properties of the AM-fabricated part can also be modified through auxiliary heating. The mechanical properties of AM-fabricated parts under various auxiliary heating routes are summarized in Table 4, and it is clear that the mechanical properties of AM-fabricated parts can be enhanced efficiently if an appropriate auxiliary thermal field is integrated within the AM process.

As mentioned previously, auxiliary heating can be used to reduce

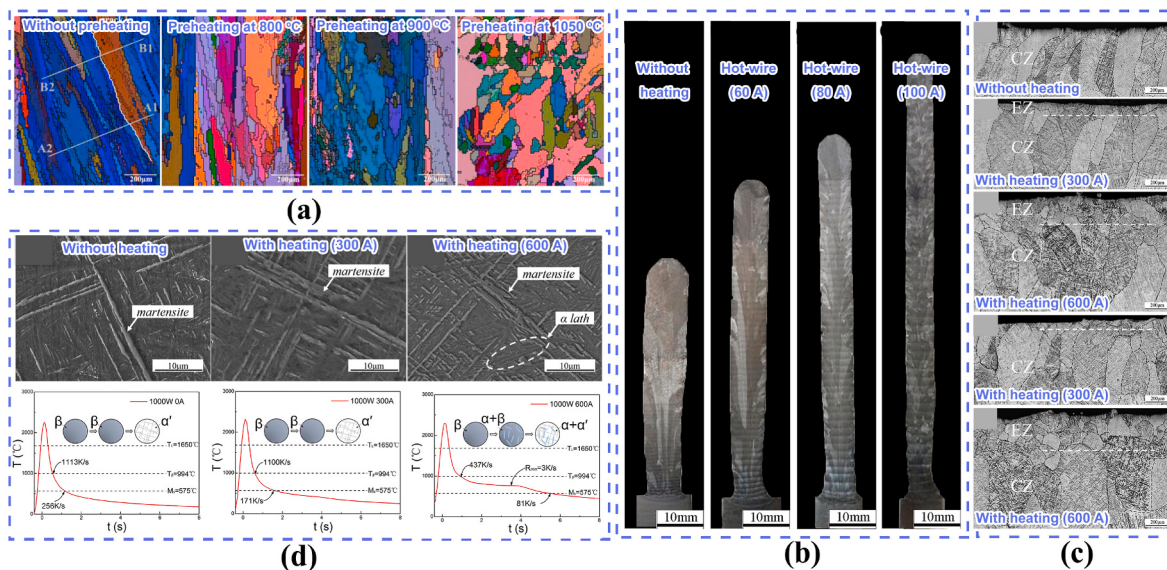


Fig. 19. Microstructure evolutions of the AM fabricated parts with auxiliary thermal field. (a)–(c) Columnar-to-equiaxed transition (CET) occurred in LDED-built IN738LC alloy [115], WAAM-built Ti-6.5Al-3.5Mo-1.5Zr-0.3Si alloy [122], LDED-built Ti6Al4V alloy [98], respectively, (d) in-situ decomposition of martensite α' in an LDED-built Ti6Al4V alloy [98].

Table 4

Mechanical properties of the AM fabricated parts with various auxiliary thermal fields.

AM	Auxiliary heating	Material	Heating temperature (°C)	Mechanical property	Property with auxiliary heating	Property without auxiliary heating	Units	Property increment	Ref
LDED	Substrate heating	AISI M4 steel	500–700	UTS	950	820	MPa	+15.9%	[102]
LDED	Substrate heating	12CrNi2 steel	150	YS UTS δ	773.1 911.1 19.8	766.4 902.3 14.9	MPa MPa %	+0.9% +1.0% +32.9%	[18]
LPBF	Substrate heating	Ti6Al4V	570	YS UTS δ	1176 1223 9.99	1139 1233 6.01	MPa MPa %	+3.2% −0.8% +66.2%	[118]
LPBF	Substrate heating	Ti6Al4V	400	YS UTS δ	1215 1280 3.9	1088 1221 6.9	MPa MPa %	+11.7% +4.8% −43.5%	[123]
LPBF	Substrate heating	Ti-5Al-5V-5Mo-3Cr	500	Hardness	463	290	HV	+59.7%	[124]
WAAM	Hot-wire	2024 Al alloy	NM	YS UTS δ	259 399 12	255 350 5.2	MPa MPa %	+1.6% +14.0% +130.8%	[15]
WAAM	Hot-wire	Ti-6.5Al-3.5Mo-1.5Zr-0.3Si	NM	YS UTS δ	840 944 12.8	810 988 9.17	MPa MPa %	+3.7% −4.5% +39.6%	[122]
WAAM	Laser-arc hybrid process	2219 Al alloy	NM	YS UTS δ	155.5 301.5 12.8	108 240 10.7	MPa MPa %	+44.0% +25.6% +19.6%	[20]
LPBF	Dual-laser hybrid process	Maraging 350 steel	NM	Hardness	471	441	HV	+6.8%	[127]
WAAM	Laser-arc hybrid process	316 L steel	NM	YS UTS δ	344 575 31.2	299 536 30.8	MPa MPa %	+15.1% +7.3% +1.3%	[21]
LDED	In-situ induction heating	Ti6Al4V	NM	Hardness	375.8	416.6	HV	−9.8%	[98]
LDED	In-situ induction heating	Ti6Al4V	NM	UTS δ	867 20.1	938 14.2	MPa %	−7.6% +41.5%	[99]

defects such as pores and cracks, alleviate residual stress, and bring IHT and CET effects during the process, and these factors directly affect the mechanical properties of the AM fabricated parts. For instance, Fu et al. [15] investigated the effects of hot-wire process on the mechanical properties of the WAAM-built 2024 Al alloy, and the results indicated that the ductility of the hot-wire assisted WAAM-built 2024 Al alloy ($\delta = 12.0\%$) is much higher than that of the alloy without hot-wire ($\delta = 5.2\%$). The related mechanism is attributed to reduced defects. Besides, the rapid in-situ heat treatment induced by the thermal field is favourable for retaining fine grain structure and achieving high mechanical performance. Graf et al. [127] fabricated Maraging 350 steel through a dual-laser hybrid LPBF process and proposed that the auxiliary laser could bring on an in-situ aging treatment to the alloy. By using a dual-laser strategy, the hardness of the LPBF-built maraging steel was enhanced from 441 to 471 HV due to the in-situ precipitation hardening. For the titanium alloy, Ali et al. [118] reported that pre-heating at 570 °C could increase the ductility of the LPBF-built Ti6Al4V alloy from 6.0% to 10.0%, and the improvement in ductility is associated with the in-situ decomposition of the martensite phase and the reduction of residual stress [128]. However, Vrancken et al. [123] reported that the excessive pickup of oxygen and nitrogen during substrate pre-heating assisted AM would be detrimental to the ductility of the AM-built alloys (especially for Ti alloys). As a result, the protective atmosphere should be carefully controlled to higher degrees during T-FAAM in view of the elevated processing temperature.

AM fabricated parts have long suffered from unfavourable mechanical anisotropy in the scanning direction and deposition direction. This could also be alleviated by integrating an auxiliary thermal field [120]. For instance, Li et al. [122] investigated the effects of the hot-wire process on the mechanical anisotropy of the WAAM-built Ti-6.5Al-3.5-Mo-1.5Zr-0.3Si alloy. With increasing the current of the resistance hot-wire to 100 A, equiaxed grains were obtained in the alloy, and the mechanical anisotropy was eliminated completely. Gong et al. [21] reported a novel oscillating laser-arc hybrid process for eliminating the

mechanical anisotropy of a WAAM-built 316 L steel. Through combining with an oscillating laser, the $\{001\}<100>$ texture of the alloy was weakened and the grains were refined as well, which eventually removed the mechanical anisotropy successfully.

5. Deformation field assisted additive manufacturing (D-FAAM)

5.1. Work principle of mechanical deformation field in additive manufacturing

In D-FAAM, an external force is applied to the deposited material to induce plastic deformation. According to the mechanical deformation configurations in AM, the D-FAAM can be categorized into three categories, i.e., rolling, machine hammer peening (MHP) and laser shock peening (LSP). A brief outline of the typical characteristics of the D-FAAM techniques is listed in Table 5.

5.1.1. Rolling-assisted AM

There are two types of rolling-assisted AM, i.e., interlayer rolling and in-situ rolling. Interlayer rolling assisted AM is a process in which a roller rolls over the deposits after each layer is completed, as illustrated in Fig. 20a. This technique is commonly used in WAAM, and the rolling force typically ranges from 15 to 75 kN [129]. The parts deposited by WAAM have large grain sizes and high-level residual stress and distortion; the subsequent interlayer rolling can improve the flatness of the weld bead and reduce the residual stress [130,131]. In-situ rolling assisted AM involves a roller that follows the energy source during AM, and the deposited metal is rolled synchronously, as shown in Fig. 20b. This process has been incorporated into WAAM and LDED [132,133]. In-situ rolling has a similar effect on the deposited materials as the interlayer rolling [134]. However, in-situ rolling has a smaller roller size and force, and the rolled material is in a semi-solid state.

Table 5

Summary of characteristics of deformation field assisted additive manufacturing (D-FAAM) techniques.

Deformation field	AM process	Advantages	Disadvantages	Ref.
Interlayer rolling	WAAM	Large rolling pressure and good stability	High set-up complexity, high cost and time-consuming.	[130]
In-situ rolling	WAAM/LDED	Low cost than interlayer rolling and good flexibility	Limited effect on reducing residual stress.	[132, 133]
Interlayer MHP	WAAM/LDED	No directional restrictions	Time-consuming and uneven strain rate.	[135]
In-situ MHP	WAAM/LDED	Good flexibility	Uneven strain rate and limited for reducing residual stress	[136, 139]
LSP	LPBF/WAAM/LDED	Ultra-high strain rate and broad applicability	High set-up complexity, high cost and time-consuming.	[138]

5.1.2. Machine hammer peening (MHP) assisted AM

In MHP-assisted AM, machine hammers are used to peen AM-deposited materials regularly to induce plastic deformation. The frequency of the hammer punch is typically up to 100 Hz, and the punching force is below 10 kN in general. There are two types of MHP used in AM, i.e. interlayer MHP and in-situ MHP. In the interlayer MHP, the rotating arm alternates the hammer and heat sources in the working position. After each layer of deposition, MHP is performed, as shown in Fig. 20c [135]. In the in-situ MHP, the hammer follows the movement of the energy beam to hammer the semi-molten metal in every track, as illustrated in Fig. 20d [136], which provides greater flexibility and efficiency than interlayer MHP.

5.1.3. Laser shock peening (LSP) assisted AM

LSP is a surface treatment technique that uses shock waves generated from rapidly expanding plasma to plastically deform a workpiece. The ablative layer is commonly used as a protective coating, in which LSP is essentially a mechanical process. The ablative layer bears the thermal load while the workpiece only experiences the shock wave. LSP can also be performed without the ablative layer. In this case, LSP becomes a thermomechanical phenomenon that leads to remelting in addition to the shock wave. Both methods can be used in combination with AM. The LSP has been used in LPBF, WAAM and LDED processes to alter the residual stress, reduce the porosity and increase the hardness. The

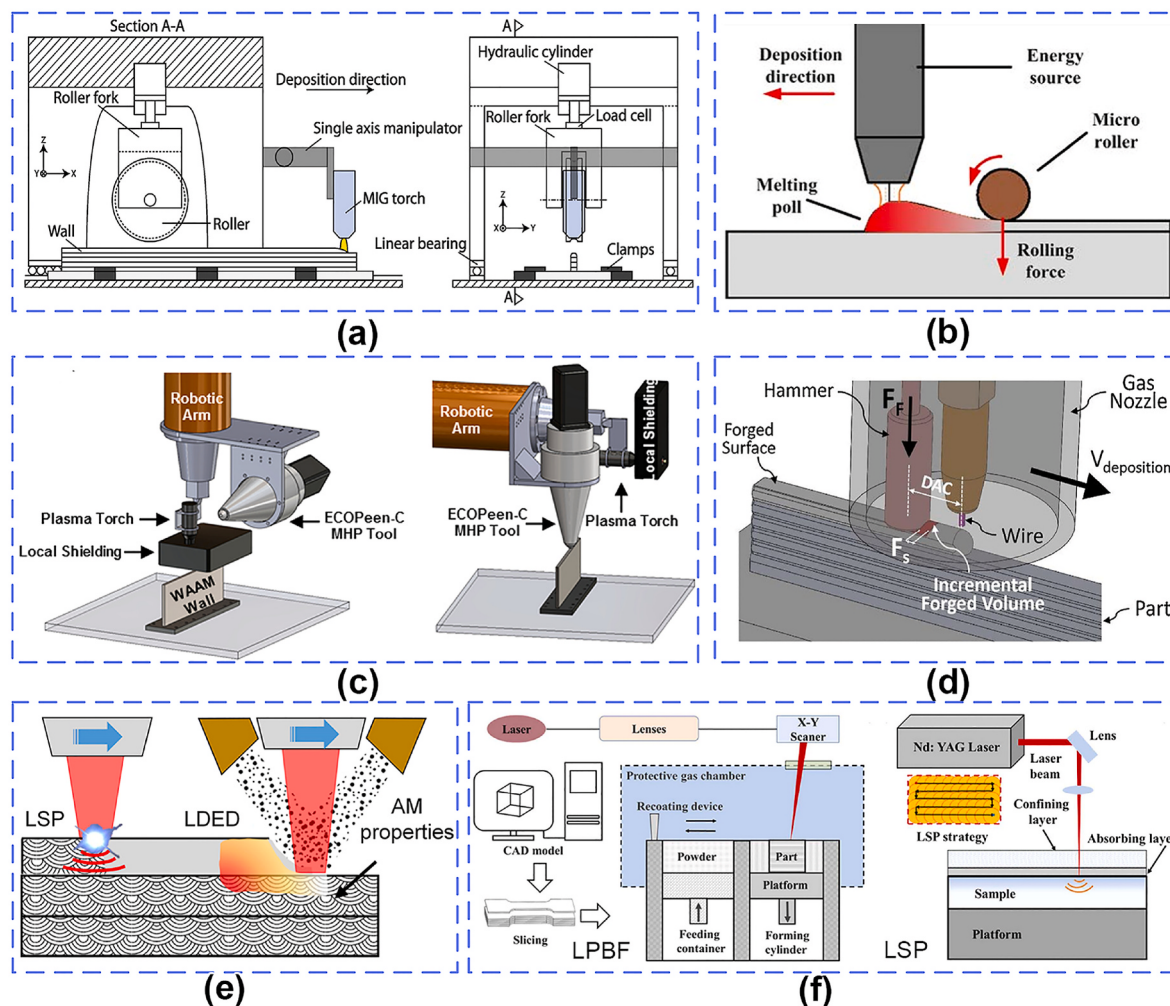


Fig. 20. Additive manufacturing with auxiliary mechanical deformation. (a) Interlayer rolling assisted WAAM [130], (b) In-situ rolling assisted WAAM [132], (c) Interlayer machine hammer peening (MHP) assisted WAAM [135], (d) In-situ MHP assisted WAAM [136], (e) laser shock peening (LSP) assisted LDED [137], and (f) LSP assisted LPBF [138].

frequency of LSP is generally no more than 5 Hz. Fig. 20e is a schematic of LSP-assisted LDED, the laser shock wave follows the energy source [137]. In the LSP-assisted LPBF, LSP is carried out on the deposited materials after each layer or several layers are finished, as shown in Fig. 20f [138].

5.2. Effect of mechanical deformation field on densification

In many cases, the auxiliary deformation can close or reduce the size of the internal pores. For rolling-assisted AM, Gu et al. [140,141] studied the influence of rolling force on the porosity of 2319 Al and 5087 Al alloys deposited by interlayer rolling-assisted WAAM. The results show that the number, volume, and size of micro-pores decreased with the

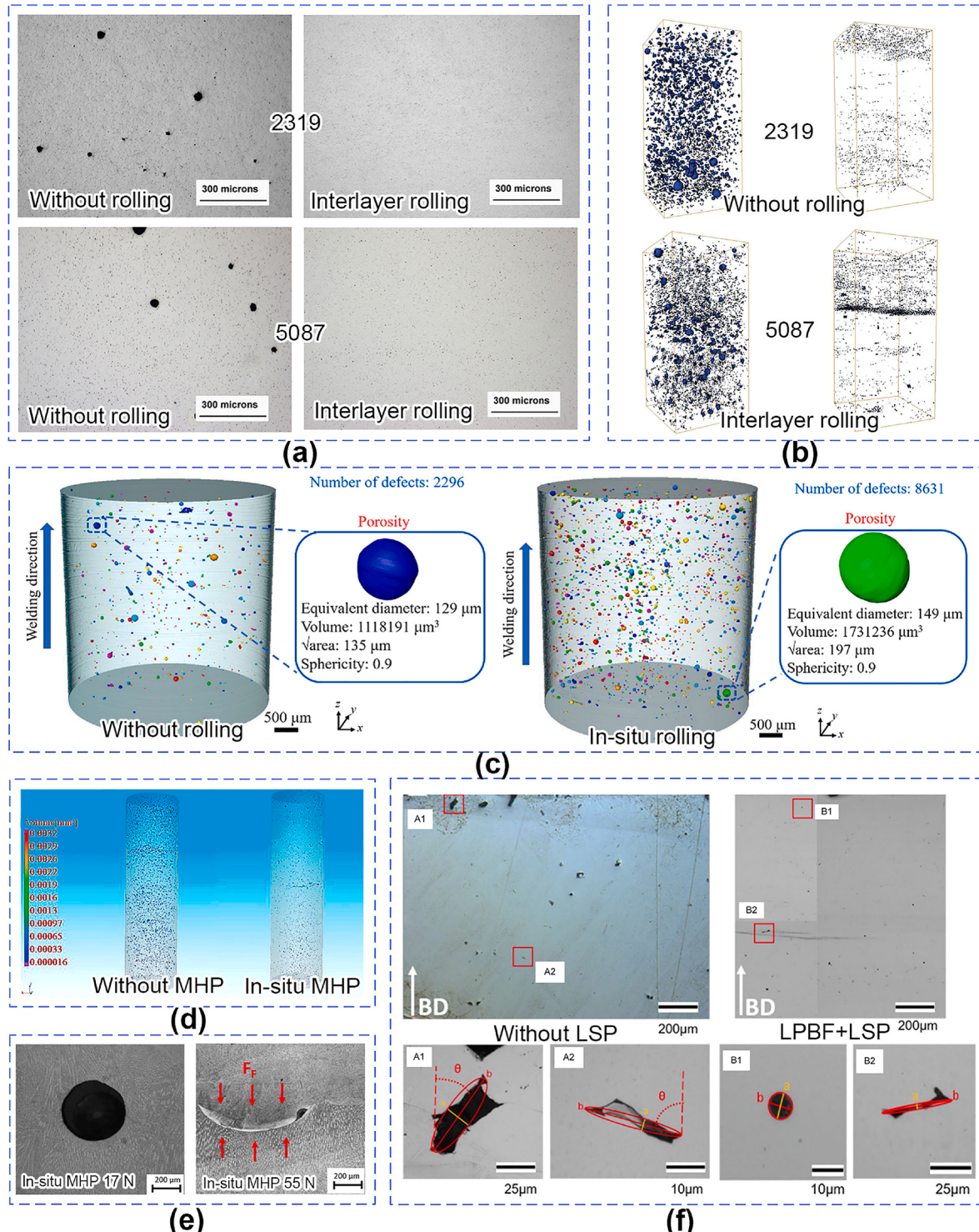


Fig. 21. Effect of auxiliary mechanical deformation on the porosity of the AM-processed metallic materials. (a) OM images of a WAAM-processed 2319 and 5087 Al alloys with and without interlayer rolling [140], (b) 3D distribution of micropores for a WAAM 2319 and 5087 Al alloys with/without interlayer rolling [141], (c) micropores for a WAAM 5087 Al alloy with/without in-situ rolling [142], (d) micropores for a WAAM 2319 Al alloy with and without MHP [143], (e) evaluation of porosity for the WAAM 316 L stainless steel with MHP [139], (f) OM image of the LPBF 316 L with and without LSP [22].

increasing loads (Fig. 21a and b). Similarly, Xie et al. [142] adopted X-ray tomography to analyze the density, morphology, distribution, and size of the defects in a WAAM 5087 Al alloy. The number and size of defects were reduced significantly by in-situ rolling (Fig. 21c).

MHP applied in AM has been demonstrated to be effective in reducing porosity. As reported by Fang et al. [143], most of the pores in WAAM 2319 Al alloy are closed after hammering, resulting in a 74% reduction of porosity (Fig. 21d). This technique can also be applied to steels, in fact, Duarte et al. [139] fabricated 316 L stainless steel by in-situ MHP-assisted WAAM, and found that the pores almost collapsed and were displaced to the periphery after hammering. The number and size of pores decreased with increasing force (Fig. 21e).

LSP also has great potential to improve the densification of AM-deposited materials. Kalentics et al. [22] deposited the 316 L stainless steel by LSP-assisted LPBF, and the results (Fig. 21f) showed that the average pore size decreased from 8.1 to 2.6 μm (reduced by 68%) in the LSP-affected zones.

5.3. Effect of mechanical deformation field on residual stress

Residual stress and distortion restrict the development of large-scale parts by AM. However, auxiliary mechanical deformation has proved to be an efficient way to alleviate internal residual stress. Martina et al. [144] demonstrated that interlayer rolling with a force of 75 kN can reduce the residual stress at the interface between deposits and substrate by 60% in Ti6Al4V walls, as shown in Fig. 22a. In-situ rolling has a limited impact on the residual stress of AM. To investigate the evolution

of stress and strain during in-situ rolling-assisted WAAM, a simulation model was established to reveal the evolution of stress and strain during in-situ rolling-assisted WAAM, which revealed that the rolling increased the strain in the weld bead and reduced the residual tensile stress on the surface (Fig. 22b) [145]. Interlayer hammering can also reduce or transform tensile residual stress into compressive stress. The residual stress profile with interlayer MHP shows an entirely compressive region, as shown in Fig. 22c. For the LSP-assisted AM, the LSP can alter the residual stress state from tensile stress to compressive stress in the LPBF processed components [146–148] and reduce the distortion of the component significantly (Fig. 22d) [149].

5.4. Effect of mechanical deformation field on microstructural evolutions

The auxiliary mechanical deformation field also brings a more favourable microstructure to AM-processed components, modifying the grain size, texture, phase morphology and dislocations.

Interlayer rolling in AM is cold working, the process causes dislocations to interact with each other through pile-up and multiplication, resulting in a significant increase in dislocation density. Xu et al. [151] studied the microstructural evolution of interlayer rolling-assisted WAAM 18Ni250 maraging steel. In the specimens without rolling, dislocations were found to be entangled in the martensitic laths. After rolling, the overall dislocation density increases significantly, and dislocation clusters with higher density are observed in the laths (Fig. 23a). Extensive dislocation motion and rearrangement can alter the subgrain structure, forming large areas of small-angle grain boundaries,

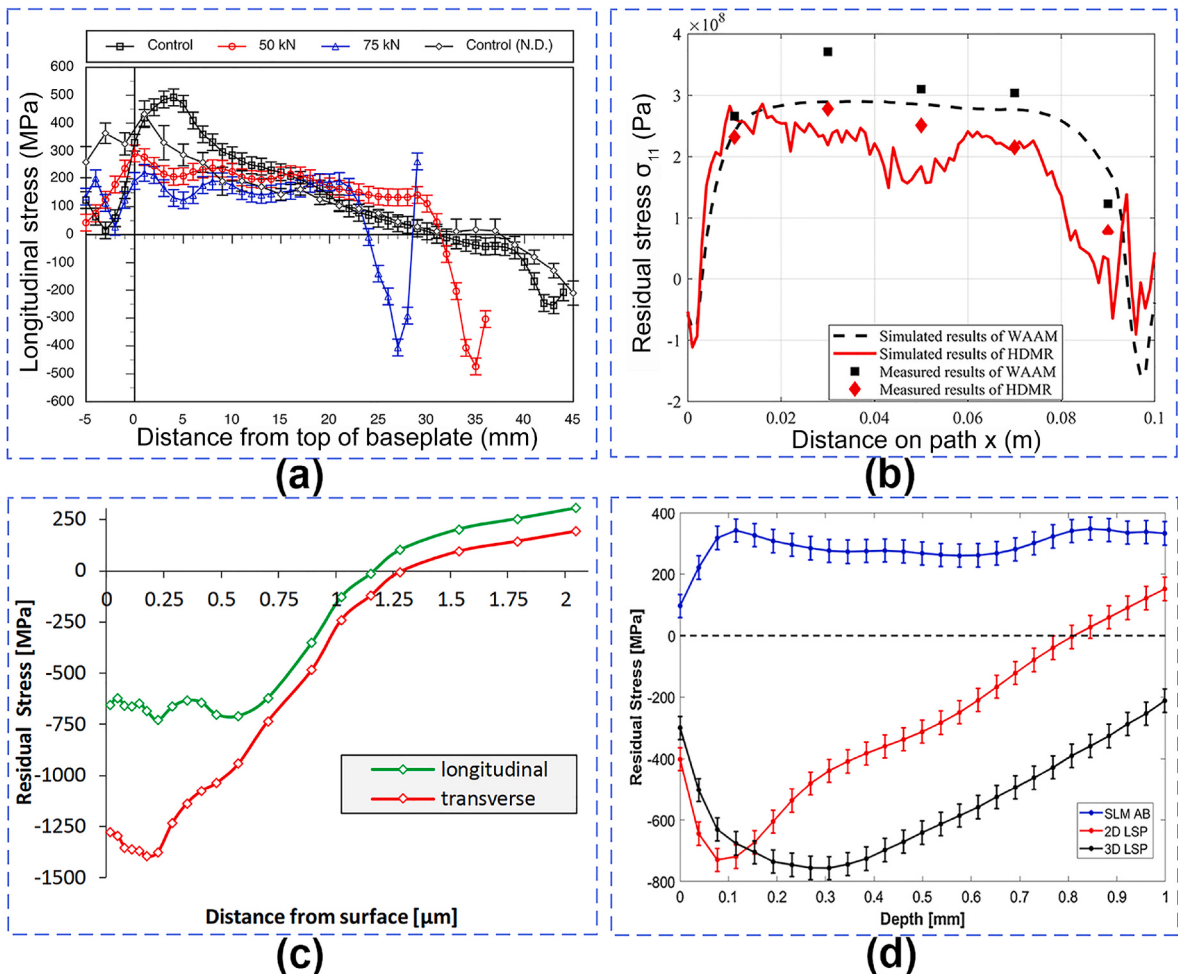


Fig. 22. Effects of auxiliary mechanical deformation on residual stress distributions. (a) Interlayer rolling assisted WAAM Ti6Al4V [144], (b) in-situ rolling assisted WAAM Inconel 718 [145], (c) interlayer MHP assisted WAAM Ti6Al4V [150], and (d) LSP assisted LPBF 316 L [147].

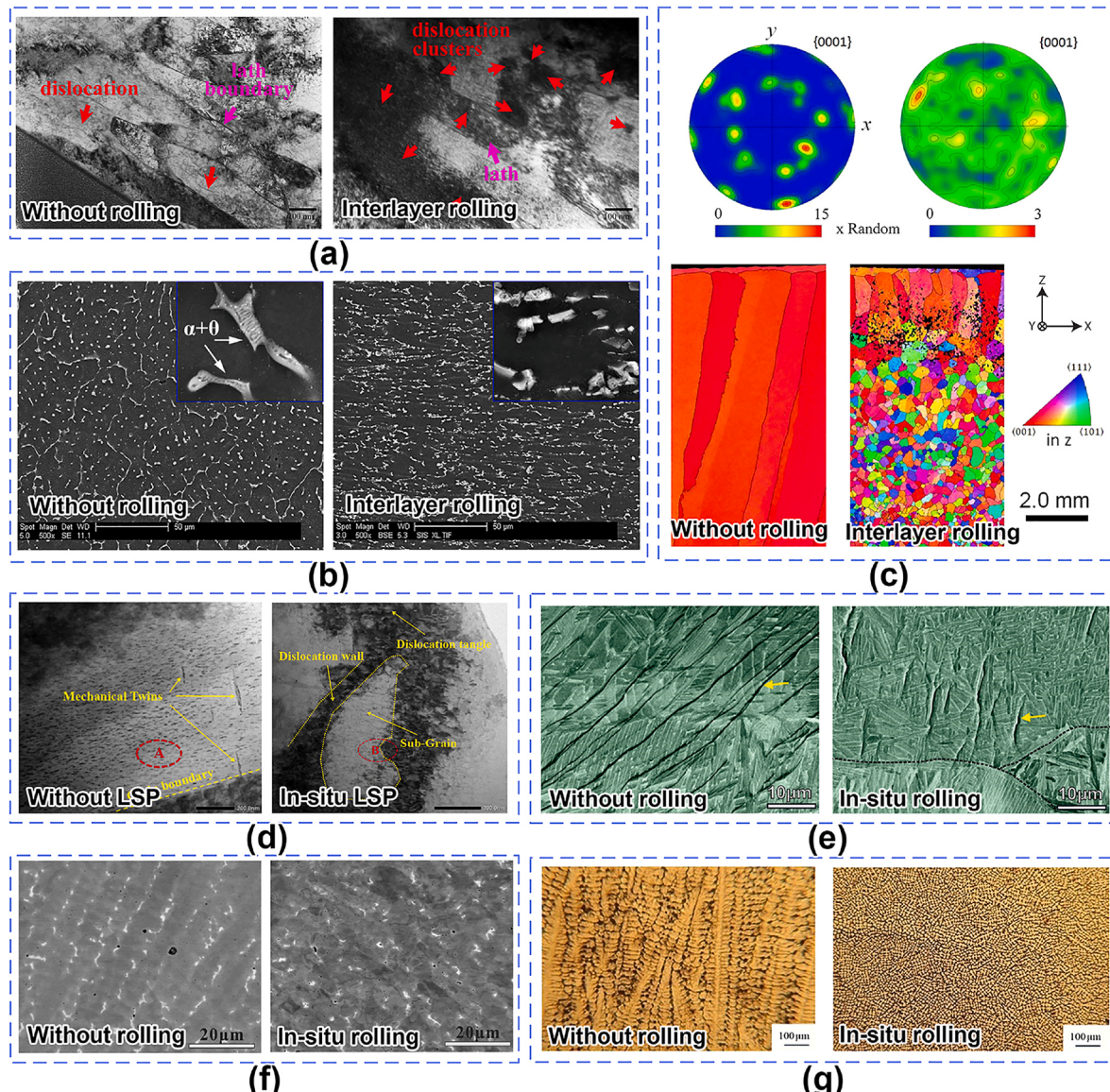


Fig. 23. Microstructure evolutions of AM fabricated alloys with various auxiliary mechanical deformations. (a) WAAM 18Ni250 steel with/without interlayer rolling [151], (b) WAAM 2319 Al alloy with/without interlayer rolling [152], (c) WAAM Ti6Al4V with/without interlayer rolling [153], (d) WAAM 2319 Al with and without in-situ LSP [155], (e) LDED Ti6Al4V with/without in-situ rolling [133], (f) LDED Inconel 718 with/without in-situ rolling [156], and (g) WAAM C45 steel with/without in-situ rolling [134].

improving the morphology of the microstructure, and significantly refining the grain size. For instance, Gu et al. [152] studied the influence of rolling force on the microstructure of a 2319 Al alloy using interlayer rolling assisted WAAM. The eutectic particles were fractured into smaller pieces and were extended along the deformation direction, as shown in Fig. 23b. In the Ti6Al4V samples deposited by interlayer rolling assisted WAAM, the $\langle 001 \rangle // BD$ crystallographic texture in WAAM Ti6Al4V is generally strong, and this texture can be significantly reduced through auxiliary deformation, the coarse β grains in the centimetre-scale can be refined to less than 100 μm , as shown in Fig. 23c [153].

In-situ rolling in AM is analogous to hot working, dislocations are controlled by a combination of work hardening, recovery and recrystallization softening. In the in-situ rolling assisted WAAM Ti6Al4V, higher local misorientations and geometrically dislocation densities due to the plastic deformation and dynamic recrystallization [154]. Similar results have also been reported in Al alloys, Sun et al. [155] studied the microstructural evolution of in-situ LSP-assisted WAAM 2319 Al alloy.

Before LSP, a small number of mechanical twins was randomly distributed within the original grains. After LSP, dislocation walls and dislocation tangles were distinctly observed. (Fig. 23d). By controlling the appropriate amount of deformation and deformation temperature, releasing the deformation energy through the dynamic recovery and recrystallization process, and driving grain nucleation, the texture tendency of the original deposited sample can be significantly weakened, and more minute grains can be obtained. In in-situ rolling-assisted LDED of Ti6Al4V [133], numerous long and continuous slip bands existed in the unrolled sample, which became shorter and more tortuous after rolling (Fig. 23e), and the average grain sizes reduced by 75%. Li et al. [156] studied in-situ rolling assisted LDED Inconel 718 and reported that the Laves phase in the rolled sample was more uniformly dispersed than in the as-built samples (Fig. 23f). For a C45 steel deposited by in-situ rolling assisted WAAM, the grain morphology was significantly changed from columnar to equiaxed, as illustrated in Fig. 23g [134].

5.5. Effect of mechanical deformation field on mechanical properties

5.5.1. Strength and ductility

The mechanical properties of the AM-built parts with and without auxiliary mechanical deformation are summarized in Table 6. Overall, the comprehensive mechanical properties (hardness, YS, UTS, and δ) of AM fabricated parts can be enhanced efficiently with auxiliary mechanical deformation. The underlying mechanisms for mechanical property improvement will be reviewed.

First, the improved mechanical properties could be associated with the reduction of material porosity [140,141,152]. As described in Section 5.2, the auxiliary mechanical deformation closes or reduces the size of the internal pores, especially for Al alloys. For the interlayer rolling assisted WAAM, the elongation of the rolled 2319 and 5087 Al alloys was increased by 23% and 19%, respectively.

Second, auxiliary mechanical deformation can refine grains, and fine equiaxed grains have higher strength and plasticity. Martin et al. [131] performed high-pressure interlayer rolling on WAAM Ti6Al4V. The columnar prior β grains were transformed into equiaxed fine grains, and

α -lath width was decreased. The UTS and δ reached 1078 MPa and 12.9%, respectively, which increased by 17.3% and 5.7%, respectively, compared with the counterpart without rolling. For in-situ rolling-assisted WAAM, Cheng et al. [157] investigated the microstructure and tensile properties of Ti6Al4V. With the increase of rolling force, UTS and YS increase, and the elongation anisotropy decreases due to significant grain refinement. Similarly, in the MHP-assisted WAAM-processed 2319 Al alloy, the YS increased by 62.8% due to grain refinement [143].

Third, auxiliary mechanical deformation could alleviate the anisotropic mechanical properties caused by strong crystallographic textures in the AM. Zhang et al. [158] tested the mechanical properties of Inconel 718 with cold rolling and warm rolling. As-built and cold-rolled samples showed significant anisotropic mechanical properties, but warm-rolled heat-treated samples obtained isotropic tensile properties. As Tian et al. [133] reported, the mechanical properties of the specimens after in-situ rolling are improved, and the anisotropy is reduced. This was mainly attributed to the nearly equiaxed grains, the more randomly oriented internal laths of the rolled samples, and the weaker orientation

Table 6
Mechanical properties of AM fabricated parts with auxiliary mechanical deformation.

AM	Mechanical deformation	Material	Force	Deformation	Mechanical property	Property without deformation	Property with deformation	Property improvement	Ref.
WAAM	Interlayer rolling	Ti6Al4V	75 kN	17.7%	UTS	919 MPa	1078 MPa	17.3%	[131]
					YS	870 MPa	1028 MPa	18.2%	
					δ	12.2%	12.9%	5.7%	
WAAM	Interlayer rolling	2319 Al alloy	45 kN	44.2%	Hardness	68.3 HV	102.3 HV	49.8%	[152]
					UTS	262 MPa	314 MPa	19.8%	
					YS	134 MPa	244 MPa	82.1%	
					δ	18.4%	8.5%	-53.8%	
WAAM	Interlayer rolling (cold)	Inconel 718	50 kN	8.5%	Hardness	250.6 HV	322.9 HV	28.9%	[158]
					UTS	841 MPa	972 MPa	15.6%	
					YS	473 MPa	724 MPa	53.1%	
					δ	26.3%	24.2%	-8.0%	
WAAM	Interlayer rolling (warm)	Inconel 718	50 kN	17.0%	Hardness	250.6 HV	308.4 HV	23.1%	[158]
					UTS	841 MPa	940 MPa	11.8%	
					YS	473 MPa	666 MPa	40.8%	
					δ	26.3%	30.2%	14.8%	
WAAM	Interlayer rolling	18Ni250	75 kN	-	UTS	1410 MPa	1751 MPa	24.2%	[151]
					YS	1303 MPa	1634 MPa	25.4%	
					δ	8.5%	6.1%	-28.2%	
					UTS	688 MPa	973 MPa	41.4%	
WAAM	In-situ rolling	C45	3 kN	-	YS	382 MPa	644 MPa	68.6%	[134]
					δ	13.0%	18.0%	38.5%	
					UTS	976 MPa	1059 MPa	8.5%	
					YS	820 MPa	966 MPa	17.8%	
WAAM	In-situ rolling	Ti6Al4V	5 kN	-	δ	11.4%	15.7%	37.7%	[162]
					UTS	508 MPa	593 MPa	16.7%	
					YS	433 MPa	479 MPa	10.6%	
					δ	7.8%	13.3%	70.5%	
WAAM	In-situ rolling	Inconel 718	-	30.0%	UTS	480 MPa	552 MPa	15.0%	[180]
					YS	356 MPa	390 MPa	9.6%	
					δ	37.6%	39.2%	4.3%	
					UTS	924 MPa	993 MPa	7.5%	
WAAM	In-situ rolling (vibration shock)	70s-6 N	136	26.5%	YS	148 MPa	241 MPa	62.8%	[181]
					δ	18%	13%	-27.8%	
					UTS	855 MPa	907 MPa	6.1%	
					YS	574 MPa	622 MPa	8.4%	
WAAM	MHP	2319 Al alloy	-	50.8%	δ	11.7%	11.3%	3.4%	[143]
					UTS	289 MPa	335 MPa	16.0%	
					YS	148 MPa	241 MPa	62.8%	
					δ	18%	13%	-27.8%	
WAAM	MHP	Ti6Al4V	-	-	UTS	924 MPa	993 MPa	7.5%	[135]
					YS	855 MPa	907 MPa	6.1%	
					δ	11.7%	11.3%	3.4%	
					UTS	574 MPa	622 MPa	8.4%	
WAAM	MHP	316 L	55 N	24.8%	YS	360 MPa	450 MPa	25.0%	[139]
					δ	32.5%	27.9%	14.2%	
					UTS	198 HV	206 HV	4.1%	
					YS	350 HV	355 HV	1.4%	
WAAM	MHP	70S-6 410 NiMo NiCu7 CuAl-A2	-	15.4% 28.0% 25.5% 12.4%	Hardness	131 HV	143 HV	9.2%	[182]
					UTS	145 HV	155 HV	6.9%	
					YS	324 HV	420 HV	29.6%	
					δ	1004 MPa	1287 MPa	28.2%	
LPBF	LSP	Ti6Al4V	-	-	UTS	997 MPa	1197 MPa	20.1%	[183]
					YS	250 MPa	360 MPa	108%	
LPBF	LSP	316 L	-	-	Fatigue limit	440 $\mu\text{m/s}$	110 $\mu\text{m/s}$	-75%	[22]
					Crack propagation rate				

texture.

Last, mechanical deformation results in work hardening through an increase in dislocation density. In interlayer rolling assisted WAAM 18Ni250 steel, the dislocation density increases after rolling. The UTS is improved from 1410 to 1750 MPa [151]. In MHP-assisted WAAM 2319 Al alloy, compared with the as-built samples, the YS of hammered samples increased by 60.6% [143]. The primary strengthening mechanism is due to the high dislocation density caused by the plastic deformation imparted through the hammering process.

The effect of auxiliary mechanical deformation on the mechanical properties of Ti6Al4V processed by AM is summarized in Fig. 24, which includes various kinds of AM technologies (i.e., LPBF, LDED and WAAM). The mechanical properties of Ti6Al4V cold worked plate standard (AMS B265) are also included for comparison. Overall, the strength and ductility of mechanical deformation-assisted AM are improved compared with conventional AM, and most of the data exceeds the properties obtained for wrought Ti6Al4V.

5.5.2. Fatigue performance

The poor fatigue performance of AM-processed parts is a common phenomenon, mainly due to metallurgical defects, high tensile residual stresses, and heterogeneous microstructure in AM-processed parts [178, 179]. Xie et al. [142] investigated the fatigue resistance of an in-situ rolling-assisted WAAM 5087 Al alloy and reported that the size and morphology of defects play a crucial role in affecting crack initiation life. Fig. 25a shows the probabilistic stress-life (S-N) fatigue curve of the rolled 5087 Al alloy resulted in a fatigue limit of 84 MPa at a survival rate of 95%. Mechanical deformation has also been used to enhance the fatigue performance of Ti alloys. The fatigue properties of interlayer rolling assisted WAAM Ti6Al4V are almost twice those required by the Airbus standards for forged and cast counterparts [129], as shown in Fig. 25b. In addition, Hu et al. [154] studied the fatigue crack growth (FCG) rates of WAAM Ti6Al4V with auxiliary in-situ rolling. In the area of stable crack propagation region, there is little difference in FCG rates between WAAM and in-situ rolling assisted WAAM (Fig. 25c). Besides, the residual compressive stress resulting from mechanical deformation also contributes to improved fatigue properties. For instance, in LSP-assisted LPBF 316 L, the fatigue life was more than 14 times higher than that of LPBF 316 L (Fig. 25d) [22].

6. Other emerging energy-fields assisted metal additive manufacturing

Some emerging fields have also been reported which have the potential to assist the metal AM process. This section will introduce several emerging energy fields deployed in FAAM, including electric field, plasma field, and coupled multi-fields. Although there is a lack of relevant research on these emerging fields assisted AM, there is great

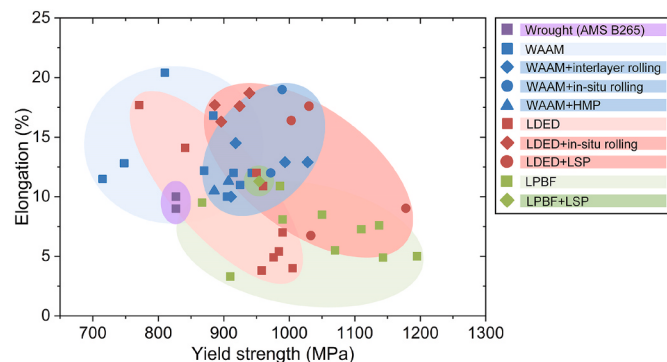


Fig. 24. Mechanical properties of the Ti6Al4V deposited by various AM technologies with and without auxiliary mechanical deformation [131,133, 135,159–177].

potential in achieving high performance in AM-built components.

6.1. Electric field assisted additive manufacturing (E-FAAM)

The application of an electric field (EF) is an established technique in other sectors such as energy, medical and manufacturing [184–186]. In terms of metal AM, the electric field shows great potential in tailoring the microstructure and mechanical properties of AM-built components. Generally, the effects of the electric field on microstructure evolutions of AM-built parts are similar to the application of a magnetic field [14]. The induced electrostatic force by an exerted electric field can drive feeding materials into the melt pool, thereby increasing the deposition rate. In addition, the auxiliary electric field can affect the heat input, enlarge the melt pool and reduce the cooling rate [187].

Notably, an electric field has been incorporated into LDED of 316 L steel [187], as displayed in Fig. 26a–c. It is reported that the cooling rate of the melt pool was reduced slightly under the static or rotating electric field deployment, and the solidification mode changed from ferritic-austenitic mode ($L \rightarrow L + \delta \rightarrow L + \delta + \gamma \rightarrow \delta + \gamma \rightarrow \gamma$) to austenitic-ferritic mode ($L \rightarrow L + \gamma \rightarrow L + \delta + \gamma \rightarrow \gamma + \delta \rightarrow \gamma$) with the application of electric field (Fig. 26d–f). In addition, the residual tensile stress on the surface of the LDED-built parts was reduced and even transformed into compressive stress with the effect of the applied electric field. An electric field has also been incorporated into the AM of an In–Bi–Sn low melting point alloy, and the process stability was improved [188]. Despite the beneficial effects of the electric field on metal AM, it is noteworthy that the research on E-FAAM (especially for LPBF and LDED techniques) is still in its infancy. More research is needed to reveal the effects and mechanisms of electric fields on metal AM with a focus on densification, solidification behaviour/mode, melt pool, thermal history and mechanical properties.

6.2. Plasma field assisted additive manufacturing (P-FAAM)

The plasma field is also an emerging auxiliary energy field for metal AM. Herein, the P-FAAM refers to the AM with plasma formation induced by another auxiliary beam. For creating a useful plasma, the power density of the auxiliary beam should be higher than the dielectric breakdown threshold of metals. For instance, Yoon et al. [189] reported a novel pulsed laser assisted LDED technique for Ti6Al4V fabrication, as shown in Fig. 27a. During the LDED process, the pulsed laser induced the plasma field formation above the melt pool (Fig. 27a), shock wave propagation and cavitation. Hence, the pulse laser not only alters the thermal field but also affects Marangoni flow by the induced shock wave. Thanks to the laser-induced cavitation and generated shock waves induced by the plasma field, the prior β grains of the LDED-built Ti6Al4V were refined by the assisted pulsed laser significantly (Fig. 27b). Meanwhile, the maximum multiple of uniform distribution of the prior- β grains reduced from 16 to 7.7 with the assisted pulse laser (Fig. 27c). These phenomena indicate that assisted pulsed laser is a feasible way for fabricating high-quality Ti6Al4V parts as the weakened texture and refined grains are beneficial for achieving high and isotropic mechanical properties.

6.3. Multi-fields coupling assisted additive manufacturing

Multi-field coupling is also a feasible solution to control the solidified microstructures. Several works have been done to study the effects of multi-field coupling on metal AM, including electric field coupled with magnetic field [187] and thermal field coupled with magnetic field [190].

Lu et al. [187] reported that applying a rotating electric field coupled with a magnetic field could expand the melt pool to approximately three times the original size due to electric and magnetic fields on the plasma plume. Compared to an electric field or magnetic field exerted alone, the coupled fields can achieve a higher hardness of the AM-deposited alloy

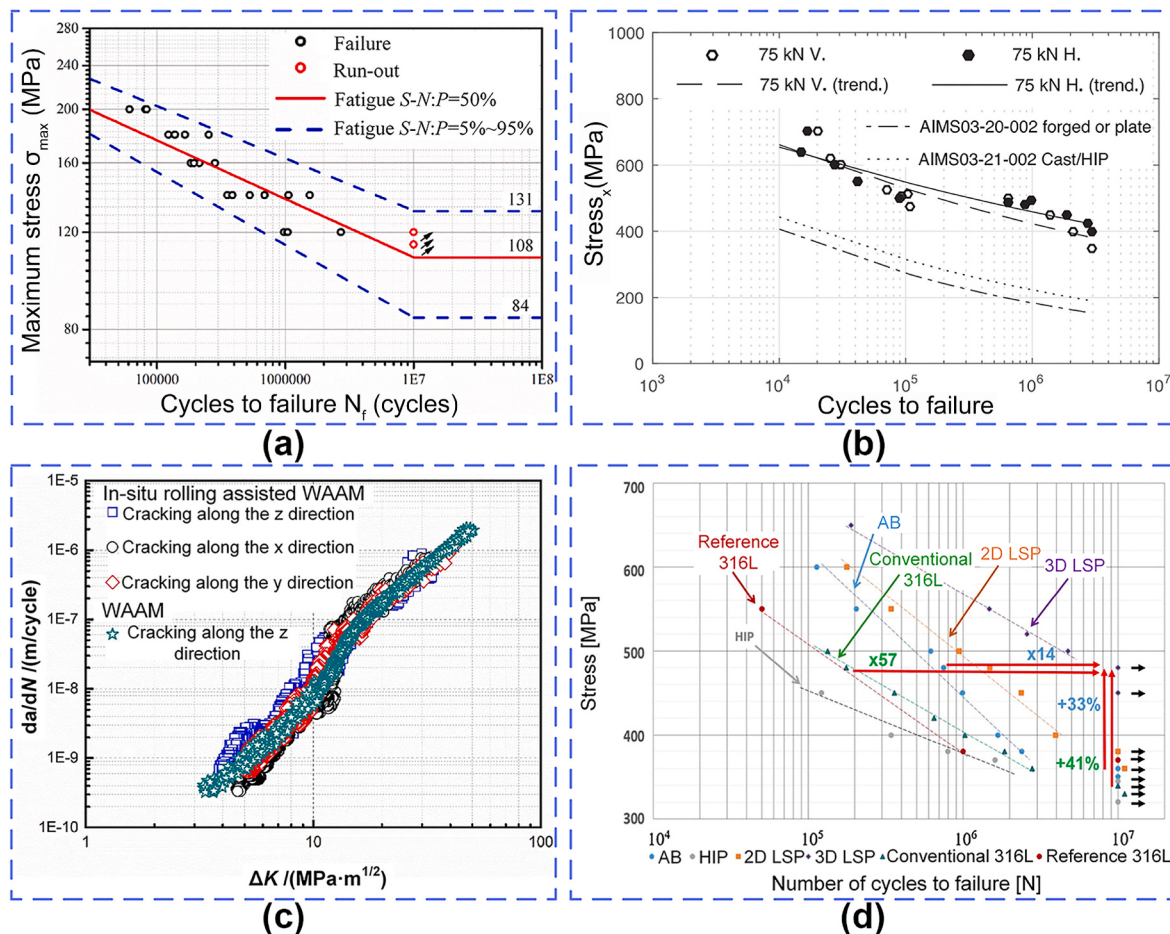


Fig. 25. Fatigue property of various AM fabricated alloys with auxiliary mechanical deformation. (a) S-N fatigue curves of 5087 Al alloy deposited by in-situ rolling assisted WAAM [142], (b) S-N fatigue curves of Ti6Al4V alloy deposited by interlayer rolling assisted WAAM [129], (c) fatigue crack growth (FCG) rates of WAAM Ti6Al4V with and without in-situ rolling [154], (d) S-N fatigue curves of 316 L deposited by LSP assisted LPBF [22].

while also restraining the surface tensile residual stresses of AM-built parts and promoting their transformation to compressive stress [187]. Ma et al. [190] studied synchronous electromagnetic induction-assisted LDED of Ti6Al4V/10 wt% TiC_p composite (Fig. 28a) and proposed that the coupled thermal and magnetic fields improved the microstructure and mechanical properties of the composite. The underlying mechanisms proposed are: (i) the Joule heating effect heated the vicinity region of the melt pool, which reduced the temperature gradient, increased the growth rate and promoted the nucleation of granular TiC. (ii) The oscillating and shear force generated by the Lorentz force then broke these TiC particles, which thereby refined these particles. As a result, the tensile strength and ductility of the Ti6Al4V/10 wt% TiC_p composite were both enhanced simultaneously by the synchronous electromagnetic induction (Fig. 28b). In addition, Gong et al. [21] reported a novel oscillating laser-assisted WAAM process, as shown in Fig. 28c and d. Compared with linear beam scanning assisted AM, the auxiliary laser beam that moves in an oscillating path can provide a robust stirring effect to the melt pool, thereby altering melt pool flow and temperature gradient greatly during solidification, as shown in Fig. 28e and f. As a result, the unfavourable {001}<100> texture and anisotropic tensile properties were both weakened by the application of an auxiliary oscillating laser. Meanwhile, the auxiliary oscillating laser beam captured the bubbles in the melt pool, thereby eliminating the pores efficiently.

In summary, coupling of multi-fields to assist AM can bring higher flexibility to the process and contributes to modifying and improving the microstructure and properties. However, up until the date of publication

of this work, research in this area is still limited. To achieve more desirable outcomes, the coupling effects between different fields and their interactive mechanisms with the material being deposited still needs investigation.

7. Simulation in field-assisted additive manufacturing

The application of auxiliary fields (magnetic, acoustic, thermal, and mechanical deformation fields, and other emerging fields) leads to improvements in the properties of AM-processed parts. However, it is still challenging to understand the influence of the auxiliary fields on heat transfer, fluid flow, microstructural evolution, residual stress, and distortion in the produced parts. The experimental trials and errors required to develop a sound understanding are expensive and time-consuming due to the multiple process parameters and various alloy properties and combinations available. FAAM process simulation and modelling are the pathways to understanding the complex heat transfer and fluid flow within the melt pool and the surrounding areas [191–193]. Several commercial software, such as ABAQUS, ANSYS, COMSOL, and FLOW-3D, is available for the FAAM simulation. Both the analytical model and mechanistic models, along with the commonly used finite element method (FEM), finite volume method (FVM), and finite difference method (FDM) are used to explore the heat transfer and fluid flow for the FAAM processes [192,193].

In this section, fundamentals of AM simulation (including heat transfer, fluid flow, and alloy properties in Table 7) are introduced in Section 7.1. FAAM simulations with the application of magnetic field

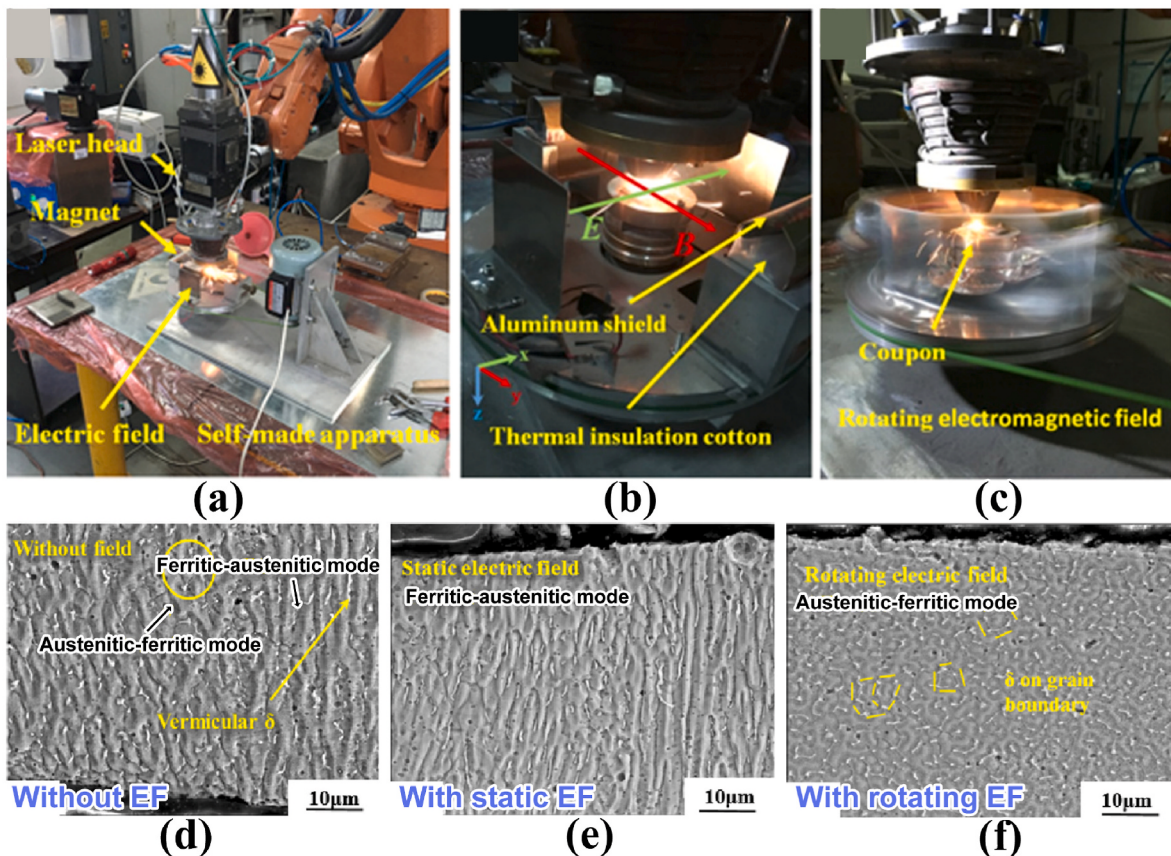


Fig. 26. Electric field assisted additive manufacturing (E-FAAM). (a)–(c) Experimental apparatus of electric and magnetic fields assisted AM [187]; (d)–(f) microstructures of the LDED-built part without electric field, with a static electric field, and with rotating electric field, respectively [187].

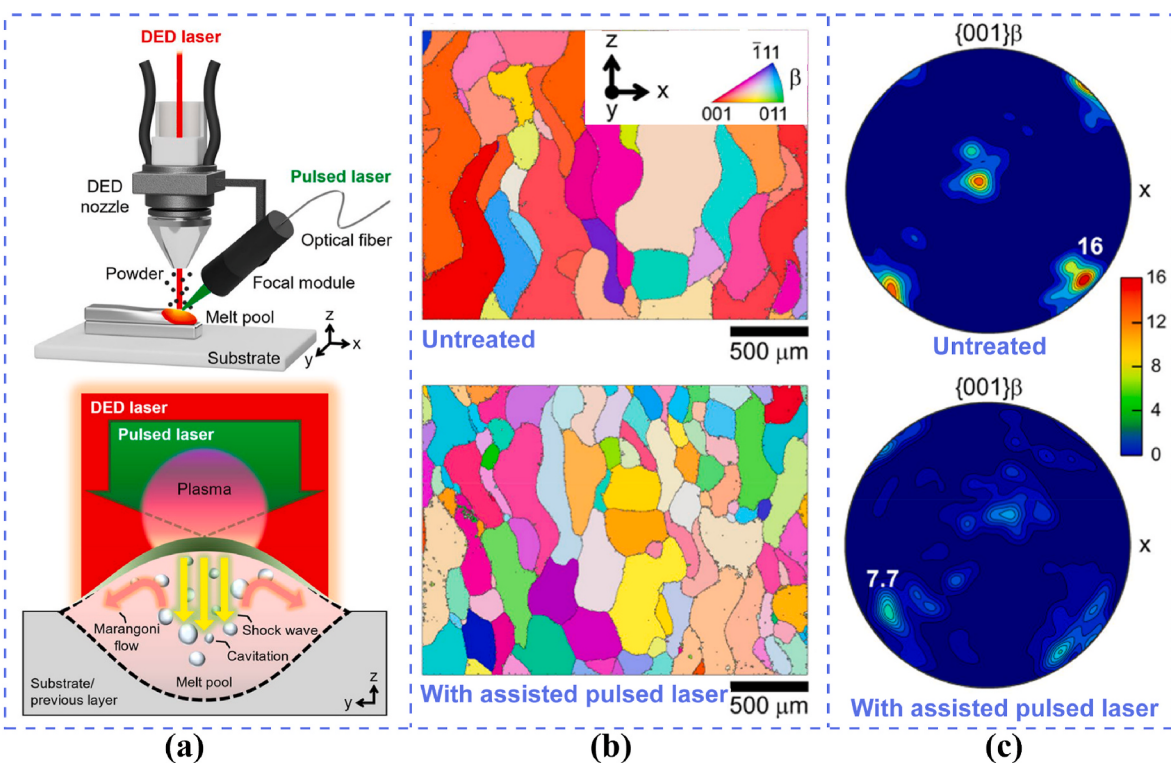


Fig. 27. Plasma field assisted additive manufacturing (P-FAAM) of metallic materials. (a) Schematic of pulsed laser-assisted AM [189], EBSD (b) IPF maps and (c) {001} PF maps of the reconstructed β grains of the pulsed laser assisted LDED-built Ti6Al4V alloy.

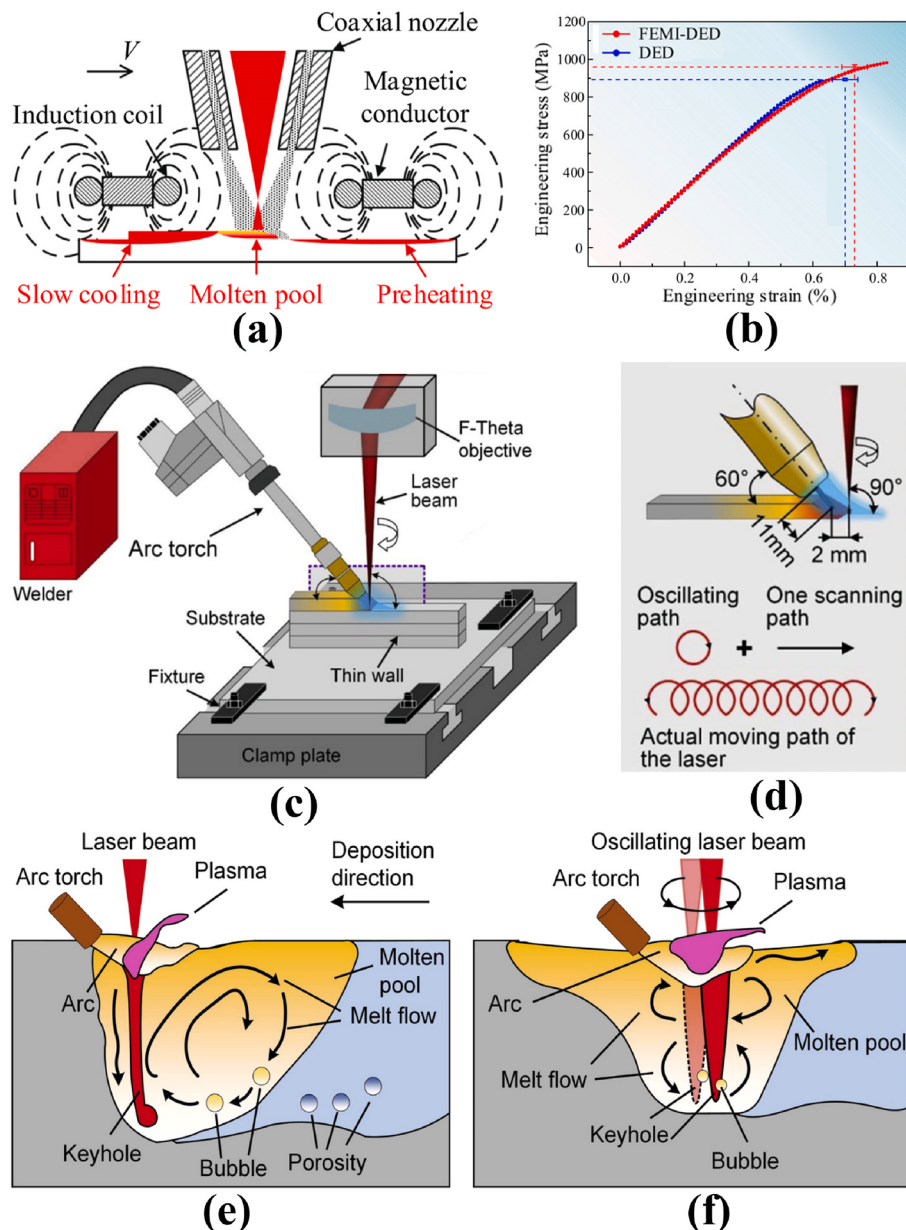


Fig. 28. Multi-fields coupling assisted additive manufacturing of metallic materials. (a) Schematic of synchronous electromagnetic induction assisted LDED [190], (b) tensile curves of Ti6Al4V/10 wt% TiC_p composite with and without synchronous electromagnetic induction; (c) and (d) schematic of synchronous oscillating laser coupled with wire-arc additive manufacturing [21], and melt flow with (e) ordinary laser and (f) oscillating laser [21].

(MF), acoustic field (AF), thermal field (TF), and mechanical deformation field (DF) are explained in Sections 7.2 to 7.5, respectively. The aim of this part is to summarize the current progress of FAAM process simulation (as shown in Table 8), compare modelling approaches between AM and FAAM (as shown in Table 9), and provide valuable insight and available methods for readers to understand FAAM simulation better. Some simulation examples of FAAM with various auxiliary fields are listed in Table 8, including the simulation method, model, software, and output from simulations. In addition, the difference in modelling approaches between AM and FAAM are compared in terms of temperature field, velocity field, microstructure, residual stress, and distortion (in Table 9).

7.1. Fundamentals of simulation in additive manufacturing

7.1.1. Heat transfer and fluid flow

The analytical model based on heat conduction is an effective and

easy way to estimate and calculate the temperature field and the shape of the melt pool. A three-dimensional temperature field can be estimated analytically by solving the Fourier heat conduction equation (Eq. (12)) [193,194]. The Fourier heat conduction equation is given by:

$$k \frac{\partial^2 T}{\partial x^2} + \frac{\partial^2 T}{\partial y^2} + \frac{\partial^2 T}{\partial z^2} + \dot{Q} = \rho C \frac{\partial T}{\partial t} \quad (12)$$

where k , ρ , C , T , and t are the thermal conductivity, density, specific heat, temperature, and time, respectively. \dot{Q} is the rate of heat input per unit volume. The shape and size of the fusion zone are relatively easy to determine by setting the temperature field values as those for the solidus and liquidus temperatures. The estimated pool width and depth using the analytical model have been well-validated by corresponding experimental results [11].

It is significant to note that the analytical model based on heat conduction has several drawbacks. It ignores the influence of surface-

Table 7

Thermophysical properties of six commonly used alloys. 'T' represents the temperature in K, which varies between room temperature to solidus temperature [193,202]. Density and diffusivity values are given at room temperature. Viscosity, surface tension, and surface tension gradient ($d\gamma/dT$) are provided at the liquidus temperature of alloys.

Properties	SS316	Ti-6Al-4V	IN718	Co-Cr	A357	AlSi10Mg
Liquidus temperature (K)	1733	1928	1609	1703	883	867
Solidus temperature (K)	1693	1878	1533	1603	855	831
Thermal conductivity (W/m K)	11.82+ 0.0106T	1.57+1.6× $10^{-2}T-1\times$ $10^{-6}T^2$	0.56+2.9× $10^{-2}T-7\times$ $10^{-6}T^2$	25.9	25.2+0.4T+ $7.4\times 10^{-6}T^2$	113+1.06× $10^{-5}T$
Specific heat (J/kg K)	$3T-4.015\times$ $10^{-4}T^2+9.46$	$492.4+0.025T$	$360.4+0.026$	1040	$928.6-0.6T$ $+1.5\times 10^{-3}T^2$	536.2+ 0.035T
Density (kg/m ³)	7800	4430	8100	8280	2700	2670
Viscosity (kg/m s)	7×10^{-3}	4×10^{-3}	5×10^{-3}	5×10^{-3}	1.3×10^{-3}	1.3×10^{-3}
Surface tension (N/m)	1.50	1.52	1.82	1.85	0.92	0.82
Thermal diffusivity of alloy (m ² /s)	4.12×10^{-6}	3.14×10^{-6}	2.90×10^{-6}	3.77×10^{-6}	6.08×10^{-5}	7.74×10^{-5}
Latent heat of fusion of alloy (J/kg)	2.72×10^5	2.84×10^5	2.09×10^5	3.14×10^5	5×10^5	4.23×10^5
$d\gamma/dT$ (N/m K)	-0.40×10^{-3}	-0.26×10^{-3}	-0.37×10^{-3}	-0.37×10^{-3}	-0.35×10^{-3}	-0.35×10^{-3}

active elements (such as S, Se, Te, B, and O) on affecting the temperature of the melt pool. In addition, heat transfer through the fluid flow is not included in the analytical model based on heat conduction. Therefore, the calculated peak temperature using the heat conduction analytical model is higher than the corresponding experimental results. The heat conduction model may predict cooling rates up to 18 times faster than those experimentally measured [193].

A dimensionless number (Peclet number, P_e) indicates the relative importance of convection and conduction in heat transfer within the melt pool Eq. (13) [195,196].

$$P_e = \frac{UL}{\alpha} \quad (13)$$

where U is the characteristic velocity (such as the maximum velocity), L is the characteristic length (such as the pool length), and α is the thermal diffusivity of the alloy. The heat conduction analytical model is valid for cases when heat conduction is the primary heat transmission (i.e., Peclet number is less than one). However, for most of the AM processes, the Peclet number is much greater than one [193], which suggests that the convective heat transfer is the primary mechanism for the heat transfer within the melt pool.

To avoid the limitation of the heat conduction analytical model and calculate the fluid flow and heat convection within the melt pool, a rigorous mechanistic model is necessary. It is well-known that fluid flow is driven by several important forces, such as the Marangoni force,

electromagnetic force, and buoyance force. The dominant driving forces may vary depending on the AM processes. More details about the driving forces are given below [195–197].

(i) Marangoni force

The Marangoni force is typically regarded as the most significant driving factor for convective fluid movement [193,196]. The surface tension (N/m) on the melt pool top surface, which depends on the temperature and liquid contaminants, can drive the liquid metal flow from low surface tension regions to a region with higher surface tension and affect the melt pool geometry. This spatial gradient of surface tension is called Marangoni stress (N/m²). For a certain pool surface area, the integral of the surface tension gradient (N/m²) over the pool top surface area is called the Marangoni force (N). The Marangoni force can be calculated using Eqs. (14) and (15).

$$F_M = \tau \times S_t \quad (14)$$

$$\tau = \frac{d\gamma}{dT} \bullet \frac{dT}{ds} = \mu \frac{\partial u_s}{\partial n} \quad (15)$$

where F_M is the Marangoni force, τ is the surface tension gradient, S_t is the area of the melt pool top surface (m²), $\frac{d\gamma}{dT}$ is the temperature coefficient of surface tension (γ), $\frac{dT}{ds}$ is the temperature gradient along a surface tangential direction \vec{s} , μ is the velocity, u_s is the surface velocity

Table 8

Some examples of FAAM process simulation with the magnetic field (MF), acoustic field (AF), thermal field (TF), and mechanical deformation field (DF). Simulation methods include the finite element method (FEM), finite volume method (FVM), finite difference method (FDM), a coupled volume-of-fluid and level set (VOSET), Arbitrary Lagrangian-Eulerian (ALE), and volume of fluid (VOF).

Auxiliary fields	AM process	Model	Simulation method	Software/tool	Output from simulation	Refs
MF	LPBF	Part scale heat transfer and fluid flow model	FEM	COMSOL Multiphysics	Temperature field, velocity fields, surface deformation	[198]
		Part scale heat transfer and fluid flow model	FVM	In-house code	Lorentz force, keyhole formation, temperature field, velocity field	[199]
		Part scale heat transfer and fluid flow model	FVM, VOSET	In-house code	Magnetic force, temperature field, velocity field, surface deformation	[235]
		Laser remelting	FEM, ALE	COMSOL Multiphysics	Temperature field, velocity field, and surface undulation	[206]
		Part scale heat transfer and fluid flow model	FVM	FLOW-3D	Temperature field, velocity field, and porosity	[44]
	LDED	Part scale heat transfer and fluid flow model	continuum surface force (CSF) method	FLUENT	Temperature field, velocity field, current density, Lorentz force density	[207]
		Part scale heat transfer and fluid flow model	FDM	In-house code	Temperature field, velocity field, and microstructure	[208]
		Part scale model	FEM	COMSOL Multiphysics	Amplitude field and sound pressure	[74]
		WAAM	VOF	FLOW-3D	Temperature field, velocity field, and pressure field	[78]
		Part scale heat transfer and fluid flow model	VOF	FLOW-3D	Temperature field, velocity field, and flow streamlines	[81]
AF	Melting and solidification Casting	Part scale model	FEM	ANSYS	Pressure distribution, acoustic intensity, temperature field, and liquid fraction	[209]
		Part scale heat transfer and fluid flow model	FEM	ProCAST	Temperature field and velocity field	[210]
TF	Hybrid plasma arc-laser AM	Part scale heat transfer model	FEM	ABAQUS	Temperature field	[236]
		Part scale heat transfer model	FEM	COMSOL Multiphysics	Temperature field	[103]
	LDED	Part scale heat transfer model	FEM	ABAQUS	Temperature, strain, and stress fields	[106]
		Part scale heat transfer model	FEM	MSC Marc	Temperature field	[218]
	WAAM	Part scale heat transfer model	Mathematical analysis	In-house code	Temperature field	[98]
		Part scale heat transfer model	FEM	In-house code	Temperature field	[117]
	LPBF	Part scale heat transfer model	FEM	ABAQUS	Temperature field and stress fields	[211,212]
		Part scale heat transfer model	FEM	COMSOL Multiphysics	Stress fields	[101]
	LDED	Part scale heat transfer model	FEM	In-house code	Temperature and stress fields	[119]
		Part scale heat transfer model	FEM	ABAQUS	Temperature field and residual stress	[148]
DF	LSP + LDED	Part scale heat transfer model	FEM	ABAQUS	Temperature field, equivalent plastic strain, and residual stress	[144,145,222,223,230]
		Part scale heat transfer model	FEM	ABAQUS	Temperature field and residual stress	[219]
	WAAM	Part scale heat transfer model	FEM	ABAQUS	Temperature field, and microstructure with grain size and distribution	[220]

along \vec{s} , and \vec{n} is the surface's normal direction.

(ii) Lorentz or electromagnetic force

Another body force that should be included in the momentum conservation equation is the Lorentz force (or electromagnetic force) that arises when an electric current is used, such as in the cases of electron beam directed energy deposition (EB-DED), electron beam powder bed fusion (EB-PBF), and WAAM. The force is calculated as:

$$F_E = \vec{J} \times \vec{B} \quad (16)$$

where F_E is the electromagnetic force (in N), \vec{J} is the current density vector and \vec{B} is the magnetic flux vector in the melt pool. More information about the Lorentz force is available in Section 2.

(iii) Buoyancy force

For a liquid with different temperatures, the hot liquid with low density will tend to rise while the cold liquid with high density will tend to sink, which leads to the convective flow inside the melt pool. The Buoyancy force can be calculated as:

$$F_B = \rho g \beta V (T - T_{ref}) \quad (17)$$

where F_B is the buoyancy force (in N), ρ is the density of liquid metal (kg/m^3), g is the acceleration due to gravity (m/s^2), β is the thermal expansion coefficient ($1/\text{K}$), V is the volume (m^3), T is the temperature of liquid metal (K), and T_{ref} is an arbitrarily selected reference temperature (K).

(iv) Governing equations

Table 9

Comparison of modelling approaches between AM and FAAM with the magnetic field (MF), acoustic field (AF), thermal field (TF), and mechanical deformation field (DF).

Method	Temperature field	Velocity field	Microstructure	Residual stress and distortion
AM	Solutions of (1) Heat conduction equation, and (2) Conservation equations of mass, momentum, and energy [192,193,237–239].	Solution of conservation equations of mass and momentum [192,193,237–239].	Calculations of temperature field, temperature gradient (G) and solidification rate (R) and G/R ratio at the solid/liquid interface [200,201,240].	Calculations of temperature field, strains (elastic, plastic, thermal, phase transformation and creep), constrain movements of some nodes, and apply constant or varying loads as boundary conditions [192,193,241–243].
AM + MF	Same as AM, the magnetic field has less effect on the temperature field within the melt pool [44, 198,199,206].	Add magnetic field-induced Lorentz force into the source term (S_{uj}) in the momentum conservation equation [206–208,235].	Same as AM, the change in pool shape and size due to magnetic field affects the microstructure evolution [208].	Same as AM, local change in pool shape and size due to the magnetic field has an insignificant effect on the overall temperature field, residual stress, and distortion [235].
AM + AF	Same as AM, the acoustic field has less effect on the temperature field within the melt pool [78,81, 209,210].	Add sound pressure and ultrasound-induced inertial force into the momentum conservation equation [78,81, 210].	Same as AM, acoustic field-induced cavitation and streaming can promote grain nucleation and refinement. Modelling of this topic is scarce in the literature [192,193].	Same as AM, the acoustic field has limited influence on residual stress and distortion. Modelling of this topic is scarce in the literature [192,193].
AM + TF	Add external heat sources or adjust boundary conditions for the same approach used for AM [98,218,236].	Similar to AM, the thermal field has limited influence on the velocity field within the melt pool [192,193,244].	Like AM, the change in temperature field, pool shape and size due to thermal field affect the microstructure evolution [192,193].	Same as AM, the change in temperature field, pool shape and size due to thermal field affect the residual stress and distortion [119, 211,212]
AM + DF	Same as AM, the mechanical deformation has very less influence on the temperature field within melt pool [144,145, 148,230]	Same as AM, the mechanical deformation has very less influence on the velocity field within melt pool [192,193]	Varying pressure/load from the mechanical deformation can cause dynamic recrystallization, nucleation, and grain growth, which are similar to those in metal forming [220,224–226]	The varying pressure/load from mechanical deformation is applied as either boundary conditions or body force in stress and strain calculation, which is similar to that in modelling of rolling, peening, and wire drawing [227–229,245,246]

For AM process, the heat transfer and fluid flow for the melt pool and its surroundings are calculated based on the conservation equations of mass, momentum, and energy in a transient form in Cartesian coordinates as [192,193]:

$$\frac{\partial(\rho u_i)}{\partial x_i} = 0 \quad (18)$$

$$\frac{\partial(\rho u_j)}{\partial t} + \frac{\partial(\rho u_i u_j)}{\partial x_i} = \frac{\partial}{\partial x_i} \left(\mu \frac{\partial u_j}{\partial x_i} \right) + S_{uj} - K_p \frac{(1-f_L)^2}{f_L^3 + B_N} u_j \quad (19)$$

$$\rho \frac{\partial h}{\partial t} + \frac{\partial(\rho u_i h)}{\partial x_i} = \frac{\partial}{\partial x_i} \left(C_p \frac{\partial h}{\partial x_i} \right) - \rho \frac{\partial \Delta H}{\partial t} - \rho \frac{\partial(u_i \Delta H)}{\partial x_i} + S_h \quad (20)$$

where ρ is the density, u_i and u_j are the velocity components along the i and j directions, respectively, x_i is the distance along the i direction, t is the time, μ is the viscosity, S_{uj} is the source term for the momentum equation that includes the driving forces for fluid motion, f_L is the liquid fraction ($f_L = 1$ when $T \geq T_{liquidus}$, $f_L = 0$ when $T \leq T_{solidus}$), K_p is a permeability coefficient, and B_N is a small numerical constant to avoid division by zero when $f_L = 0$, h is the sensible heat, C_p is the specific heat, k is the thermal conductivity, ΔH is the latent heat source.

Three traditional numerical methods of FEM, FVM, and FDM are used to solve the governing equations along with appropriate boundary conditions. The formulation of these numerical methods is well explained and documented in the literature and thus not repeated here. Among these three methods, FVM and FEM work with a computational domain comprising unstructured mesh to capture complex geometries. However, FDM is usually used for a structured mesh. An interface tracking method, the volume of fluid (VOF) method, can be applied with FDM to track complex geometries with very fine rectangular mesh. To simulate the free surface of the melt pool, the VOF method is a widely used method, and the conservation equation of fluid fraction is solved by Refs. [192,193]:

$$\frac{\partial f_l^v}{\partial t} + \frac{\partial(u_i f_l^v)}{\partial x_i} = 0 \quad (21)$$

where f_l^v is the fluid volume fraction ($0 \leq f_l^v \leq 1$) and not to be confused

with the liquid fraction f_L . The item f_l^v defines the volume fraction of a cell occupied by fluid (either liquid or solid), for example, $f_l^v = 0$ represents a cell without any fluid, and $f_l^v = 1$ indicates a cell filled with fluid.

For FAAM process simulation, the influence of auxiliary fields (such as magnetic, acoustic, mechanical deformation, and thermal fields) should be combined in governing equations and boundary conditions. For example, in the Navier-Stokes equation for the momentum conservation equation (Eq. (19)), the source term (S_{uj}) combines all driving forces which may be generated by the auxiliary fields. In this case, the Navier-Stokes equation (Eq. (19)) can be written as:

$$\frac{\partial(\rho \vec{U})}{\partial t} + \vec{U} \bullet \nabla (\rho \vec{U}) = -\nabla p + \nabla \bullet (\mu \nabla \vec{U}) + \vec{F}_M + \vec{F}_E + \vec{F}_B + \vec{F}_{ext} \quad (22)$$

where \vec{U} is the fluid flowing speed (m/s), ρ is density (kg/m³), μ is viscosity (kg/m s), p is pressure (N/m²), \vec{F}_M , \vec{F}_E , and \vec{F}_B are the Marangoni force, electromagnetic force, and buoyance force respectively. The \vec{F}_{ext} is the force caused by the auxiliary fields, such as the Lorentz force generated by the MF [198,199].

Both the original fields created by the initial heating source and the assisted fields are crucial for controlling heat transfer and fluid flow in the melt pool. However, the adjustment of the governing equations depends on the auxiliary fields. More details for FAAM simulation with various auxiliary fields are explained in Sections 7.2–7.5. Some examples of FAAM process simulation are summarized in Table 8. The comparison of the modelling approaches between the common AM and FAAM is summarized in Table 9.

It is worthwhile to mention that for both AM and FAAM processes, the microstructure is primarily determined by the temperature field using either the heat conduction analytical model or rigorous mechanical models. The microstructure of various depositing materials is determined by the temperature gradient (G), solidification rate (R), and undercooling rate (ΔT). The ratio G/R determines the mode of solidification (such as planar, cellular, columnar, and equiaxed grains), and the product G × R governs the scale of the solidification microstructure. For

microstructure simulation, the melt pool is usually assumed at a steady state. The grain growth direction is assumed parallel to the maximum heat flow direction which is normal to the solidus/liquidus interface of the melt pool and unmelted material. With the calculated temperature field, the microstructure of the AM and FAAM can be calculated using JMA based method, Monte Carlo method, Cellular automata, or Phase-field model [191,200,201]. In addition, for the mechanical deformation-assisted additive manufacturing (D-FAAM) process, the varying pressure or load caused by the external mechanical deformation can result in dynamic recrystallization, and affect the nucleation, and grain growth, which are like those in the metal forming process. More details about the microstructure evolution and calculation are summarized in Table 9.

7.1.2. Thermophysical properties of alloys

Both the governing equations and material properties affect the heat transfer and fluid flow within the melt pool. Under the same processing conditions, various alloys may produce different temperature and velocity fields [202–205]. For example, under the same process conditions, the melt pool for a stainless steel alloy is much smaller than that of an aluminium alloy [202,204]. In addition, different alloys may have different susceptibilities to defects, which implies that under the same process conditions, some alloys have more sensitivity to some flaws compared to other alloys [202]. Therefore, a good understanding of the influence of alloys' thermophysical properties on the simulation of the FAAM process is required. The thermophysical properties of several typical alloys are listed in Table 7 [202–204].

7.2. Magnetic field-assisted AM simulation

As explained in Section 2, for most of the current research with non-ferromagnetic materials or materials with low magnetic intensity, in which cases the magnetic force and magnetization energy are small and negligible in simulation conditions, the induced Lorentz force by the magnetic field (MF) plays the primary role in the simulation of MF-assisted AM simulation [198]. Since the influence of the induced Lorentz force is on the fluid flow, the heat conduction model, which ignores the fluid flow, is not applicable to this case. The induced Lorentz force is considered and combined in the source term (S_{ij}) in the momentum conservation equation (Eq. (19), the same as \vec{F}_{ext} in Eq. (22)). The updated momentum conservation equation, along with the conservation equations of mass and energy, will be solved for the temperature and velocity fields, microstructure evolution [43,198], surface roughness, residual stress, and deformation calculation which use the same methods as AM does (Table 9).

Lu Wang and Wentao Yan [199] build a thermoelectric magneto-hydrodynamic model to investigate the influence of MF on the temperature field, velocity field, induced magnetic field, and Lorentz force density of the LPBF process with AlSi10Mg alloy. This model is generated based on the mass, energy, and updated momentum conservation equations (Eq. (18), (20), and (22)), and the equation for free surface using the volume-of-fluid (VOF) method (Eq. (21)) to calculate the energy absorption, magnetic field intensity, electric currents, Lorentz force distribution, velocity, temperature, and phase fraction. Some commercial software is developed to simulate the FAAM process effectively and efficiently, such as COMSOL Multiphysics [198,206], FLOW-3D [44], and FLUENT [207]. FLOW-3D allows user-defined solutions to calculate the heat transfer and fluid flow for the FAAM process. The method [199] has been developed as a customized solution and applied using FLOW-3D to calculate the heat transfer and fluid flow for the LPBF process under various MF intensities for AlSi10Mg alloy [44]. The calculated results of the temperature gradient, electric currents, and thermo-electric-magnetic force (TEMF) are shown in Fig. 29a–c. A high-temperature gradient is found at the front melt pool solid/liquid interface according to the scanning direction and near the bottom of the

melt pool (Fig. 29a). The TEMF increases with the increasing of MF intensity (Fig. 29b and c).

Chen et al. [198] applied COMSOL Multiphysics to calculate the induced Lorentz force and investigated the influence of MF intensity and direction on the velocity and Lorentz force. With an increase in MF intensity, the induced Lorentz force increases, and the maximum velocity decreases (Fig. 29d and e). For the MF direction, the calculated results using COMSOL Multiphysics indicate that the MF in the Z direction can affect the fluid flow more effectively compared to the MF in the Y direction (Fig. 29d and e). This is because the MF in the Z direction can induce Lorentz force to reduce the fluid flow along the X and Y directions; the MF in the Y direction can decrease the X and Y directions fluid flow. It is well-known that the velocity magnitude components along the X and Y directions are much larger than that along the Z directions. Therefore, the MF in the Z direction can reduce the fluid flow more significantly than the MF in the Y direction [198]. In addition, a small melt pool size can be formed due to the low velocity within the melt pool. Low Marangoni force [204], low velocity, and high hydrodynamic stability [202] within the small melt pool are good for reducing surface roughness. Smooth surfaces are formed for the LPBF components with MF [198]. Some other findings by COMSOL Multiphysics show that the MF intensity has less influence on the peak temperature within the melt pool [206].

The change in pool shape and size due to the magnetic field affects the microstructure evolution, and the microstructure for the MF-assisted AM process can also be predicted by the calculated temperature field. The method for microstructure simulation for the MF-assisted AM process is the same as that used for the AM process. However, the change in pool shape and size due to the magnetic field affects the microstructure evolution. A numerical model [208] is developed to compute heat transfer, fluid flow, phase transformation, and microstructure evolution using finite difference-based methods (FDM) and cellular automata method (CA). The mesoscopic steady-state solutions for temperature and velocity are used as the inputs for the microstructure model. This model has been validated by corresponding experimental results of Al10Si powders. The calculated Lorentz force and hydrodynamic mechanism, thermal field, and grain structure for -Y and +Z directions MF are shown in Fig. 30. The same strength of the MF $|\vec{B}| = 0.5 \text{ T}$ was applied at the -Y and +Z directions, respectively. The external -Y direction MF has a keyhole-like effect, generating a deep but narrow melt pool and changing the grain size and distribution of the microstructures (Fig. 30b, e, and h). The grain development at the bottom of the narrow pool is suppressed by the hot, molten liquid, and the cool liquid rises to the surface. The grains in the bottom are encouraged to surpass the grains close to the surface by the strong temperature gradient (Fig. 30h). However, the strong Lorentz force induces a swirl at the front of the melt pool in the +Z direction magnetic field (Fig. 30c). The deflection generates a shallow and broad melt pool and affects the microstructure evolution (Fig. 30f and i). Therefore, different microstructures can be produced by adjusting the temperature gradient, the shape and size of the melt pool with different intensities and directions of MF.

Since the current research about MF is still focused on low magnetic intensity (generally less than 1 T) and non-ferromagnetic material, more work is needed to understand the influence of high magnetic intensity and ferromagnetic materials of the M-FAAM process. In addition, simulations of the effect of the MF on defects (such as voids, pores, and cracks), their reduction and mitigation are still scarce in the literature.

7.3. Acoustic field-assisted AM simulation

The working principle of the acoustic field (AF) in the AM process has been explained in Section 3. The primary influence of the AF is acoustic cavitation and streaming, which can generate sound pressure and inertial force in the melt pool and affect the fluid flow and microstructure. To simulate the A-FAAM process, the momentum

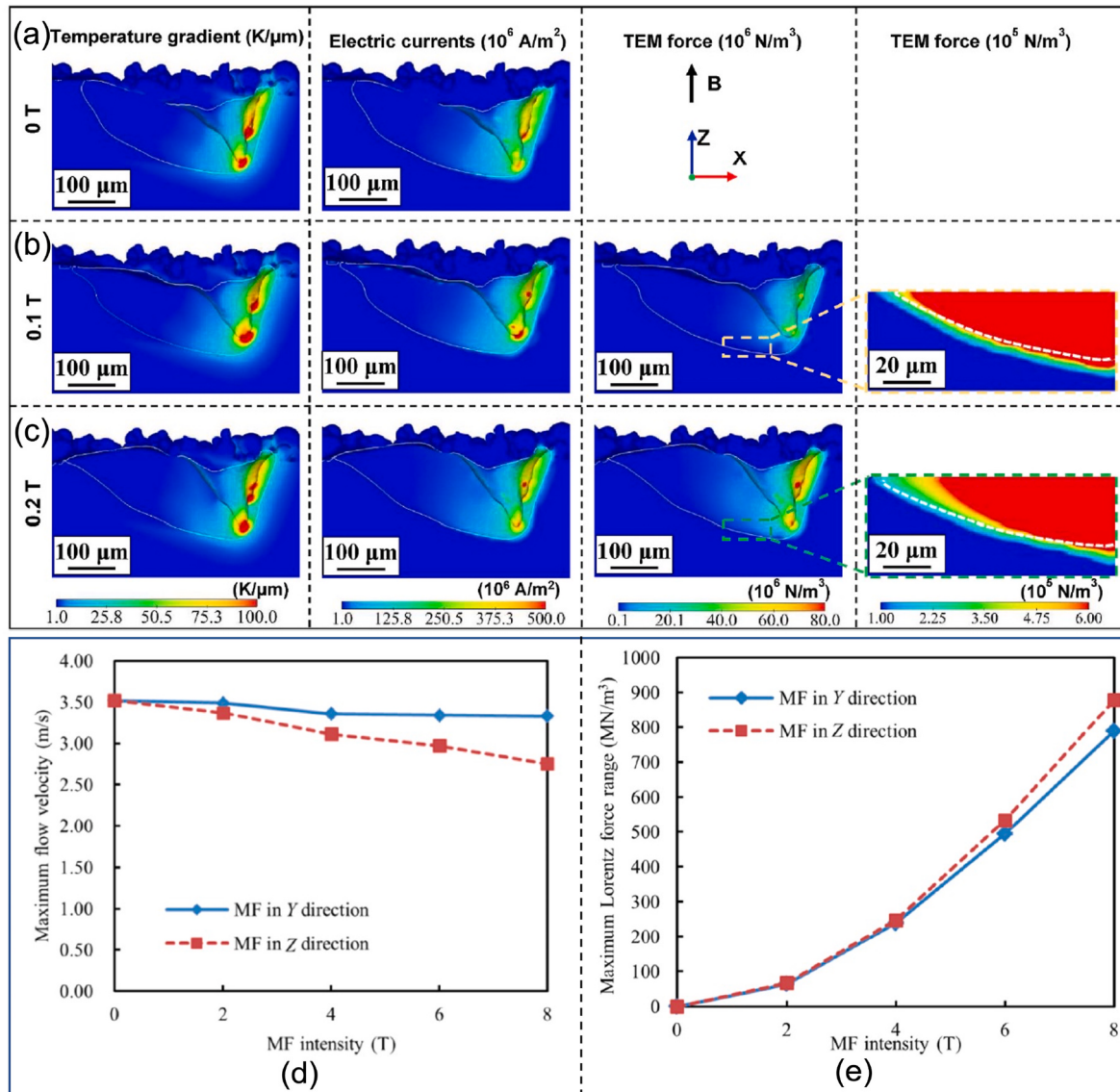


Fig. 29. Influence of magnetic field (MF) on the temperature, temperature gradient, electric currents, thermo-electric-magnetic force, velocity, and Lorentz force. Simulated results of AlSi10Mg alloys fabricated by LPBF under various MF intensities at $t = 1503$ s, (a) without magnetic field, with a magnetic field intensity of (b) 0.1 T and (c) 0.2 T [44], (d) Maximum flow velocity magnitude and (e) maximum Lorentz force of the melt pool under various intensities of MF [198].

conservation equation needs to be updated to include the ultrasonic vibration-induced sound pressure and inertial force (Eq. (19)). The updated momentum conservation equation, along with other governing equations are used to compute the temperature [81,209,210] and velocity fields [78,81,210], microstructure, residual stress, and deformation, same as the methods used for AM (Table 9). The calculations for the threshold values of sound pressure for the cavitation [74,78], ultrasonic intensity, and induced force [81,210] are explained in Section 3. It is worthwhile to note that different boundary conditions may need to be set up for various acoustic fields. In some cases, there is a distance between the ultrasonic vibration (USV) and heat source (referred to as follow-up USV in Section 3), and the sound intensity in the melt pool may affect by this distance [74]. In addition, USV can also lead to some displacement loads, depending on the distance between the USV and the melt pool [74]. Sometimes, the ultrasonic amplitude is assumed to be a constant value when the ultrasonic probe sets up just below the heat source (named substrate USV in Section 3) [78].

A commercial program, FLOW-3D, is used for the multi-physics heat transfer and fluid flow simulation for the WAAM with and without the USV process [78]. The calculated cross-section files have been

well-tested and validated by corresponding measured cross-section files in Fig. 31a and b for the cases with and without USV. In addition, the longitudinal sections for the cases with and without USV are shown in Fig. 31c. The calculated results for the cross-section and longitudinal section are available in Fig. 31a, b, and c. Both the simulation and experimental results show that the inertial force caused by the USV promotes the fluid flow forward and backwards along the scanning direction and forms a shallow but wide pool. The influence of USV on the fluid flow is also indicated in Fig. 12d (in Section 3) and Fig. 32c, d, g, and h. A schematic cross-section of the melt pool given in (Fig. 31d) further elucidates the influence of USV in the melt pool on the microstructural evolution. Another important finding shows that the external ultrasound field has a trend towards increasing surface roughness of LDED parts and forming fish-scale ripples on the top surface by the calculated and measured results in Fig. 32a, b, e, and f [81]. The main reason for the rough surface formation is the high fluid flow near the pool edges driven by the ultrasound field-induced inertial force. Further simulation work is still needed to explore and explain the microstructural evolution, residual stress, distortion, and defect formation in the AM process with and without ultrasound.

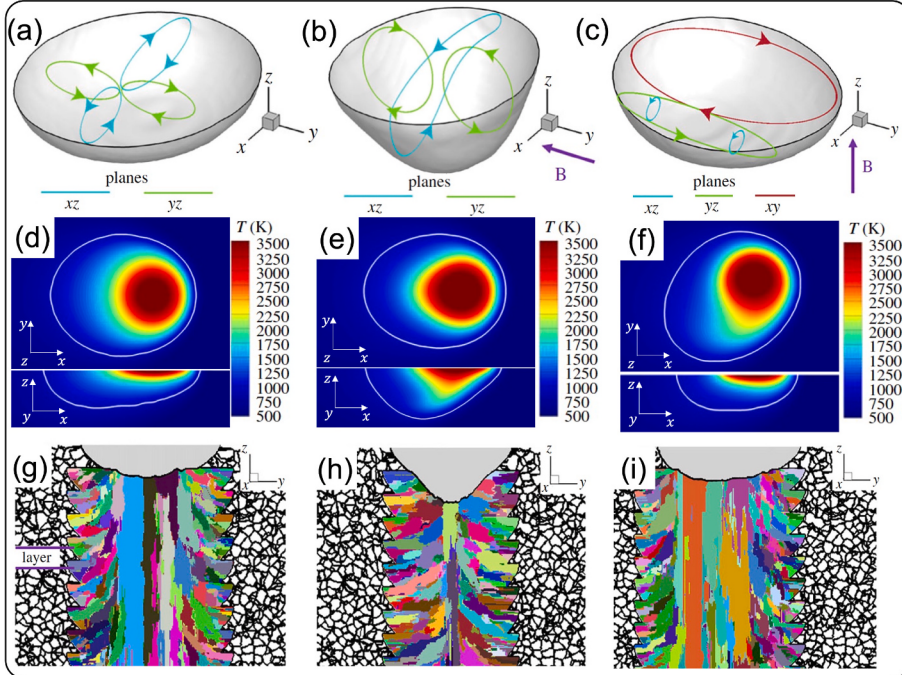


Fig. 30. Fluid flow hydrodynamic mechanism, temperature field, and microstructure with and without magnetic field (MF) for Al10Si alloy [208]. The hydrodynamic mechanism for Al10Si alloy processed by LPBF (a) without MF, (b) with -Y direction MF, and (c) with +Z direction MF, Thermal field for (d) without MF, (e) with -Y direction MF, and (f) with +Z direction MF, Cross-section of microstructure perpendicular to scan direction for (g) without MF, (h) with -Y direction MF, and (i) with +Z direction MF. Microstructure depends on the temperature gradient and pool shape and size, which can be adjusted by applying different intensities or directions of MF.

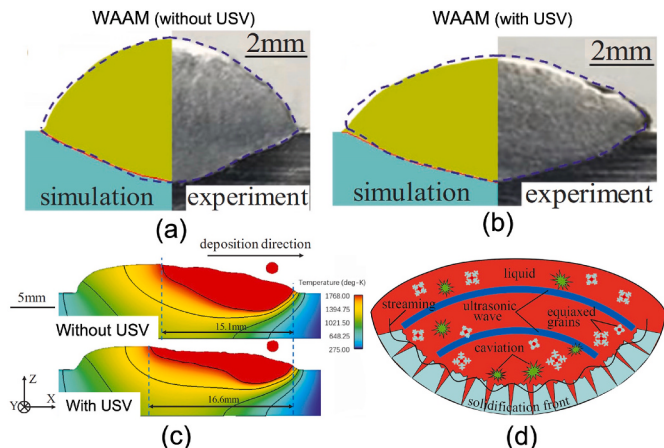


Fig. 31. Simulation results using FLOW-3D for WAAM with and without ultrasonic vibration of 1045 steel [78]. Cross-sections for the WAAM parts (a) without and (b) with ultrasonic vibration, respectively, (c) the longitudinal section of the melt pool along the symmetry surface (XZ plane), (d) the schematic cross-section of the melt pool with acoustic streaming and cavitation.

7.4. Thermal field-assisted AM simulation

The thermal field (the auxiliary heating) is applied for AM process to adjust the temperature field [101,119,211], such as hybrid-source heating and substrate heating explained in Section 4. For the T-FAAM process simulation, adding external heat sources [119,212,213] or tuning the boundary conditions [106,214] according to the experimental setup is an effective way to calculate the temperature field [215–217]. In addition, among available auxiliary fields, unlike the MF, AF, and DF, the TF is the only one applicable to use the heat conduction model to calculate the temperature field [218]. The TF has minimal influence on the velocity within the melt pool, especially in the post-heating, parallel laser heating process [212]. The change in the temperature field, shape and size of the melt pool caused by the additional TF affects the microstructure, residual stress, and distortion.

However, the modelling approach for calculating the velocity field, microstructure, residual stress, and distortion of the TF-assisted AM process is the same as those methods used for AM (see Table 9).

Some simulation results have been performed by ABAQUS and COMSOL Multiphysics to compute the temperature and residual stress fields [101,119,211]. Zhang et al. [212] investigated the influence of parallel heating, preheating, and post-heating by a second laser beam for the LPBF process. Two heat sources are applied for the calculations of power density, peak temperature, cooling rate, and stress for various conditions (Fig. 33). Among three different modes of heating, post-heating is found as the most effective way to reduce stress for most of the investigated cases (Fig. 33h). However, this model has not been validated by experimental data. It's also important to consider the impacts of phase transition temperature on the residual stress [119]. J.X. Fang et al. [119] applied a FEM model to estimate the residual stress distribution with/without preheating and under different phase transition points for a multi-layer and multi-pass laser metal deposition (Fig. 34). This model has been well-validated by testing results using neutron diffraction measurement. They found that when no preheating is used, as the temperature drops to the solid phase transition temperature (200 °C), the longitudinal tension stress rapidly decreases from a high value in (Fig. 34a). It suggested that there is a tensile stress relaxation effect during the low-temperature solid phase transition. When the lowest temperature is higher than the solid phase transition point (~200 °C), a preheating of 200 °C has less impact on the final values of residual stress (Fig. 34b). When the solid phase transition temperature is high (>400 °C), the preheating can increase the lowest temperature of heat cycle above the solid phase transition temperature and increase the tensile stress relaxation effect (Fig. 34c and d) for a low value of residual stress at the end.

With the help of an external thermal field, the residual stress distribution can be tuned and optimized, which significantly influences the deformation and distortion of large components. Although some work has been done to model the temperature and residual stress field with the assisted thermal field, further investigation is needed to understand the influence of the assisted thermal field on microstructural optimization, defect formation and mitigation, and mechanical properties in the future.

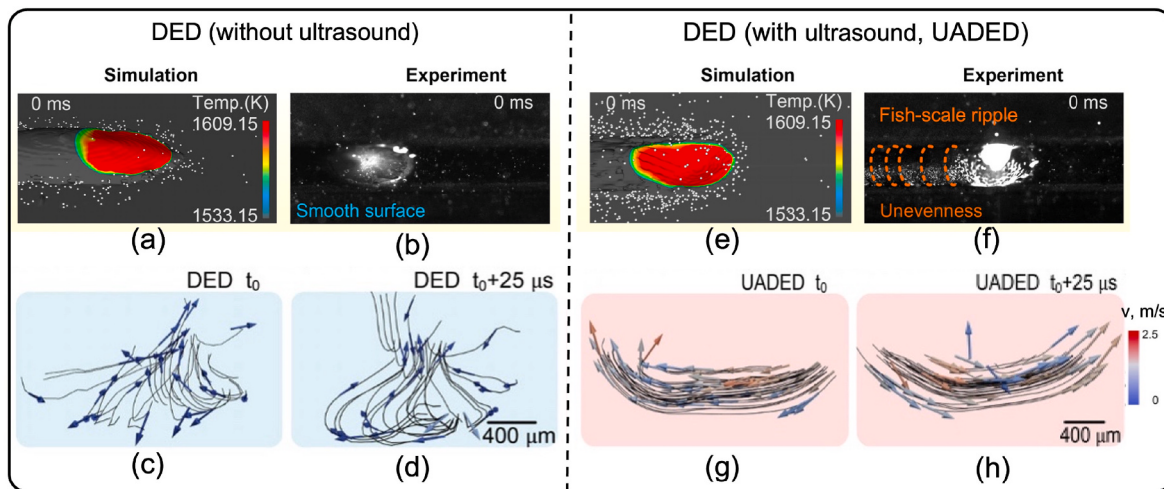


Fig. 32. Melt pool and streamlines in the LDED process with and without ultrasound for Inconel 718 [81]. For LDED without ultrasound condition: (a) calculated results of the dynamic melt pool, (b) experimental images display the instantaneous melt pool morphology, streamlines at (c) t_0 and (d) $t_0 + 25 \mu\text{s}$. For ultrasound assisted LDED (UADED) condition: (e)calculated results of the dynamic melt pool, (f) experimental images display the instantaneous melt pool morphology, streamlines at (g) t_0 and (h) $t_0 + 25 \mu\text{s}$.

7.5. Mechanical deformation field assisted AM simulation

Mechanical deformation field [219–221] is applied to assist AM process in adjusting the temperature field [219,220,222], microstructure [220], and residual stress [219,222,223] by rolling, machine hammer peening, and laser shock peening, as introduced in Section 5. For the D-FAAM process simulation, the modelling approach for temperature and velocity fields is the same as that used for AM. However, the microstructure is affected by the external pressure/load from mechanical deformation, which can cause dynamic recrystallization, nucleation, and grain growth. The microstructure changes in ways due to the mechanical deformation that is the same as in the metal forming [224–226]. It means that the modelling approaches for metal forming can be applied to the microstructure evolution calculations caused by the external mechanical deformation field. In addition, mechanical deformation plays a crucial role in residual stress and distortion. The varying pressure/load from mechanical deformation is applied as either boundary conditions or body forces in stress and strain calculation. The way to calculate the influence of mechanical deformation on residual stress is the same as the modelling of rolling, peening, and wire drawing [227–229] (Table 9).

Some work has been done in ABAQUS for the temperature and stress fields calculation (Fig. 35a and b) for the WAAM process [220]. Nucleation and grain growth simulation during solidification can be calculated with the results of temperature and stress fields (Cellular Automata model). Then, the strain field is updated with the dislocation density caused by the roller. Last, nucleation and grain growing calculations in the dynamic recrystallization process caused by the roller are based on the WAAM microstructure and dislocation density [220]. The simulation results are available for solidification (Fig. 35c–e) and dynamic recrystallization (Fig. 35f–h, k) for the hybrid deposition and micro-rolling process (HDMR) at various Cellular Automata (CA) steps and different rolling reductions (ΔH) (Fig. 35i and j). Large rolling reductions increase the thickness of the refined microstructure under the top surface. However, this model has not been tested by experimental measurement [220].

For the mechanical deformation-assisted AM process residual stress simulation, the residual stress primarily depends on the roller design, roller load, roller profile radius, and initial residual stress of the AM process [219,222,223]. Abbaszadeh et al. [230] applied FEM model to calculate the residual stress for the WAAM process and the rolling process. In this work, they found that the maximum equivalent von Mises

stress increases by reducing the roller profile radius (Fig. 36a and b) or increasing the rolling loads. However, both the initial residual stress and friction coefficient have a negligible effect on the residual stress (Fig. 36c–e). It means that the value of initial residual stress caused by the AM process is less compared to that caused by the external mechanical deformation field. In addition, second-order polynomial regression is used to derive an equation from calculating the equivalent plastic strains using the rolling load and roller profile radius for Ti6Al4V, S355JR, and AA2319 alloys [230]. This model has been well-validated by corresponding compression experimental tests. To investigate the influence of roller design on residual stress for the WAAM process, the residual stress of three different designs of rollers is simulated [222] and the calculated results are validated by corresponding experimental results. They found that the slotted roller is the best one to reduce the tensile residual stress compared to the flat and profiled rollers (Fig. 36f and g) [222]. Further details with regard to residual stress simulations with FEM are given in (Table 8).

Some work report that both compressive stress and dynamic recrystallization can reduce internal defects (such as pores and micro-cracks) and improve mechanical properties (such as YS, UTS, and fatigue life) [222,223,230]. Shock peening is another commonly used way of mechanical deformation [148,219,221]. A mechanistic understanding of the influence of mechanical deformation on microstructure revolution and residual stress is helpful for roller design (in shape and size, such as profile radius) and process variable selection to optimize the grain distribution, residual stress, and distortion. However, more effort is still needed to simulate and understand defect evolution and reduction for AM processes assisted by mechanical deformation.

For further development of FAAM simulations, there are many uncertain parameters in the equations for FAAM process calculation, such as the source terms in the conservation equations. These uncertain variables need to be appropriately selected for a precise calculation. In addition, for some simulations which are computationally expensive and require hundreds of hours, there is a need for quantum computing to shorten the calculation time and make the simulation cheaper for researchers. Compared to AM, FAAM is more complex to understand and simulate. For someone who doesn't have a basic understanding of the FAAM, machine learning may be a good choice to investigate the FAAM with no requirement for understanding the inherent mechanisms. However, machine learning needs sufficient data to train the algorithms. With the rapid development of the AM and FAAM, a better understanding of the process will help to make the AM and FAAM components

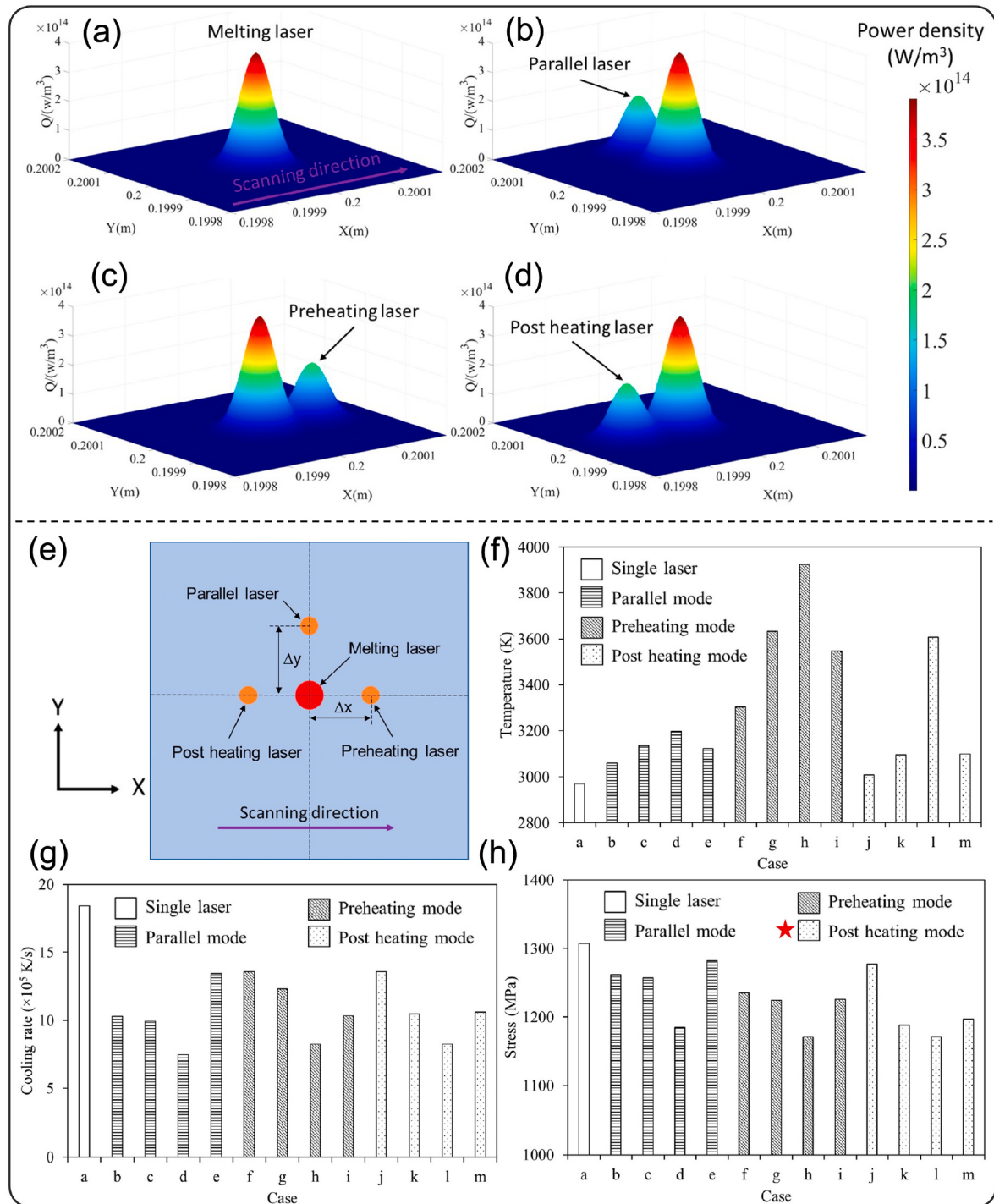


Fig. 33. Influence of thermal field-assisted AM process on power density, temperature, cooling rate, and stress for Ti6Al4V alloy [212]. Illustration of the Gaussian distributed heat sources for LPBF modelling for (a) a single laser beam, an auxiliary heat source of (b) parallel laser heating, (c) pre-heating laser, and (d) post-heating laser, (e) illustration of three different modes of a second laser beam of parallel, post-heating, and preheating modes, comparing the calculated results for (f) peak temperature, (g) cooling rate, and (h) stress for three heating modes under various conditions, post-heating is found as the most effective way to reduce stress.

cheaper and more commercially friendly.

7.6. Field-assisted AM model validations

Because practically all FAAM mechanistic models are approximate and built on some assumptions, they should be tested and validated to the extent required for the intended use. FAAM mechanistic models are often verified by comparing model outputs to corresponding experimental results under various processing conditions. It is crucial to decide

which experiment needs to be conducted to validate a model. The experiments are designed according to the variables that the model can calculate. For example, if the model calculates the temperature distribution of the FAAM process, thermocouples, and infrared (IR) thermography using IR cameras and pyrometers are available techniques for measuring the temperature. The temperature measurement accuracy and reliability depend on the testing range, sensitivity, and calibration of the thermocouples, wavelength, and frames per second (fps) of the IR cameras. The thermocouples are embedded in advance to measure the

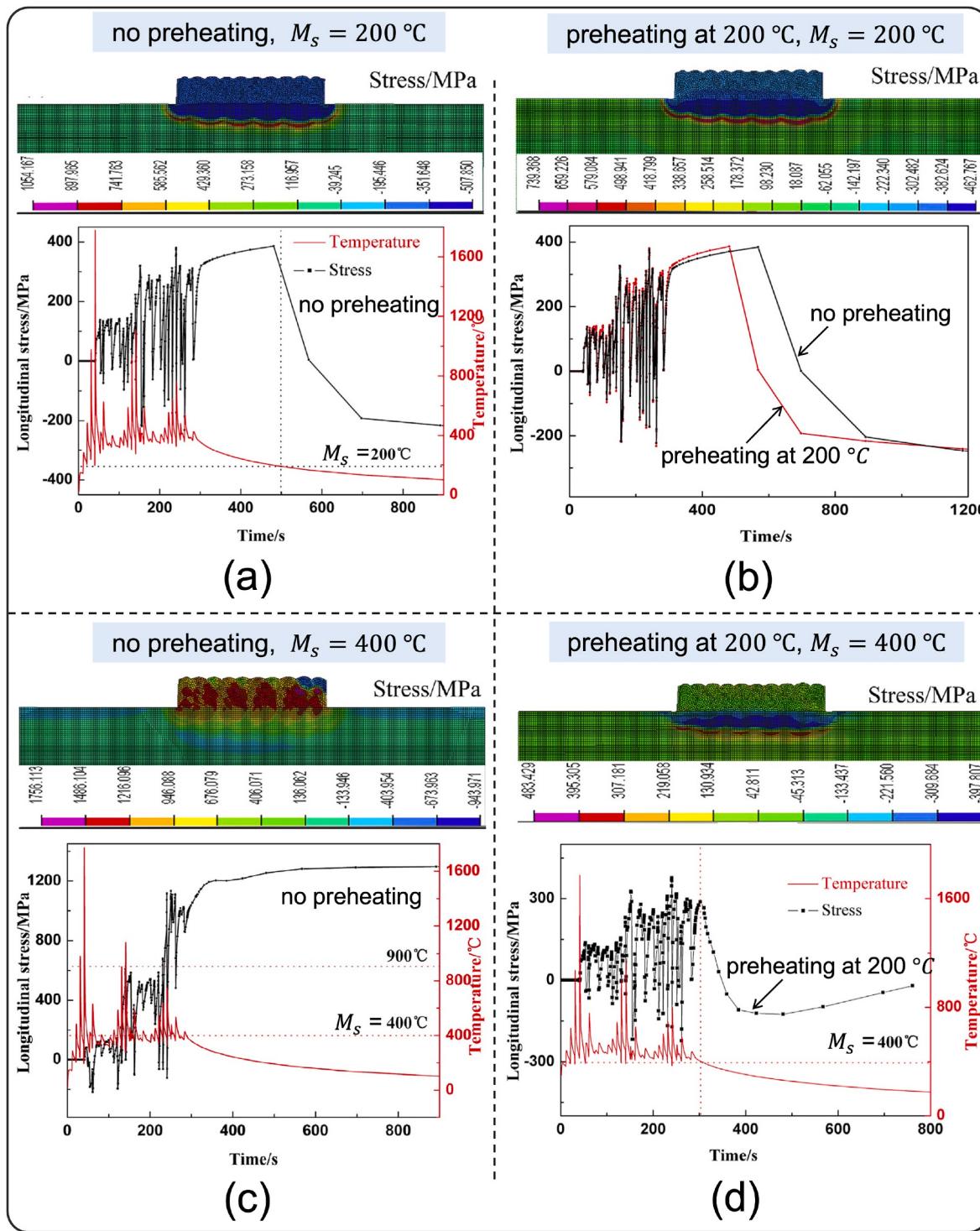


Fig. 34. Simulation results of longitudinal residual stress and temperature for LPBF process under various phase transition points (M_s) and with/without pre-heating using FV520B steel as substrate and Fe–Cr–Ni–Mo–B–Si powder [119]. Longitudinal residual stress distribution and temperature of the mid-point of the fifth pass in the first layer for (a) without preheating, $M_s = 200^\circ\text{C}$ (b) preheated at 200°C , $M_s = 200^\circ\text{C}$, (c) without preheating, $M_s = 400^\circ\text{C}$, and (d) preheated at 200°C , $M_s = 400^\circ\text{C}$.

temperature history curve of a small region near the melt pool to measure the temperature history curve if the solidus temperature of the alloy is higher than the working temperature range of thermal couples [231]. A high-performance IR camera is better to capture the dynamic temperature distribution for the surface temperature measurement [231]. However, an accurate temperature measurement inside the melt pool region remains challenging. The main challenge is the difficulty of

developing a temperature measurement device with a large testing range, high-temperature sensitivity, small testing errors, and ease of setup and removal.

In addition to the temperature field, some models can calculate fluid flow for FAAM. However, it is difficult to measure the velocity of the liquid metal within a small size pool for a rapid transient process like AM and FAAM. Tracer particles are commonly used to track liquid

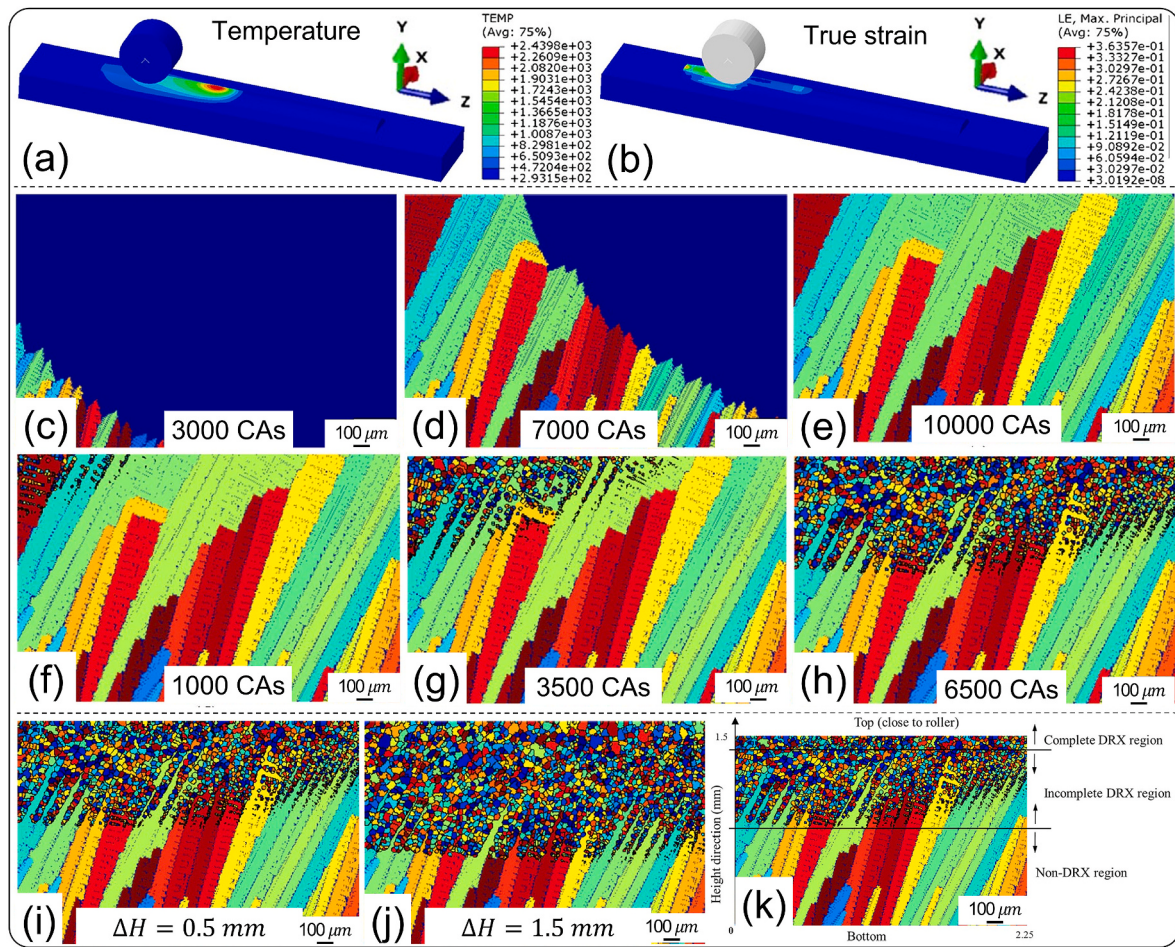


Fig. 35. Results of thermo-mechanical simulation, solidification simulation, and dynamic recrystallization simulation for carbon steel [220]. Thermo-mechanical coupling simulation of the hybrid deposition and micro-rolling (HDMR) process of (a) temperature (in K) and (b) true strain distribution, Microstructure evolution during the HDMR process, solidification simulation at different Cellular Automata steps (CAs) of (c) 3000 CAs, (d) 7000 CAs, (e) 10000 CAs, recrystallization simulation at (f) 1000 CAs, (g) 3500 CAs, (h) 6500 CAs, simulation results of dynamic recrystallization at 6500 CAs under rolling reduction (ΔH) of (i) 0.5 mm and (j) 1.5 mm, (k) schematic of statistic for dynamic recrystallization grains.

movement by their spatiotemporal distribution [232], such as tungsten and tantalum particles. Since the temperature and velocity fields decide the melt pool shape and size, the cross-section of the FAAM samples can be compared with the corresponding calculated temperature and velocity fields, such as Fig. 31a and b. In addition, the in-situ stress measurement is challenging, but ex-situ residual stress measurement is available to validate models.

Validation of different models requires experimental datasets of process conditions, temperature, cross-section, residual stress, and other tested profiles for various alloys. Some standardized datasets provided by the National Institute of Standards and Technology (NIST) in the United States are available for laser welding [233] and AM process [234] models' validation. FAAM experimental research papers are encouraged to provide necessary testing profiles and experimental details which can be used for new-developed model validations in the future. More public experimental datasets are encouraged and helpful for the development and validation of FAAM modelling and simulation.

8. Summary and perspectives

8.1. Summary

This work reviewed various auxiliary fields used to assist AM processes, including the mainstream fields such as acoustic, thermal, magnetic, and mechanical fields, as well as the emerging plasma and electric

fields and coupled multi-fields. The interaction mechanisms between auxiliary mainstream fields and materials are summarized in Fig. 37.

The magnetic field will affect the melt pool convection in AM due to the TEMC and damping effect, which could reduce melt pool velocity, resist backward flow, and change the temperature gradient of the melt pool. Besides, TEMF on dendrites during solidifications (as illustrated in Fig. 37) could break the dendrites and promote equiaxed microstructures formation (i.e., CET) by acting as nucleation sites and thus inducing a transformation to an equiaxed structure through a lower free energy barrier than usual. In contrast, the acoustic field will affect the melt pool dynamics during AM, since the high-density ultrasound will agitate the melt pool flow inducing stirring and mixing effects and leading to cavitation bubbles or clouds (as illustrated in Fig. 37). Besides, the acoustic energy can break the dendrites and promote the CET. The auxiliary thermal field in AM will not affect the melt pool dynamics; however, it can control the thermal history of the AM-built part. Specifically, the thermal field could not only reduce the temperature gradient and achieve a more homogeneous temperature distribution but also bring about in-situ heat treatment to the deposited materials. Meanwhile, the thermal field (e.g., hot-wire process) possesses the highest potential in improving the deposition rate of materials due to the extra thermal energy input. Furthermore, the thermal field showed the ability to promote equiaxed growth due to the decreased temperature gradient. Unlike magnetic and thermal fields, which interact with materials without contact, the mechanical fields primarily affect the AM

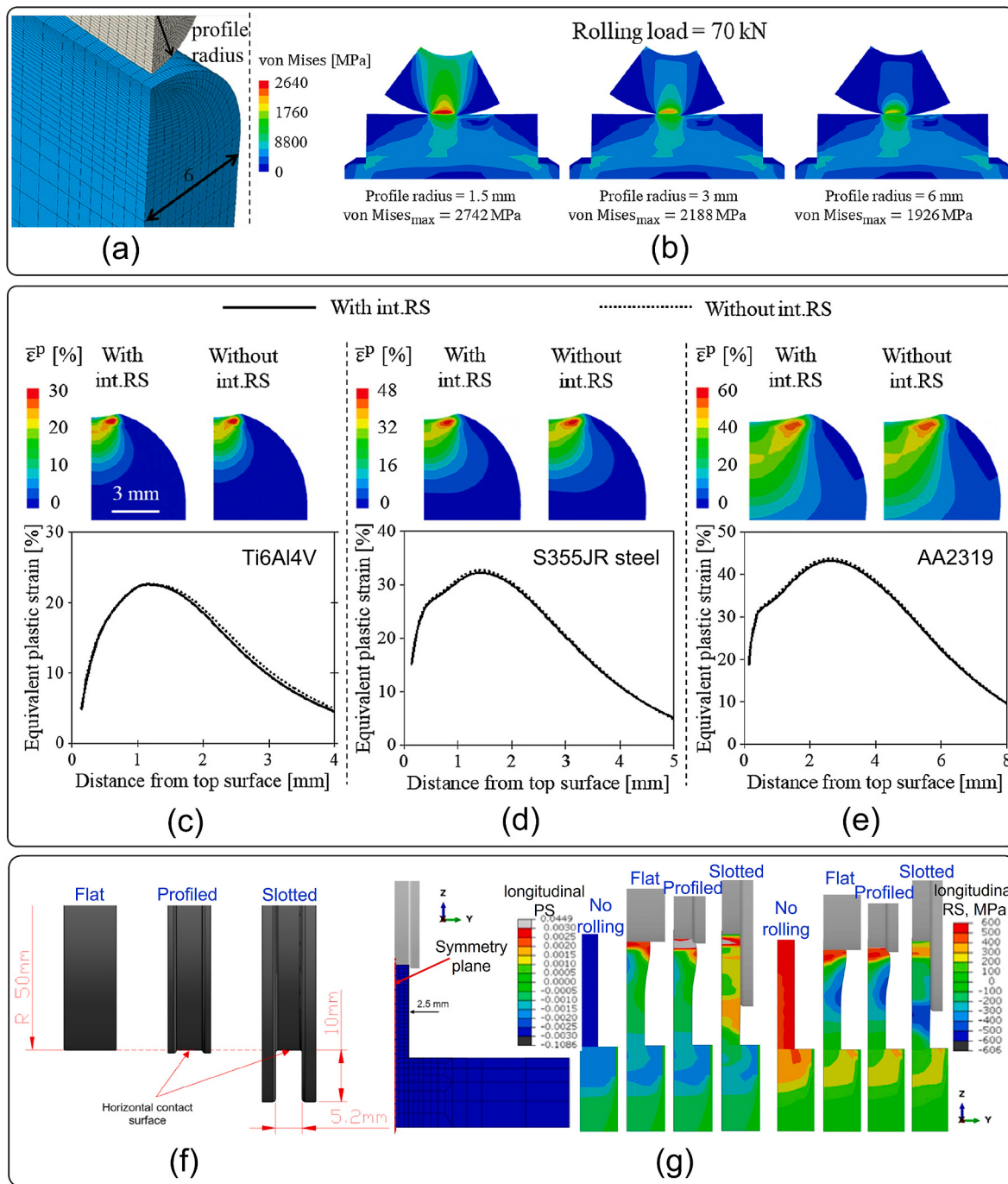


Fig. 36. Influence of roller profile radius, initial residual stress, and roller design on residual stress. (a) roll profile radius, (b) simulated residual stress with profile radius of 1.5, 3, and 6 mm [230], compare the final residual stress distribution with and without initial residual stress (int. RS) field for (c) Ti6Al4V, (d) S355JR steel, and (e) AA2319 alloy, $\bar{\varepsilon}^p$ represents the equivalent plastic strain [230], (f) design of flat, profiled, and slotted rollers with roller radius of 50 mm [222], (g) longitudinal plastic strain (PS) and residual stress (RS) distributions obtained from the symmetry plane of WAAM wall [222], with the substrate steel grade S355JR-AR and Lincoln Electric SupraMIG G3Si1/ER70S-6 wire.

deposits through contact by inducing plastic deformation to the workpiece, which will cause dynamic recrystallization and high stored energy in the deposited materials, therefore bringing more dislocations and preferential nucleation sites to materials.

The interaction outcomes between auxiliary fields and materials in FAAM are summarized in Fig. 38, which highlights the improvement in AM process and deposits in terms of process stability, surface quality and densification, residual stress, microstructure, mechanical properties, and fatigue performance. Incorporating an auxiliary field process has several advantages, which will be elaborated on as follows.

(i) **Improve the printability and densification of materials.** The use of an auxiliary field improves printability, surface roughness, and forming quality and alleviates cracking behaviour during AM. The addition of a thermal field during AM reduces the temperature gradient and therefore reduces the internal thermal residual stress and cracking tendency of materials. Besides, the thermal field could also improve the density of the AM-processed part by consolidation and crack mitigation [114]. Similarly, the auxiliary mechanical field (e.g., rolling, hammer forging and

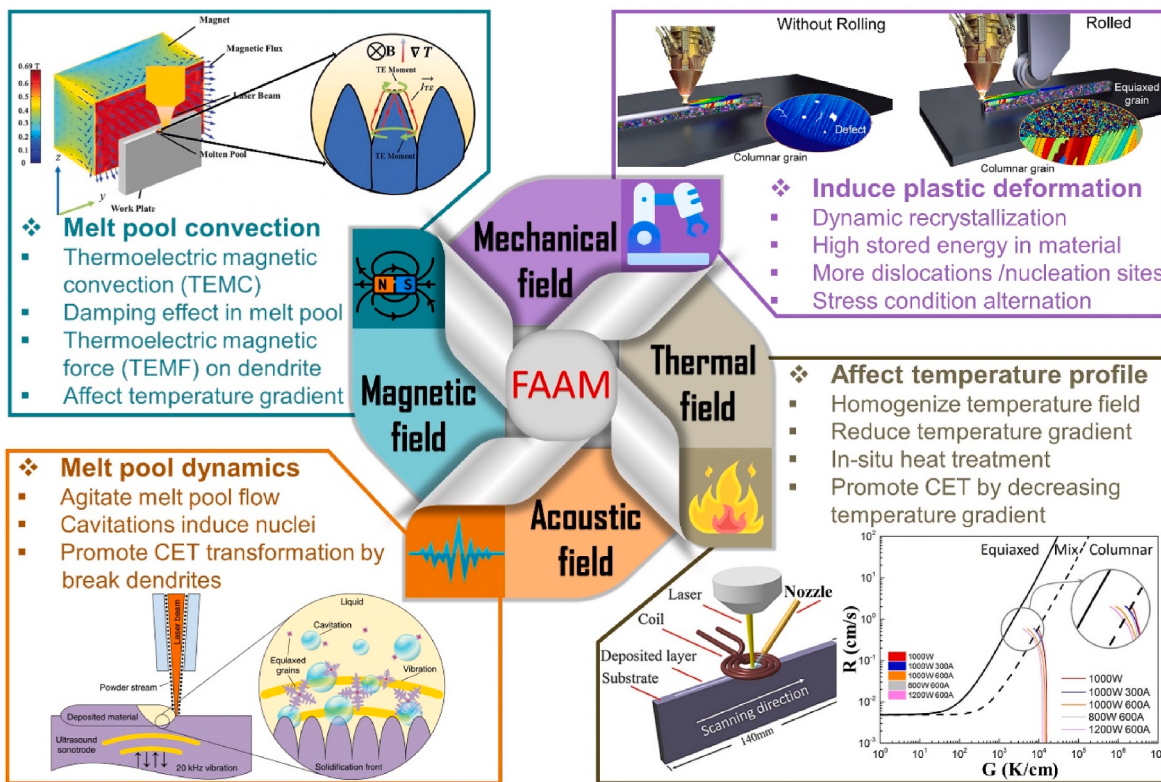


Fig. 37. A summary of underlying mechanisms for material-field interactions in FAAM. Image source from Refs. [49,72,98,220].

laser shock peening) have been shown to coalesce the internal voids and improve the densification of material.

(ii) **Control the solidification behaviour and tune the microstructure.** Auxiliary physical fields (e.g., magnetic, ultrasonic and thermal fields) affect the fluid flow and heat transfer mechanisms in the melt pool, which effectively changes the nucleation, growth and coarsening behaviours during solidification, and therefore allows modification of the microstructures as they are solidifying [45]. Additionally, the mechanical field could lead to the recrystallization and significant grain refinement of

microstructures due to the deformation after solidification [133]. The large deformation also promotes precipitation due to the high stored energy and more potential nucleation sites [247].

(iii) **Alleviate anisotropy in mechanical properties and enhance mechanical performance.** The columnar grains oriented along the build direction, formed through epitaxial growth, cause property anisotropy. The application of auxiliary magnetic, acoustic and mechanical deformation fields can promote the formation of refined and equiaxed grains during melt pool solidification [72] and dynamic recrystallization under

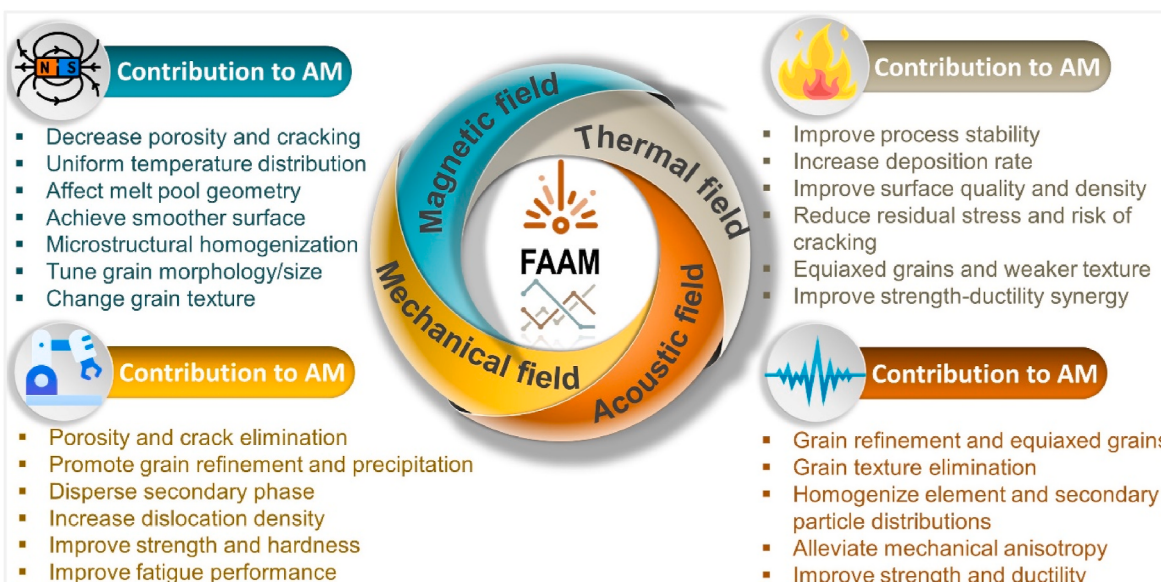


Fig. 38. A summary of the contribution of auxiliary fields to additive manufacturing in FAAM.

deformation [156], demonstrating the high potential to achieve improved mechanical properties after replacing coarse columnar grains [72,156].

- (iv) **Improve fatigue performance.** The residual tensile stresses in AM-processed metallic materials have a negative effect on the FCG resistance and ductility of the material, as they can promote the opening of the cracks [154]. The alleviation of detrimental residual stresses by the application of a mechanical deformation field or thermal field has been shown to improve the ductility and fatigue performance of the AM-processed components. Furthermore, fatigue failure generally originates from the nucleation of cracks at micro-voids and surface cracks; the reduced surface porosity and closing of cracks in materials by mechanical deformation field also improve fatigue performance.

8.2. Perspectives

This section will provide further insights into some key research and development priorities to further advance and mature the FAAM technique and enhance FAAM processing capabilities. The perspectives on manufacturing innovation, principle investigation, materials development, and performance enhancement are summarized in Fig. 39. These are elucidated below point by point.

8.2.1. Process innovation and system qualification

As aforementioned, each FAAM has its merit and weakness. The interaction of multi-fields to assist AM could bring more opportunities in tailoring the microstructure and mechanical performance of the deposited materials. For instance, the coupling of the magnetic-thermal-deformation fields in AM has the potential to improve the strength, ductility, and fatigue performance of the materials. Because the magnetic field could facilitate equiaxed grain formation [53], alleviate mechanical anisotropy and improve ductility, while the thermal field has the capability to in-situ form strengthening precipitates in the materials for better strength. Meanwhile, mechanical deformation is feasible to enhance fatigue performance by eliminating defects, refining grains, and inducing compressive stress in the materials [129]. Besides, the ultrasonic vibration can stir and mix the melt pool, which could be

potentially used to solve the homogeneity in AM of composite powders. FAAM is also expected to have high flexibility in processing high-geometry-complexity components and good scalability in depositing large or small free-form components. This raises high challenges in process and system developments as it requires uniform field distribution in 3D volume. Breakthrough of uniform field distribution will improve the flexibility and scalability of FAAM technologies, as well as mature and expand their applications.

FAAM system qualification and commercialization is another progress direction since current FAAM equipment is mostly experimental without rigorous testing and qualification. The lab-stage FAAM technologies could suffer from stability and repeatability issues, which are not qualified enough for processing reliable industrial products. Therefore, rigorous system qualification is requested to commercialize the FAAM technique. At the same time, the standards for FAAM system qualification also need to be developed and compiled to guide and certify the qualification for commercial purposes. The availability of reliable commercial FAAM equipment will attract more researchers to advance and implement FAAM technologies in industrial applications. Although the capital equipment costs in the FAAM techniques are increased, the benefits to processing capability enhancement and part performance may outweigh the cost significantly [107].

8.2.2. Field-material evolution simulation and mechanism investigation

The establishment of systematic knowledge on FAAM, in terms of field-material interaction mechanisms, microstructural evolution at different scales, and the relationship between field and material property, are critical to mature and guide the further development of FAAM technologies. Simulation, along with in-situ monitoring, is a powerful approach to understanding field-material interaction and evolution. An investigation into the underlying physical mechanisms is also essential to understand and better utilize the effect of auxiliary fields. Such as how the nucleation and phase transformation happen in the thermal or mechanical deformation fields based FAAM, and how the auxiliary fields affect the strengthening and toughening mechanism of the materials.

8.2.3. Customized materials development for FAAM

Customization of material for AM is an ongoing development trend

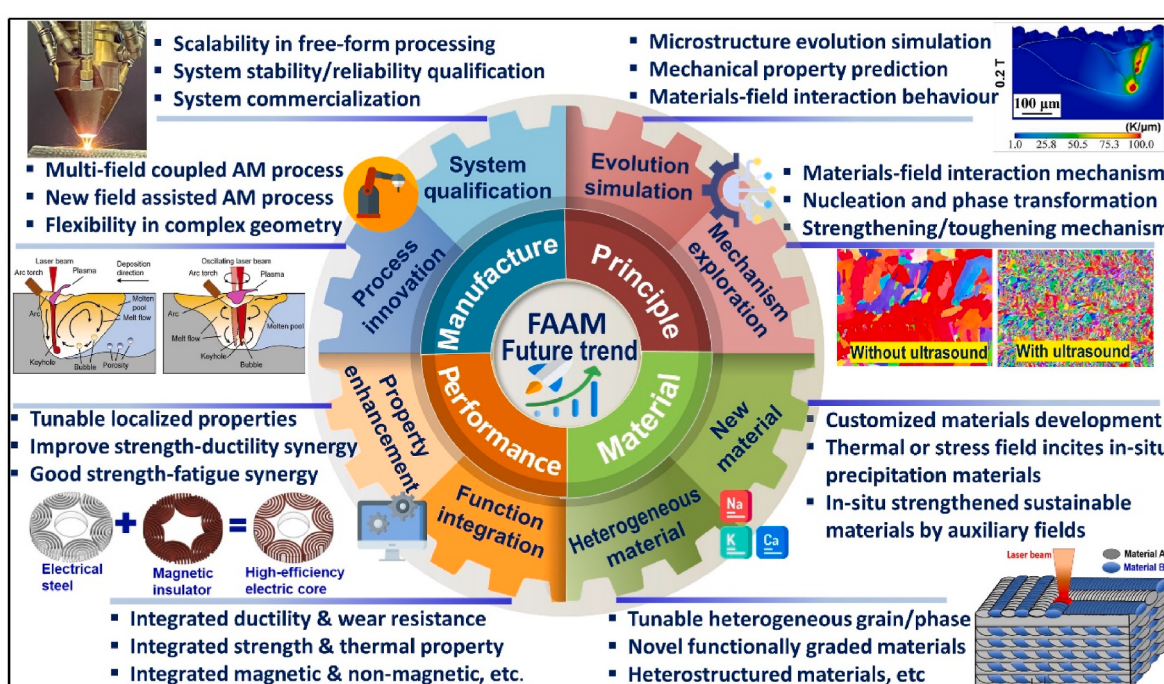


Fig. 39. The perspectives in future R&D of FAAM. Image source from Refs. [21,44,72,248,249].

[250]. Apart from the system and process advancements, innovations in co-designing materials and manufacturing processes should also be highlighted. The auxiliary fields in AM provide opportunities to develop new materials. Recent drives to develop materials tailored explicitly for AM could also take into account the development of materials tailored for FAAM [251,252]. Hence, it is essential to frame FAAM from a materials design perspective to ultimately take advantage of auxiliary fields, such as the thermal field and mechanical deformation field. For instance, the thermal field can be utilized to promote the formation of precipitates (such as the metal carbides [253] and intermetallics [254]) and tune phase constitutions (such as the fraction of BCC and FCC phases in steel [255]). To avoid over or insufficient heat treatment, novel materials may need an extensive range of heat treatment duration to enable long-time deposition [256]. Besides, large deformation associated with mechanical fields can promote recrystallization and in-situ precipitation due to their high stored energy and more potential nucleation sites, respectively. Materials with fast precipitation kinetics are possible to achieve in-situ precipitation during auxiliary mechanical field processing. Besides, the deployment of an acoustic field in AM is possible to disperse detrimental hard phase segregations, which also provides a good opportunity to accommodate high-density hard phase (e.g., Laves phase in steel) in materials to strengthen the materials as a beneficial phase.

The heterostructured and functional materials are also feasible to be developed with FAAM. For instance, the mechanical field could be utilized to develop BCC/FCC heterostructured materials when FAAM of an FCC material since the mechanical strain can induce the transformation from FCC to BCC. Specifically, in the layerwise deposition, applying mechanical strain (e.g., rolling or hammer peening) alternately could obtain layerwise BCC/FCC heterostructured dual-phase component, which is possible to achieve improved mechanical performance [249].

8.2.4. Property enhancement and functionality integration

AM has demonstrated exciting capabilities for fabricating complex geometries unobtainable via traditional methods. Nevertheless, the complexity of the material within a component lacks exploration since current metal AM technologies are limited to monolithic materials and lack programmatic control over the printed microstructure. The employment of an auxiliary field during AM could tune grain size/shape, phase constitution, and stress level/condition locally in a component, which is capable of defining the property and performance at different regions to enhance the overall performance of the component, such as strength-ductility synergy, strength-fatigue combination, integrated ductility and wear resistance, integrated strength-thermal property, and integrated magnetic and non-magnetic components, etc. The realization of such a fabrication pathway is vital to unlocking the unparalleled potential of the FAAM technique.

CRediT authorship contribution statement

Chaolin Tan: Writing – review & editing, Writing – original draft, Project administration, Funding acquisition, Conceptualization. **Runsheng Li:** Writing – review & editing, Writing – original draft, Validation, Methodology. **Jinlong Su:** Writing – review & editing, Writing – original draft, Formal analysis. **Dafan Du:** Writing – review & editing, Writing – original draft, Funding acquisition, Formal analysis. **Yang Du:** Writing – review & editing, Writing – original draft, Formal analysis, Data curation. **Bonnie Attard:** Writing – review & editing, Visualization. **Youxiang Chew:** Resources, Investigation. **Haiou Zhang:** Writing – review & editing, Formal analysis. **Enrique J. Lavernia:** Writing – review & editing, Investigation. **Yves Fautrelle:** Writing – review & editing. **Jie Teng:** Writing – review & editing, Resources. **Anping Dong:** Writing – review & editing.

Declaration of competing interest

The authors declare that they have no known competing financial interests or personal relationships that could have appeared to influence the work reported in this paper.

Data availability

Data will be made available on request.

Acknowledgments

This work was funded by the Singapore RIE 2025 MTC 2022 Young Individual Research Grants (M22K3c0097), and SIMTech SSRT program (Grant No. C21-J1-036). This work is also supported by the Natural Science Foundation of Shandong Province, China (Grant No. ZR2022ME106), the National Natural Science Foundation of China (Grant No. 52071205), Equipment Pre-reaserch Collaborative Foundation for Innovation Team from Ministry of Education of China (Grant No. 8091B042209), and the State Key Laboratory of Solidification Processing in NWPU (Grant No. SKLSP202214).

References

- [1] C. Tan, D. Wang, W. Ma, K. Zhou, Ultra-strong bond interface in additively manufactured iron-based multi-materials, *Mater. Sci. Eng., A* 802 (2020), 140642.
- [2] Z. Li, S. Sui, X. Ma, H. Tan, C. Zhong, G. Bi, A.T. Clare, A. Gasser, J. Chen, High deposition rate powder- and wire-based laser directed energy deposition of metallic materials: a review, *Int. J. Mach. Tool Manufact.* 181 (2022), 103942.
- [3] M.S. Pham, C. Liu, I. Todd, J. Lerthanasarn, Damage-tolerant architected materials inspired by crystal microstructure, *Nature* 565 (7739) (2019) 305–311.
- [4] C. Tan, J. Zou, S. Li, P. Jamshidi, A. Abena, A. Forsey, R.J. Moat, K. Essa, M. Wang, K. Zhou, M.M. Attallah, Additive manufacturing of bio-inspired multi-scale hierarchically strengthened lattice structures, *Int. J. Mach. Tool Manufact.* 167 (2021), 103764.
- [5] EOS, First Metal 3D-Printed Primary Flight Control Hydraulic Component, 2022. https://www.eos.info/en/all-3d-printing-applications/liebherr-3d-printed-primary-flight-control-hydraulic-component#video_1753. (Accessed 20 July 2022).
- [6] J.C. Najmon, S. Raeisi, A. Tovar, 2 - review of additive manufacturing technologies and applications in the aerospace industry, in: F. Froes, R. Boyer (Eds.), *Additive Manufacturing for the Aerospace Industry*, Elsevier, 2019, pp. 7–31.
- [7] C. Tan, F. Weng, S. Sui, Y. Chew, G. Bi, Progress and perspectives in laser additive manufacturing of key aeroengine materials, *Int. J. Mach. Tool Manufact.* 170 (2021), 103804.
- [8] L. Liu, Q. Ding, Y. Zhong, J. Zou, J. Wu, Y.-L. Chiu, J. Li, Z. Zhang, Q. Yu, Z. Shen, Dislocation network in additive manufactured steel breaks strength-ductility trade-off, *Mater. Today* 21 (4) (2018) 354–361.
- [9] T. DebRoy, T. Mukherjee, H.L. Wei, J.W. Elmer, J.O. Milewski, Metallurgy, mechanistic models and machine learning in metal printing, *Nat. Rev. Mater.* 6 (6) (2020) 48–68.
- [10] D. Gu, X. Shi, R. Poprawe, D.L. Bourell, R. Setchi, J. Zhu, Material-structure-performance integrated laser-metal additive manufacturing, *Science* 372 (6545) (2021), eabg1487.
- [11] T. DebRoy, T. Mukherjee, J.O. Milewski, J.W. Elmer, B. Ribic, J.J. Blecher, W. Zhang, Scientific, technological and economic issues in metal printing and their solutions, *Nat. Mater.* 18 (10) (2019) 1026–1032.
- [12] F. Xu, N. Madhaven, V. Dhokia, A. McAndrew, P. Colegrave, S. Williams, A. Henstridge, S. Newman, Multi-sensor system for wire-fed additive manufacture of titanium alloys, 26th Int. Conf. on Flexible Automation and Intelligent Manufacturing (2016).
- [13] C. Tan, Y. Chew, F. Weng, S. Sui, F.L. Ng, T. Liu, G. Bi, Laser aided additive manufacturing of spatially heterostructured steels, *Int. J. Mach. Tool Manufact.* 172 (2022).
- [14] Y. Hu, Recent progress in field-assisted additive manufacturing: materials, methodologies, and applications, *Mater. Horiz.* 8 (3) (2021) 885–911.
- [15] R. Fu, S. Tang, J. Lu, Y. Cui, Z. Li, H. Zhang, T. Xu, Z. Chen, C. Liu, Hot-wire arc additive manufacturing of aluminum alloy with reduced porosity and high deposition rate, *Mater. Des.* 199 (2021).
- [16] Y.-X. Sang, M.-Z. Xiao, Z.-J. Zhang, Q.-Y. Fu, Effect of auxiliary heating process on low power pulsed laser wire feeding deposition, *Mater. Des.* 218 (2022).
- [17] M. Bambach, I. Sizova, F. Silze, M. Schnick, Comparison of laser metal deposition of Inconel 718 from powder, hot and cold wire, *Procedia CIRP* 74 (2018) 206–209.
- [18] C. Ding, X. Cui, J. Jiao, P. Zhu, Effects of substrate preheating temperatures on the microstructure, properties, and residual stress of 12CrNi2 prepared by laser cladding deposition technique, *Materials (Basel)* 11 (12) (2018).

- [19] R. Mertens, S. Dadbakhsh, J. Van Humbeeck, J.-P. Kruth, Application of base plate preheating during selective laser melting, *Procedia CIRP* 74 (2018) 5–11.
- [20] D. Wu, D. Liu, F. Niu, Q. Miao, K. Zhao, B. Tang, G. Bi, G. Ma, Al–Cu alloy fabricated by novel laser-tungsten inert gas hybrid additive manufacturing, *Addit. Manuf.* 33 (2020).
- [21] M. Gong, Y. Meng, S. Zhang, Y. Zhang, X. Zeng, M. Gao, Laser-arc hybrid additive manufacturing of stainless steel with beam oscillation, *Addit. Manuf.* 33 (2020).
- [22] N. Kalentits, M.O.V. de Seijas, S. Griffiths, C. Leinenbach, R.E. Logé, 3D laser shock peening – a new method for improving fatigue properties of selective laser melted parts, *Addit. Manuf.* 33 (2020).
- [23] S. Asai, K.-s. Sassa, M. Tahashi, Crystal orientation of non-magnetic materials by imposition of a high magnetic field, *Sci. Technol. Adv. Mater.* 4 (5) (2003) 455–460.
- [24] R.F. Tournier, E. Beaugnon, Texturing by Cooling a Metallic Melt in a Magnetic Field, *Science and technology of advanced materials*, 2009, 014501.
- [25] Fundamentals of magnetic field effects, in: M. Yamaguchi, Y. Tanimoto (Eds.), *Magneto-Science: Magnetic Field Effects on Materials: Fundamentals and Applications*, Springer Berlin Heidelberg, Berlin, Heidelberg, 2006, pp. 1–40.
- [26] P.A. Davidson, Magnetohydrodynamics in materials processing, *Annu. Rev. Fluid Mech.* 31 (1) (1999) 273–300.
- [27] P. Gillon, Uses of intense d.c. magnetic fields in materials processing, *Mater. Sci. Eng., A* 287 (2) (2000) 146–152.
- [28] T.P. Hou, Z.H. Li, K.M. Wu, H.F. Lin, Y. Li, G.H. Zhang, W.M. Liu, Role of external magnetic fields in determining the thermodynamic properties of iron carbides in steel, *Acta Mater.* 167 (2019) 71–79.
- [29] J. Yan, T. Liu, M. Wang, J. Sun, S. Dong, L. Zhao, Q. Wang, Constitutional supercooling and corresponding microstructure transition triggered by high magnetic field gradient during directional solidification of Al–Fe eutectic alloy, *Mater. Char.* 188 (2022), 111920.
- [30] Y. He, F. Bu, Y. Wu, J. Zhang, D. Luo, Z. Bian, Q. Zhou, T. Liu, Q. Wang, J. Wang, H. Wang, J. Li, E. Beaugnon, Liquid state dependent solidification of a Co–B eutectic alloy under a high magnetic field, *J. Mater. Sci. Technol.* 116 (2022) 58–71.
- [31] D. Du, A. Dong, D. Shu, G. Zhu, B. Sun, X. Li, Microstructure and crystallization evolution of directionally solidified Al–Cu–Si alloys with the assistance of a static magnetic field, *Metall. Mater. Trans. S* 53 (8) (2022) 3166–3178.
- [32] D. Du, Y. Fautrelle, A. Dong, D. Shu, G. Zhu, B. Sun, H. Nguyen-Thi, Z. Ren, X. Li, In-situ fabrication of graded material with the application of a horizontal magnetic field during directional solidification, *Mater. Char.* 141 (2018) 423–432.
- [33] K. Zaïdat, N. Mangelinck-Noël, R. Moreau, Control of melt convection by a travelling magnetic field during the directional solidification of Al–Ni alloys, *Compt. Rendus Mec.* 335 (5) (2007) 330–335.
- [34] L. Luo, L. Luo, R.O. Ritchie, Y. Su, B. Wang, L. Wang, R. Chen, J. Guo, H. Fu, Optimizing the microstructures and mechanical properties of Al–Cu-based alloys with large solidification intervals by coupling travelling magnetic fields with sequential solidification, *J. Mater. Sci. Technol.* 61 (2021) 100–113.
- [35] E. Çadırlı, H. Kaya, D. Räßiger, S. Eckert, M. Gündüz, Effect of rotating magnetic field on the microstructures and physical properties of Al–Cu–Co ternary eutectic alloy, *J. Alloys Compd.* 647 (2015) 471–480.
- [36] Y.Z. Li, N. Mangelinck-Noël, G. Zimmermann, L. Sturz, H. Nguyen-Thi, Modification of the microstructure by rotating magnetic field during the solidification of Al-7 wt.% Si alloy under microgravity, *J. Alloys Compd.* 836 (2020), 155458.
- [37] T. Wang, C. Zou, Z. Chen, M. Li, W. Wang, R. Li, H. Kang, In situ synthesis of TiB₂ particulate reinforced copper matrix composite with a rotating magnetic field, *Mater. Des.* 65 (1980–2015) (2015) 280–288.
- [38] J. Zhou, W. Guo, D. He, Y. Huang, Z. Cai, L. Zhou, Z. Xing, H. Wang, Study on preparation and wear resistance of NiCrBSi-WC/Co composite coatings by pulsed magnetic field assisted supersonic plasma spraying, *Surf. Coatings. Technol.* 448 (2022), 128897.
- [39] Y. Wang, Z. Xing, Y. Huang, W. Guo, J. Kang, H. Wang, Z. Zhang, Effect of pulse magnetic field treatment on the hardness of 20Cr2Ni4A steel, *J. Magn. Magn. Mater.* 538 (2021), 168248.
- [40] J.C. Jie, S.P. Yue, J. Liu, D.H. StJohn, Y.B. Zhang, E.Y. Guo, T.M. Wang, T.J. Li, Revealing the mechanisms for the nucleation and formation of equiaxed grains in commercial purity aluminum by fluid-solid coupling induced by a pulsed magnetic field, *Acta Mater.* 208 (2021), 116747.
- [41] S. Asai, Electromagnetic Processing of Materials, 2012.
- [42] Y. Fautrelle, Solidification Processing of Metallic Alloys under External Fields, 2018.
- [43] H. Ge, H. Fang, C. Zhang, L. Wang, Q. Zhang, J. Yao, The evolution of element distribution during laser cladding under static magnetic field, *Metall. Mater. Trans.* 53 (2) (2021) 370–376.
- [44] D. Du, L. Wang, A. Dong, W. Yan, G. Zhu, B. Sun, Promoting the densification and grain refinement with assistance of static magnetic field in laser powder bed fusion, *Int. J. Mach. Tool Manufact.* 183 (2022).
- [45] D. Du, J.C. Haley, A. Dong, Y. Fautrelle, D. Shu, G. Zhu, X. Li, B. Sun, E. J. Lavernia, Influence of static magnetic field on microstructure and mechanical behavior of selective laser melted AlSi10Mg alloy, *Mater. Des.* 181 (2019).
- [46] N. Kang, H. Yuan, P. Coddet, Z. Ren, C. Bernage, H. Liao, C. Coddet, On the texture, phase and tensile properties of commercially pure Ti produced via selective laser melting assisted by static magnetic field, *Mater. Sci. Eng. C* 70 (2017) 405–407.
- [47] H. Zhou, C. Song, Y. Yang, C. Han, M. Wang, Y. Xiao, Z. Liu, The microstructure and properties evolution of SS316L fabricated by magnetic field-assisted laser powder bed fusion, *Mater. Sci. Eng., A* 845 (2022).
- [48] D. Du, A. Dong, D. Shu, D. Wang, G. Zhu, B. Sun, E.J. Lavernia, Influence of static magnetic field on the microstructure of nickel-based superalloy by laser-directed energy deposition, *Metall. Mater. Trans. S* 51 (7) (2020) 3354–3359.
- [49] R. Zhao, C. Chen, S. Shuai, T. Hu, Y. Fautrelle, H. Liao, J. Lu, J. Wang, Z. Ren, Enhanced mechanical properties of Ti6Al4V alloy fabricated by laser additive manufacturing under static magnetic field, *Materials Research Letters* 10 (8) (2022) 530–538.
- [50] A.M. Filimonov, O.A. Rogozin, O.N. Dubinin, Y.O. Kuzminova, A.A. Shibalova, I. V. Okulov, I.S. Akhatov, S.A. Evlashin, Modification of mechanical properties in directed energy deposition by a static magnetic field: experimental and theoretical analysis, *Materials* 14 (18) (2021).
- [51] X. Zhou, Simulation of heat and mass transfer in arc welding based additive forming process with external transverse magnetic field, *J. Mech. Eng.* 54 (12) (2018).
- [52] Y. Wang, X. Chen, Q. Shen, C. Su, Y. Zhang, S. Jayalakshmi, R.A. Singh, Effect of magnetic Field on the microstructure and mechanical properties of inconel 625 superalloy fabricated by wire arc additive manufacturing, *J. Manuf. Process.* 64 (2021) 10–19.
- [53] P.-c. Huan, X. Wei, X.-n. Wang, H.-s. Di, Y. Chen, Q.-y. Zhang, X.-m. Chen, X.-j. Shen, Comparative study on the microstructure, mechanical properties and fracture mechanism of wire arc additive manufactured Inconel 718 alloy under the assistance of alternating magnetic field, *Mater. Sci. Eng., A* 854 (2022).
- [54] B. Wu, Z. Qiu, B. Dong, D. Wexler, Z. Pan, K. Carpenter, D.R. Corradi, H. Li, Effects of synchronized magnetic arc oscillation on microstructure, texture, grain boundary and mechanical properties of wire arc additively manufactured Ti6Al4V alloy, *Addit. Manuf.* 54 (2022).
- [55] A. Seidel, L. Degener, J. Schneider, F. Brueckner, E. Beyer, C. Leyens, Novel approach for suppressing of hot cracking via magneto-fluid dynamic modification of the laser-induced Marangoni convection, *Superalloys 2020/2020*, pp. 972–981.
- [56] Y. Wang, J. Chen, X. Wu, M. Chen, H. Su, L. Wang, C. Wu, Investigation on high-deposition-rate directed energy deposition of Al-5%Mg alloy via external compound magnetic fields, *Addit. Manuf.* 61 (2023), 103299.
- [57] M. Xia, D. Gu, G. Yu, D. Dai, H. Chen, Q. Shi, Porosity evolution and its thermodynamic mechanism of randomly packed powder-bed during selective laser melting of Inconel 718 alloy, *Int. J. Mach. Tool Manufact.* 116 (2017) 96–106.
- [58] R. Cunningham, C. Zhao, N. Parab, C. Kantzios, J. Pauza, K. Fezzaa, T. Sun, A. D. Rollett, Keyhole threshold and morphology in laser melting revealed by ultrahigh-speed x-ray imaging, *Science* 363 (6429) (2019) 849–852.
- [59] C. Zhao, N.D. Parab, X. Li, K. Fezzaa, W. Tan, A.D. Rollett, T. Sun, Critical instability at moving keyhole tip generates porosity in laser melting, *Science* 370 (6520) (2020) 1080–1086.
- [60] C.L.A. Leung, S. Marussi, R.C. Atwood, M. Towrie, P.J. Withers, P.D. Lee, In situ X-ray imaging of defect and molten pool dynamics in laser additive manufacturing, *Nat. Commun.* 9 (1) (2018) 1355.
- [61] S.J. Wolff, B. Gould, N. Parab, C. Zhao, A. Greco, T. Sun, Preliminary study on the influence of an external magnetic field on melt pool behavior in laser melting of 4140 steel using in-situ X-ray imaging, *J. Micro Nano-Manufacturing* 8 (4) (2021).
- [62] P.H. Smith, J.W. Murray, A. Jackson-Crisp, J. Segal, A.T. Clare, Magnetic manipulation in directed energy deposition using a programmable solenoid, *J. Mater. Process. Technol.* 299 (2022).
- [63] H.L. Wei, T. Mukherjee, W. Zhang, J.S. Zuback, G.L. Knapp, A. De, T. DebRoy, Mechanistic models for additive manufacturing of metallic components, *Prog. Mater. Sci.* 116 (2021), 100703.
- [64] D. Svetlizky, M. Das, B. Zheng, A.L. Vyatskikh, S. Bose, A. Bandyopadhyay, J. M. Schoenung, E.J. Lavernia, N. Eliaz, Directed energy deposition (DED) additive manufacturing: physical characteristics, defects, challenges and applications, *Mater. Today* 49 (2021) 271–295.
- [65] E. Alabot, Y.T. Tang, D. Barba, R.C. Reed, Alloys-by-design: a low-modulus titanium alloy for additively manufactured biomedical implants, *Acta Mater.* 229 (2022), 117749.
- [66] Y.T. Tang, C. Panwasawas, J.N. Ghoussooub, Y. Gong, J.W.G. Clark, A.A. Németh, D.G. McCartney, R.C. Reed, Alloys-by-design: application to new superalloys for additive manufacturing, *Acta Mater.* 202 (2021) 417–436.
- [67] Y. Liu, J. Zhang, Q. Tan, Y. Yin, S. Liu, M. Li, M. Li, Q. Liu, Y. Zhou, T. Wu, F. Wang, M.-X. Zhang, Additive manufacturing of high strength copper alloy with heterogeneous grain structure through laser powder bed fusion, *Acta Mater.* 220 (2021), 117311.
- [68] J.H. Martin, B.D. Yahata, J.M. Hundley, J.A. Mayer, T.A. Schaefler, T.M. Pollock, 3D printing of high-strength aluminium alloys, *Nature* 549 (7672) (2017) 365–369.
- [69] S. Yang, Q. Han, Y. Yin, J. Gao, Z. Zhang, Y. Gu, K.W.Q. Low, Effects of micrometer-sized TiB₂ on crack mitigation, mechanical and electrochemical performance of a Ni-based alloy fabricated by selective laser melting, *Opt. Laser. Technol.* 142 (2021), 107240.
- [70] W. Zhou, Y. Tian, Q. Tan, S. Qiao, H. Luo, G. Zhu, D. Shu, B. Sun, Effect of carbon content on the microstructure, tensile properties and cracking susceptibility of IN738 superalloy processed by laser powder bed fusion, *Addit. Manuf.* 58 (2022), 103016.
- [71] P.H. Smith, J.W. Murray, D.O. Jones, J. Segal, A.T. Clare, Magnetically assisted directed energy deposition, *J. Mater. Process. Technol.* 288 (2021).

- [72] C.J. Todaro, M.A. Easton, D. Qiu, D. Zhang, M.J. Birmingham, E.W. Lui, M. Brandt, D.H. StJohn, M. Qian, Grain structure control during metal 3D printing by high-intensity ultrasound, *Nat. Commun.* 11 (1) (2020) 142.
- [73] Y. Chen, M. Xu, T. Zhang, J. Xie, K. Wei, S. Wang, L. Yin, P. He, Grain refinement and mechanical properties improvement of Inconel 625 alloy fabricated by ultrasonic-assisted wire and arc additive manufacturing, *J. Alloys Compd.* 910 (2022).
- [74] D. Yuan, S. Shao, C. Guo, F. Jiang, J. Wang, Grain refining of Ti-6Al-4V alloy fabricated by laser and wire additive manufacturing assisted with ultrasonic vibration, *Ultrason. Sonochem.* 73 (2021), 105472.
- [75] D. Yuan, X. Sun, L. Sun, Z. Zhang, C. Guo, J. Wang, F. Jiang, Improvement of the grain structure and mechanical properties of austenitic stainless steel fabricated by laser and wire additive manufacturing assisted with ultrasonic vibration, *Mater. Sci. Eng., A* 813 (2021).
- [76] W. Cong, F. Ning, A fundamental investigation on ultrasonic vibration-assisted laser engineered net shaping of stainless steel, *Int. J. Mach. Tool Manufact.* 121 (2017) 61–69.
- [77] T. Wang, V. Mazánová, X. Liu, Ultrasonic effects on gas tungsten arc based wire additive manufacturing of aluminum matrix nanocomposite, *Mater. Des.* 214 (2022).
- [78] F. Ji, X. Qin, Z. Hu, X. Xiong, M. Ni, M. Wu, Influence of ultrasonic vibration on molten pool behavior and deposition layer forming morphology for wire and arc additive manufacturing, *Int. Commun. Heat Mass Tran.* 130 (2022).
- [79] G.I. Eskin, Ultrasonic Treatment of Light Alloy Melts, 1998.
- [80] L. Zhu, Z. Yang, B. Xin, S. Wang, G. Meng, J. Ning, P. Xue, Microstructure and mechanical properties of parts formed by ultrasonic vibration-assisted laser cladding of Inconel 718, *Surf. Coating. Technol.* 410 (2021).
- [81] Z. Yang, S. Wang, L. Zhu, J. Ning, B. Xin, Y. Dun, W. Yan, Manipulating molten pool dynamics during metal 3D printing by ultrasound, *Appl. Phys. Rev.* 9 (2) (2022).
- [82] F. Ning, W. Cong, Microstructures and mechanical properties of Fe-Cr stainless steel parts fabricated by ultrasonic vibration-assisted laser engineered net shaping process, *Mater. Lett.* 179 (2016) 61–64.
- [83] C.J. Todaro, M.A. Easton, D. Qiu, M. Brandt, D.H. StJohn, M. Qian, Grain refinement of stainless steel in ultrasound-assisted additive manufacturing, *Addit. Manuf.* 37 (2021).
- [84] F. Ning, Y. Hu, W. Cong, Microstructure and mechanical property of TiB reinforced Ti matrix composites fabricated by ultrasonic vibration-assisted laser engineered net shaping, *Rapid Prototyp. J.* 25 (3) (2019) 581–591.
- [85] F. Wang, D. Eskin, J. Mi, C. Wang, B. Koe, A. King, C. Reinhard, T. Connolley, A synchrotron X-ray diffraction study of the fragmentation and refinement of primary intermetallic particles in an Al-35 Cu alloy induced by ultrasonic melt processing, *Acta Mater.* 141 (2017) 142–153.
- [86] F. Wang, I. Tzanakis, D. Eskin, J. Mi, T. Connolley, In situ observation of ultrasonic cavitation-induced fragmentation of the primary crystals formed in Al alloys, *Ultrason. Sonochem.* 39 (2017) 66–76.
- [87] H. Wang, Y. Hu, F. Ning, W. Cong, Ultrasonic vibration-assisted laser engineered net shaping of Inconel 718 parts: effects of ultrasonic frequency on microstructural and mechanical properties, *J. Mater. Process. Technol.* 276 (2020).
- [88] Y. Zhang, Y. Guo, Y. Chen, Y. Cao, H. Qi, S. Yang, Microstructure and mechanical properties of Al-12Si alloys fabricated by ultrasonic-assisted laser metal deposition, *Materials (Basel)* 13 (1) (2019).
- [89] F. Ning, D. Jiang, Z. Liu, H. Wang, W. Cong, Ultrasonic frequency effects on the melt pool formation, porosity, and thermal-dependent property of inconel 718 fabricated by ultrasonic vibration-assisted directed energy deposition, *J. Manuf. Sci. Eng.* 143 (5) (2021).
- [90] J. Su, F. Jiang, J. Li, C. Tan, Z. Xu, H. Xie, J. Liu, J. Tang, D. Fu, H. Zhang, J. Teng, Phase Transformation Mechanisms, Microstructural Characteristics and Mechanical Performances of an Additively Manufactured Ti-6Al-4V Alloy under Dual-Stage Heat Treatment, *Materials & Design*, 2022.
- [91] Y. Zhao, Z. Ma, L. Yu, J. Dong, Y. Liu, The simultaneous improvements of strength and ductility in additive manufactured Ni-based superalloy via controlling cellular subgrain microstructure, *J. Mater. Sci. Technol.* 68 (2021) 184–190.
- [92] J. Su, J. Teng, Z. Xu, Y. Li, Effects of hydroxyapatite content on mechanical properties and in-vitro corrosion behavior of ZK60/HA composites, *Int. J. Mater. Res.* 111 (8) (2020) 621–631.
- [93] J. Su, J. Teng, Recent progress in graphene-reinforced aluminum matrix composites, *Front. Mater. Sci.* 15 (1) (2021) 79–97.
- [94] D. Wu, C. Song, T. Di, F. Niu, G. Ma, Intermetallic regulation mechanism of inconel 718/Ti6Al4V composite by novel follow-up ultrasonic assisted laser additive manufacturing, *Compos. B Eng.* 235 (2022).
- [95] S. Webster, H. Lin, F.M. Carter III, K. Ehmann, J. Cao, Physical mechanisms in hybrid additive manufacturing: a process design framework, *J. Mater. Process. Technol.* 291 (2021).
- [96] C. Wang, W. Suder, J. Ding, S. Williams, Wire based plasma arc and laser hybrid additive manufacture of Ti-6Al-4V, *J. Mater. Process. Technol.* 293 (2021).
- [97] T. Heeling, K. Wegener, The effect of multi-beam strategies on selective laser melting of stainless steel 316L, *Addit. Manuf.* 22 (2018) 334–342.
- [98] W. Fan, H. Tan, X. Lin, W. Huang, Microstructure formation of Ti-6Al-4 V in synchronous induction assisted laser deposition, *Mater. Des.* 160 (2018) 1096–1105.
- [99] W. Fan, H. Tan, F. Zhang, Z. Feng, Y. Wang, L.-C. Zhang, X. Lin, W. Huang, Overcoming the limitation of in-situ microstructural control in laser additive manufactured Ti-6Al-4V alloy to enhanced mechanical performance by integration of synchronous induction heating, *J. Mater. Sci. Technol.* 94 (2021) 32–46.
- [100] J.D. Roehling, W.L. Smith, T.T. Roehling, B. Vrancken, G.M. Guss, J.T. McKeown, M.R. Hill, M.J. Matthews, Reducing residual stress by selective large-area diode surface heating during laser powder bed fusion additive manufacturing, *Addit. Manuf.* 28 (2019) 228–235.
- [101] W.L. Smith, J.D. Roehling, M. Strantza, R.K. Ganeriwala, A.S. Ashby, B. Vrancken, B. Clausen, G.M. Guss, D.W. Brown, J.T. McKeown, M.R. Hill, M.J. Matthews, Residual stress analysis of in situ surface layer heating effects on laser powder bed fusion of 316L stainless steel, *Addit. Manuf.* 47 (2021).
- [102] D.-S. Shim, G.-Y. Baek, E.-M. Lee, Effect of substrate preheating by induction heater on direct energy deposition of AISI M4 powder, *Mater. Sci. Eng., A* 682 (2017) 550–562.
- [103] M.T. Dalaei, L. Gloor, C. Leinenbach, K. Wegener, Experimental and numerical study of the influence of induction heating process on build rates Induction Heating-assisted laser Direct Metal Deposition (IH-DMD), *Surf. Coating. Technol.* 384 (2020).
- [104] N. Naksuk, P. Poolperm, J. Nakngoenthong, W. Printrakoon, R. Yuttawiriya, Experimental investigation of hot-wire laser deposition for the additive manufacturing of titanium parts, *Mater. Res. Express* 9 (5) (2022).
- [105] Z. Lin, K. Song, X. Yu, A review on wire and arc additive manufacturing of titanium alloy, *J. Manuf. Process.* 70 (2021) 24–45.
- [106] Z. Nie, G. Wang, J.D. McGuffin-Cawley, B. Narayanan, S. Zhang, D. Schwam, M. Kottman, Y. Rong, Experimental study and modeling of H13 steel deposition using laser hot-wire additive manufacturing, *J. Mater. Process. Technol.* 235 (2016) 171–186.
- [107] M.P. Sealy, G. Madireddy, R.E. Williams, P. Rao, M. Toursangasarak, Hybrid processes in additive manufacturing, *J. Manuf. Sci. Eng.* 140 (6) (2018).
- [108] W. Fan, H. Tan, X. Lin, W. Huang, Thermal analysis of synchronous induction-assisted laser deposition of Ti-6Al-4V using different laser-induction interaction modes, *Addit. Manuf.* 35 (2020).
- [109] Y.N. Liu, E. Kannatey-Asibu, Laser beam welding with simultaneous Gaussian laser preheating, *J. Heat Tran.* 115 (1) (1993) 34–41.
- [110] E.S. Ng, I.A. Watson, Post-Heat Treatment of Nd: YAG Laser Welded High Carbon Steels, International Congress on Applications of Lasers & Electro-Optics, Laser Institute of America, 1997, pp. G238–G247.
- [111] K. Kempen, B. Vrancken, S. Buls, L. Thijss, J. Van Humbeeck, J.-P. Kruth, Selective laser melting of crack-free high density M2 high speed steel parts by baseplate preheating, *J. Manuf. Sci. Eng.* 136 (6) (2014).
- [112] A.C. Field, L.N. Carter, N.J.E. Adkins, M.M. Attallah, M.J. Gorley, M. Strangwood, The effect of powder characteristics on build quality of high-purity tungsten produced via laser powder bed fusion (LPBF), *Metall. Mater. Trans.* 51 (3) (2020) 1367–1378.
- [113] A. Iveković, N. Omidvari, B. Vrancken, K. Lietaert, L. Thijss, K. Vanmeensel, J. Vleugels, J.-P. Kruth, Selective laser melting of tungsten and tungsten alloys, *Int. J. Refract. Metals Hard Mater.* 72 (2018) 27–32.
- [114] A.V. Müller, G. Schlick, R. Neu, C. Anstätt, T. Klimkait, J. Lee, B. Pascher, M. Schmitt, C. Seidel, Additive manufacturing of pure tungsten by means of selective laser beam melting with substrate preheating temperatures up to 1000°C, *Nuclear Materials and Energy* 19 (2019) 184–188.
- [115] J. Xu, X. Lin, P. Guo, Y. Hu, X. Wen, L. Xue, J. Liu, W. Huang, The effect of preheating on microstructure and mechanical properties of laser solid forming IN-738LC alloy, *Mater. Sci. Eng., A* 691 (2017) 71–80.
- [116] M.M. Savalani, J.M. Pizarro, Effect of preheat and layer thickness on selective laser melting (SLM) of magnesium, *Rapid Prototyp. J.* 22 (1) (2016) 115–122.
- [117] X. Bai, H. Zhang, G. Wang, Modeling of the moving induction heating used as secondary heat source in weld-based additive manufacturing, *Int. J. Adv. Des. Manuf. Technol.* 77 (1–4) (2014) 717–727.
- [118] H. Ali, L. Ma, H. Ghadbeigi, K. Mumtaz, In-situ residual stress reduction, martensitic decomposition and mechanical properties enhancement through high temperature powder bed pre-heating of Selective Laser Melted Ti6Al4V, *Mater. Sci. Eng., A* 695 (2017) 211–220.
- [119] J.X. Fang, S.B. Li, S.Y. Dong, Y.J. Wang, H.S. Huang, Y.L. Jiang, B. Liu, Effects of phase transition temperature and preheating on residual stress in multi-pass & multi-layer laser metal deposition, *J. Alloys Compd.* 792 (2019) 928–937.
- [120] M.J. Birmingham, D.H. StJohn, J. Krynen, S. Tedman-Jones, M.S. Dargusch, Promoting the columnar to equiaxed transition and grain refinement of titanium alloys during additive manufacturing, *Acta Mater.* 168 (2019) 261–274.
- [121] J. Su, C. Tan, F.L. Ng, F. Weng, L. Chen, F. Jiang, J. Teng, Y. Chew, Additive manufacturing of novel heterostructured martensite-austenite dual-phase steel through in-situ alloying, *Mater. Today Commun.* 33 (2022).
- [122] Z. Li, C. Liu, T. Xu, L. Ji, D. Wang, J. Lu, S. Ma, H. Fan, Reducing arc heat input and obtaining equiaxed grains by hot-wire method during arc additive manufacturing titanium alloy, *Mater. Sci. Eng., A* 742 (2019) 287–294.
- [123] B. Vrancken, S. Buls, J.P. Kruth, J.V. Humbeeck, Preheating of Selective Laser Melted Ti6Al4V: Microstructure and Mechanical Properties, Proceedings of the 13th World Conference on Titanium, Wiley Online Library, 2016, pp. 1269–1277.
- [124] H. Schwab, M. Bönisch, L. Giebelner, T. Gustmann, J. Eckert, U. Kühn, Processing of Ti-5553 with improved mechanical properties via an in-situ heat treatment combining selective laser melting and substrate plate heating, *Mater. Des.* 130 (2017) 83–89.
- [125] H. Deng, W. Qiu, L. Chen, S. Cao, Y. Wei, Z. Hu, X. Cui, J. Tang, Microstructure and mechanical property of Ti-5Al-5Mo-5V-3Cr-1Zr alloy fabricated by selective laser melting with a preheated substrate, *Adv. Eng. Mater.* 23 (9) (2021).

- [126] J. Su, F. Jiang, C. Tan, F. Weng, F.L. Ng, M.H. Goh, H. Xie, J. Liu, Y. Chew, J. Teng, Additive manufacturing of fine-grained high-strength titanium alloy via multi-eutectoid elements alloying, *Compos. B Eng.* 249 (2023).
- [127] G. Graf, N. Nouri, S. Dietrich, F. Zanger, V. Schulze, Dual-laser PBF-lb processing of a high-performance maraging tool steel FeNiCoMoVtAl, *Materials (Basel)* 14 (15) (2021).
- [128] J. Su, X. Ji, J. Liu, J. Teng, F. Jiang, D. Fu, H. Zhang, Revealing the decomposition mechanisms of dislocations and metastable α' phase and their effects on mechanical properties in a Ti-6Al-4V alloy, *J. Mater. Sci. Technol.* 107 (2022) 136–148.
- [129] P.A. Colegrove, J. Donoghue, F. Martina, J. Gu, P. Prangnell, J. Hönnige, Application of bulk deformation methods for microstructural and material property improvement and residual stress and distortion control in additively manufactured components, *Scripta Mater.* 135 (2017) 111–118.
- [130] P.A. Colegrove, H.E. Coules, J. Fairman, F. Martina, T. Kashoob, H. Mamash, L. D. Cozzolino, Microstructure and residual stress improvement in wire and arc additively manufactured parts through high-pressure rolling, *J. Mater. Process. Technol.* 213 (10) (2013) 1782–1791.
- [131] F. Martina, S.W. Williams, P.A. Colegrove, Improved Microstructure and Increased Mechanical Properties of Additive Manufacture Produces Ti-6Al-4V by Interpass Cold Rolling, Solid Freeform Fabrication Symposium, Austin, Texas, USA, 2013.
- [132] H. Zhang, X. Wang, G. Wang, Y. Zhang, Hybrid direct manufacturing method of metallic parts using deposition and micro continuous rolling, *Rapid Prototyp. J.* 19 (6) (2013) 387–394.
- [133] X. Tian, Y. Zhu, C.V.S. Lim, J. Williams, R. Boyer, X. Wu, K. Zhang, A. Huang, Isotropic and improved tensile properties of Ti-6Al-4V achieved by in-situ rolling in direct energy deposition, *Addit. Manuf.* 46 (2021).
- [134] H. Zhang, R. Wang, L. Liang, G. Wang, HDMR technology for the aircraft metal part, *Rapid Prototyp. J.* 22 (6) (2016) 857–863.
- [135] L. Neto, S. Williams, J. Ding, J. Hnnige, F. Martina, Mechanical Properties Enhancement of Additive Manufactured Ti-6Al-4V by Machine Hammer Peening, International Conference on Advanced Surface Enhancement, 2020.
- [136] K.P. Karunakaran, K. Sajan, K.P. Milind, In-situ Stress Relieving Process for Additive Manufacturing, 2018. India.
- [137] M.P. Sealy, G. Madireddy, R. Williams, P. Rao, M. Toursangsaraki, Hybrid processes in additive manufacturing, *J. Manuf. Sci. Eng.* (2017).
- [138] J. Lv, K. Luo, H. Lu, Z. Wang, J. Liu, J. Lu, Achieving High Strength and Ductility in Selective Laser Melting Ti-6Al-4V Alloy by Laser Shock Peening, 2021.
- [139] V.R. Duarte, T.A. Rodrigues, N. Schell, R.M. Miranda, J.P. Oliveira, T.G. Santos, Hot forging wire and arc additive manufacturing (HF-WAAM), *Addit. Manuf.* 35 (2020).
- [140] J. Gu, J. Ding, S.W. Williams, H. Gu, P. Ma, Y. Zhai, The effect of inter-layer cold working and post-deposition heat treatment on porosity in additively manufactured aluminum alloys, *J. Mater. Process. Technol.* 230 (2016) 26–34.
- [141] J. Gu, S. Yang, M. Gao, J. Bai, Y. Zhai, J. Ding, Micropore evolution in additively manufactured aluminum alloys under heat treatment and inter-layer rolling, *Mater. Des.* 186 (2020).
- [142] C. Xie, S. Wu, Y. Yu, H. Zhang, Y. Hu, M. Zhang, G. Wang, Defect-correlated fatigue resistance of additively manufactured Al-Mg4.5Mn alloy with in situ micro-rolling, *J. Mater. Process. Technol.* 291 (2021).
- [143] X. Fang, L. Zhang, G. Chen, K. Huang, F. Xue, L. Wang, J. Zhao, B. Lu, Microstructure evolution of wire-arc additively manufactured 2319 aluminum alloy with interlayer hammering, *Mater. Sci. Eng., A* 800 (2021).
- [144] F. Martina, M.J. Roy, B.A. Szost, S. Terzi, P.A. Colegrove, S.W. Williams, P. J. Withers, J. Meyer, M. Hofmann, Residual stress of as-deposited and rolled wire +arc additive manufacturing Ti-6Al-4V components, *Mater. Sci. Technol.* 32 (14) (2016) 1439–1448.
- [145] X. Zhao, Y. Wang, G. Wang, R. Li, H. Zhang, Effect of process parameters on stress and strain of hybrid deposition and micro-rolling, *Rapid Prototyp. J.* 28 (3) (2021) 490–504.
- [146] M.P. Sealy, G. Madireddy, C. Li, Y.B. Guo, Finite Element Modeling of Hybrid Additive Manufacturing by Laser Shock Peening, Solid Freeform Fabrication Symposium, Austin, Texas, USA, 2016.
- [147] N. Kalentics, E. Boillat, P. Peyre, C. Gorny, C. Kenel, C. Leinenbach, J. Jhabvala, R.E. Logé, 3D laser shock peening – a new method for the 3D control of residual stresses in selective laser melting, *Mater. Des.* 130 (2017) 350–356.
- [148] G. Madireddy, C. Li, J. Liu, M.P. Sealy, Modeling thermal and mechanical cancellation of residual stress from hybrid additive manufacturing by laser peening, *Nanotechnology and Precision Engineering* 2 (2) (2019) 49–60.
- [149] N. Kalentics, A. Burn, M. Cloots, R.E. Logé, 3D laser shock peening as a way to improve geometrical accuracy in selective laser melting, *Int. J. Adv. Des. Manuf. Technol.* 101 (5–8) (2019) 1247–1254.
- [150] J.R. Hönnige, P. Colegrove, S. Williams, Improvement of Microstructure and Mechanical Properties in Wire + Arc Additively Manufactured Ti-6Al-4V with Machine Hammer Peening, 9th International Conference on Materials for Advanced Technologies, 2017.
- [151] X. Xu, S. Ganguly, J. Ding, P. Dirisu, F. Martina, X. Liu, S.W. Williams, Improving mechanical properties of wire plus arc additively manufactured maraging steel through plastic deformation enhanced aging response, *Mater. Sci. Eng., A* 747 (2019) 111–118.
- [152] J. Gu, J. Ding, S.W. Williams, H. Gu, J. Bai, Y. Zhai, P. Ma, The strengthening effect of inter-layer cold working and post-deposition heat treatment on the additively manufactured Al-6.3Cu alloy, *Mater. Sci. Eng., A* 651 (2016) 18–26.
- [153] J. Donoghue, A.A. Antonysamy, F. Martina, P.A. Colegrove, S.W. Williams, P. Prangnell, The effectiveness of combining rolling deformation with Wire-Arc Additive Manufacture on β -grain refinement and texture modification in Ti-6Al-4V, *Mater. Char.* 114 (2016) 103–114.
- [154] Y. Hu, N. Ao, S. Wu, Y. Yu, H. Zhang, W. Qian, G. Guo, M. Zhang, G. Wang, Influence of in situ micro-rolling on the improved strength and ductility of hybrid additively manufactured metals, *Eng. Fract. Mech.* 253 (2021).
- [155] R. Sun, L. Li, Y. Zhu, W. Guo, P. Peng, B. Cong, J. Sun, Z. Che, B. Li, C.J.J.O. A. Guo, Compounds, Microstructure, Residual Stress and Tensile Properties Control of Wire-Arc Additive Manufactured 2319 Aluminum Alloy with Laser Shock Peening, 2018, S0925838818308508.
- [156] C. Li, Y. Tian, Y. Chen, P. Hodgson, X. Wu, Y. Zhu, A. Huang, Hierarchical layered and refined grain structure of Inconel 718 superalloy produced by rolling-assisted directed energy deposition, *Additive Manufacturing Letters* 1 (2021).
- [157] K. Cheng, M. Zhang, H. Song, X. Liu, Z. Fan, G. Wang, H. Zhang, Additive manufacturing of Ti-6Al-4V alloy by hybrid plasma-arc deposition and microrolling: grain morphology, microstructure, and tensile properties, *Sci. China Technol. Sci.* 65 (4) (2022) 849–857.
- [158] T. Zhang, H. Li, H. Gong, J. Ding, Y. Wu, C. Diao, X. Zhang, S. Williams, Hybrid wire - arc additive manufacture and effect of rolling process on microstructure and tensile properties of Inconel 718, *J. Mater. Process. Technol.* 299 (2022).
- [159] J. Lv, K. Luo, H. Lu, Z. Wang, J. Liu, J. Lu, Achieving high strength and ductility in selective laser melting Ti-6Al-4V alloy by laser shock peening, *J. Alloys Compd.* 899 (2022).
- [160] B.E. Carroll, T.A. Palmer, A.M. Beese, Anisotropic tensile behavior of Ti6Al4V components fabricated with directed energy deposition additive manufacturing, *Acta Mater.* 87 (2015) 309–320.
- [161] T. Vilardo, C. Colin, J.D. Bartout, As-fabricated and heat-treated microstructures of the Ti-6Al-4V alloy processed by selective laser melting, *Metall. Mater. Trans.* 42A (10) (2011) 3190–3199.
- [162] H. Zhang, R. Li, R. Wang, Y. Fu, X. Wang, G. Wang, S. Tang, Casting - Forging - Milling Composite Additive Manufacturing Technology, Solid Freeform Fabrication Symposium, Austin, Texas, USA, 2017.
- [163] J. Chi, Z. Cai, H. Zhang, H. Zhang, W. Guo, Z. Wan, G. Han, P. Peng, Z. Zeng, Combining manufacturing of titanium alloy through direct energy deposition and laser shock peening processes, *Mater. Des.* 203 (2021).
- [164] L. Mashigo, H. Müller, C. Gassmann, Comparison of the Mechanical Properties of Grade 5 and Grade 23 Ti6Al4V for Wire-Arc Additive Manufacturing, vol. 7, The Southern African Institute of Mining Metallurgy, 2021.
- [165] B. Wu, Z. Pan, D. Ding, C. Dominic, H. Li, Effects of heat accumulation on microstructure and mechanical properties of Ti6Al4V alloy deposited by wire arc additive manufacturing, *Addit. Manuf.* 23 (2018) 151–160.
- [166] H. Gong, K. Rafi, T. Starr, B. Stucker, The Effects of Processing Parameters on Defect Regularity in Ti-6Al-4V Parts Fabricated by Selective Laser Melting and Electron Beam Melting, 24th Annual International Solid Freeform Fabrication Symposium, 2013.
- [167] C. Qiu, G.A. Ravi, C. Dance, A. Ranson, S. Dilworth, M.M. Attallah, Fabrication of large Ti-6Al-4V structures by direct laser deposition, *J. Alloys Compd.* 629 (2015) 351–361.
- [168] P. Edwards, M. Ramulu, Fatigue performance evaluation of selective laser melted Ti-6Al-4V, *J. Materials Science Engineering, A. Structural Materials: Properties, Microstructure Processing* 598 (2014) 327–337.
- [169] B. Vrancken, L. Thijss, J.P. Kruth, Heat treatment of Ti6Al4V produced by selective laser melting: microstructure and mechanical properties, *J. Alloys Compd.: An Interdisciplinary Journal of Materials Science Solid-state Chemistry Physics* (2012) 541.
- [170] K. Galina, H. Joachim, Improvement of fatigue resistance and ductility of TiAl6V4 processed by selective laser melting, *J. Mater. Process. Technol.* (2015).
- [171] W. Guo, R. Sun, B. Song, Y. Zhu, F. Li, Z. Che, B. Li, C. Guo, L. Liu, P. Peng, Laser shock peening of laser additive manufactured Ti6Al4V titanium alloy, *Surf. Coatings. Technol.* 349 (2018) 503–510.
- [172] J. Yu, M. Rombouts, G. Maes, F. Motmans, Material properties of Ti6Al4 V parts produced by laser metal deposition, *J. Physics Procedia* 39 (2012) 416–424.
- [173] H. Lu, L. Wu, H. Wei, J. Cai, K. Luo, X. Xu, J. Lu, Microstructural evolution and tensile property enhancement of remanufactured Ti6Al4V using hybrid manufacturing of laser directed energy deposition with laser shock peening, *Addit. Manuf.* 55 (2022).
- [174] C. Qiu, N.J. Adkins, M.M. Attallah, Microstructure and Tensile Properties of Selectively Laser-Melted and of HIPed Laser-Melted Ti-6Al-4V, *Materials Science & Engineering A*, 2013.
- [175] H.K. Rafi, N.V. Karthik, H. Gong, T.L. Starr, B.E. Stucker, Microstructures and mechanical properties of Ti6Al4V parts fabricated by selective laser melting and electron beam melting, *J. Mater. Eng. Perform.* 22 (12) (2013) 248.
- [176] J. Alcristo, A. Enriquez, H. García, S. Hinkson, T. Steelman, E. Silverman, P. Valdovino, H. Gigerenzer, J. Foyos, J. Ogren, Tensile properties and microstructures of laser-formed Ti-6Al-4V, *J. Mater. Eng. Perform.* 20 (2) (2011) 203–212.
- [177] T. Artaza, A. Suarez, F. Veiga, I. Braceras, A. Lamikiz, Wire arc additive manufacturing Ti6Al4V aeronautical parts using plasma arc welding: analysis of heat-treatment processes in different atmospheres, *J. Mater. Res. Technol.* 9 (6) (2020).
- [178] Y.N. Hu, S.C. Wu, P.J. Withers, J. Zhang, H.Y.X. Bao, Y.N. Fu, G.Z. Kang, The effect of manufacturing defects on the fatigue life of selective laser melted Ti-6Al-4V structures, *Mater. Des.* 192 (2020).
- [179] T.H. Becker, P. Kumar, U. Ramamurthy, Fracture and fatigue in additively manufactured metals, *Acta Mater.* 219 (33) (2021), 117240.

- [180] Q. Chen, G. Wang, H. Zhang, R. Li, Research on microstructure and mechanical properties of hybrid plasma arc and micro-rolling additive manufacturing of Inconel 718 superalloy, *Rapid Prototyp. J.* 28 (8) (2022) 1509–1519.
- [181] C. Ma, Y. Liu, C. Li, H. Dong, D. Li, X. Wu, P. Liu, Q. Sun, H. Jin, F. Zhang, Mechanical properties of carbon steel by compound arc and vibration shock forging-rolling, *J. Manuf. Process.* 60 (2020) 11–22.
- [182] T.J.G.d. Santos, R.M.M. Miranda, Developments in Directed Energy Deposition Additive Manufacturing-In Situ Hot Forging and Indirect Cooling, Nova school of science & technology, 2020.
- [183] J. Lu, H. Lu, X. Xu, J. Yao, J. Cai, K. Luo, High-performance integrated additive manufacturing with laser shock peening –induced microstructural evolution and improvement in mechanical properties of Ti6Al4V alloy components, *Int. J. Mach. Tool Manufact.* 148 (2020).
- [184] D.A. Gurnett, W.S. Kurth, Intense plasma waves at and near the solar wind termination shock, *Nature* 454 (7200) (2008) 78–80.
- [185] R.C. Fear, S.E. Milan, R. Maggiolo, A.N. Fazakerley, I. Dandouras, S.B. Mende, Direct observation of closed magnetic flux trapped in the high-latitude magnetosphere, *Science* 346 (6216) (2014) 1506–1510.
- [186] E.D. Kirson, Z. Gurvich, R. Schneiderman, E. Dekel, A. Itzhaki, Y. Wasserman, R. Schatzberger, Y. Palti, Disruption of cancer cell replication by alternating electric fields, *Cancer Res.* 64 (9) (2004) 3288–3295.
- [187] Y. Lu, G. Sun, Z. Wang, Y. Zhang, B. Su, A. Feng, Z. Ni, Effects of electromagnetic field on the laser direct metal deposition of austenitic stainless steel, *Opt. Laser. Technol.* 119 (2019).
- [188] Y. Huang, Y. Cao, H. Qin, Electric field assisted direct writing and 3D printing of low-melting alloy, *Adv. Eng. Mater.* 24 (9) (2022).
- [189] H. Yoon, P. Liu, Y. Park, G. Choi, P.P. Choi, H. Sohn, Pulsed laser-assisted additive manufacturing of Ti-6Al-4V for in-situ grain refinement, *Sci. Rep.* 12 (1) (2022), 22247.
- [190] G. Ma, X. Liu, C. Song, F. Niu, D. Wu, TiCp reinforced Ti6Al4V of follow-up synchronous electromagnetic induction-laser hybrid directed energy deposition: microstructure evolution and mechanical properties, *Addit. Manuf.* 59 (2022).
- [191] T. DebRoy, T. Mukherjee, H.L. Wei, J.W. Elmer, J.O. Milewski, Metallurgy, mechanistic models and machine learning in metal printing, *Nat. Rev. Mater.* 6 (1) (2020) 48–68.
- [192] T. DebRoy, H.L. Wei, J.S. Zuback, T. Mukherjee, J.W. Elmer, J.O. Milewski, A. M. Beese, A. Wilson-Heid, A. De, W. Zhang, Additive manufacturing of metallic components – process, structure and properties, *Prog. Mater. Sci.* 92 (2018) 112–224.
- [193] H.L. Wei, T. Mukherjee, W. Zhang, J.S. Zuback, G.L. Knapp, A. De, T. DebRoy, Mechanistic models for additive manufacturing of metallic components, *Prog. Mater. Sci.* 116 (2021).
- [194] P. Zagade, B.P. Gautham, A. De, T. DebRoy, Analytical estimation of fusion zone dimensions and cooling rates in part scale laser powder bed fusion, *Addit. Manuf.* 46 (2021).
- [195] T. Mukherjee, V. Manvatkar, A. De, T. DebRoy, Dimensionless numbers in additive manufacturing, *J. Appl. Phys.* 121 (6) (2017).
- [196] T. DebRoy, S.A. David, Physical processes in fusion welding, *Rev. Mod. Phys.* 67 (1) (1995) 85–112.
- [197] A. Raghavan, H.L. Wei, T.A. Palmer, T. DebRoy, Heat transfer and fluid flow in additive manufacturing, *J. Laser Appl.* 25 (5) (2013).
- [198] L. Chen, H. Li, S. Liu, S. Shen, T. Zhang, Y. Huang, G. Zhang, Y. Zhang, B. He, C. Yang, Simulation of surface deformation control during selective laser melting of AlSi10Mg powder using an external magnetic field, *AIP Adv.* 9 (4) (2019).
- [199] L. Wang, W. Yan, Thermo-electric magnetohydrodynamic model for laser-based metal additive manufacturing, *Phys. Rev. Appl.* 15 (6) (2021).
- [200] H.L. Wei, J.W. Elmer, T. DebRoy, Three-dimensional modeling of grain structure evolution during welding of an aluminum alloy, *Acta Mater.* 126 (2017) 413–425.
- [201] H.L. Wei, J.W. Elmer, T. DebRoy, Crystal growth during keyhole mode laser welding, *Acta Mater.* 133 (2017) 10–20.
- [202] Y. Du, T. Mukherjee, T. DebRoy, Physics-informed machine learning and mechanistic modeling of additive manufacturing to reduce defects, *Appl. Mater. Today* 24 (2021).
- [203] M. Jiang, T. Mukherjee, Y. Du, T. DebRoy, Superior printed parts using history and augmented machine learning, *npj Comput. Mater.* 8 (1) (2022).
- [204] Y. Du, T. Mukherjee, N. Finch, A. De, T. DebRoy, High-throughput screening of surface roughness during additive manufacturing, *J. Manuf. Process.* 81 (2022) 65–77.
- [205] X. Chen, N. Jiang, M. Jiang, Y. Du, S. Ma, Y. Chen, C. Tan, Z. Lei, S. Zhao, Y. Chen, Numerical investigation of asymmetric weld fusion geometry in laser welding of aluminium alloy with beam oscillation, *Sci. Technol. Weld. Join.* 27 (8) (2022) 595–605.
- [206] L. Wang, J. Yao, Y. Hu, S. Song, Suppression effect of a steady magnetic field on molten pool during laser remelting, *Appl. Surf. Sci.* 351 (2015) 794–802.
- [207] Y. Zhou, W. Qu, F. Zhou, X. Li, L. Song, Q. Zhu, Thermo-fluid flow behavior of the IN718 molten pool in the laser directed energy deposition process under magnetic field, *Rapid Prototyp. J.* (2022).
- [208] A. Kao, T. Gan, C. Tonry, I. Krastins, K. Pericleous, Thermoelectric magnetohydrodynamic control of melt pool dynamics and microstructure evolution in additive manufacturing, *Phil. Trans. Math. Phys. Eng. Sci.* 378 (2020) 2171.
- [209] X. Zhang, J. Kang, S. Wang, J. Ma, T. Huang, The effect of ultrasonic processing on solidification microstructure and heat transfer in stainless steel melt, *Ultrason. Sonochem.* 27 (2015) 307–315.
- [210] G. Wang, P. Croaker, M. Dargusch, D. McGuckin, D. StJohn, Simulation of convective flow and thermal conditions during ultrasonic treatment of an Al-2Cu alloy, *Comput. Mater. Sci.* 134 (2017) 116–125.
- [211] P. Promoppatum, Dual-laser powder bed fusion additive manufacturing: computational study of the effect of process strategies on thermal and residual stress formations, *Int. J. Adv. Des. Manuf. Technol.* 121 (1–2) (2022) 1337–1351.
- [212] W. Zhang, W.M. Abbott, A. Sasnauskas, R. Lupoi, Process parameters optimisation for mitigating residual stress in dual-laser beam powder bed fusion additive manufacturing, *Metals* 12 (3) (2022).
- [213] W. Zhang, M. Tong, N.M. Harrison, Scanning strategies effect on temperature, residual stress and deformation by multi-laser beam powder bed fusion manufacturing, *Addit. Manuf.* 36 (2020), 101507.
- [214] R. Evans, J. Gockel, Modeling the effects of coordinated multi-beam additive manufacturing, *Int. J. Adv. Des. Manuf. Technol.* 115 (4) (2021) 1075–1087.
- [215] G.-G. Xu, W.-G. Jiang, Y.-Y. Sun, Q.-H. Qin, Q. Li, Particle-scale computational fluid dynamics simulation on selective parallel dual-laser melting of nickel-based superalloy, *J. Manuf. Process.* 73 (2022) 197–206.
- [216] L. Cao, Numerical investigation on molten pool dynamics during multi-laser array powder bed fusion process, *Metall. Mater. Trans.* 52 (2021) 211–227.
- [217] B. Liu, B.-Q. Li, Z. Li, P. Bai, Y. Wang, Z. Kuai, Numerical investigation on heat transfer of multi-laser processing during selective laser melting of AlSi10Mg, *Results Phys.* 12 (2019) 454–459.
- [218] J. Xiong, Y. Lei, R. Li, Finite element analysis and experimental validation of thermal behavior for thin-walled parts in GMAW-based additive manufacturing with various substrate preheating temperatures, *Appl. Therm. Eng.* 126 (2017) 43–52.
- [219] G.M.M.P. Sealy, C. Li, Y.B. Guo, Finite Element Modeling of Hybrid Additive Manufacturing by Laser Shock Peening, 2016 International Solid Freeform Fabrication Symposium, University of Texas at Austin, 2016.
- [220] X. Zhou, H. Zhang, G. Wang, X. Bai, Y. Fu, J. Zhao, Simulation of microstructure evolution during hybrid deposition and micro-rolling process, *J. Mater. Sci.* 51 (14) (2016) 6735–6749.
- [221] X. Jin, L. Lan, S. Gao, B. He, Y. Rong, Effects of laser shock peening on microstructure and fatigue behavior of Ti-6Al-4V alloy fabricated via electron beam melting, *Mater. Sci. Eng., A* 780 (2020).
- [222] V. Gorniyakov, J. Ding, Y. Sun, S. Williams, Understanding and designing post-build rolling for mitigation of residual stress and distortion in wire arc additively manufactured components, *Mater. Des.* 213 (2022).
- [223] V. Gorniyakov, Y. Sun, J. Ding, S. Williams, Efficient determination and evaluation of steady-state thermal-mechanical variables generated by wire arc additive manufacturing and high pressure rolling, *Model. Simulat. Mater. Sci. Eng.* 30 (1) (2021).
- [224] M.A. Wells, I.V. Samarasekera, J.K. Brimacombe, E.B. Hawbolt, D.J. Lloyd, Modeling the microstructural changes during hot tandem rolling of AA5XXX aluminum alloys: Part III. Overall model development and validation, *Mater. Trans. B* 29 (3) (1998) 709–719.
- [225] M. Tolouei, S. Serajzadeh, Modelling recrystallization kinetics during hot rolling of AA5083, *J. Mater. Process. Technol.* 184 (1–3) (2007) 345–353.
- [226] S.P. Jupp, Mathematical Modeling of the Microstructural Evolution during the Hot Rolling of AA5083 Aluminum Alloys, University of British Columbia, 2001.
- [227] O. Kalinina, A. Lyudagovsky, A. Loktev, V. Korolev, I. Shishkina, D. Alexandrova, P. Geluh, D. Loktev, Energy efficiency of temperature distribution in electromagnetic welding of rolling stock parts, *E3S Web of Conf.* 110 (2019).
- [228] K.J. Juul, K.L. Nielsen, C.F. Niordson, Steady-state numerical modeling of size effects in micron scale wire drawing, *J. Manuf. Process.* 25 (2017) 163–171.
- [229] C.J. Luis, J. León, R. Luri, Comparison between finite element method and analytical methods for studying wire drawing processes, *J. Mater. Process. Technol.* 164–165 (2005) 1218–1225.
- [230] M. Abbaszadeh, J.R. Hönnige, F. Martina, L. Neto, N. Kashaei, P. Colegrave, S. Williams, B. Klusemann, Numerical investigation of the effect of rolling on the localized stress and strain induction for wire + arc additive manufactured structures, *J. Mater. Eng. Perform.* 28 (8) (2019) 4931–4942.
- [231] G. Tapia, A. Elwany, A review on process monitoring and control in metal-based additive manufacturing, *J. Manuf. Sci. Eng.* 136 (6) (2014).
- [232] L. Aucott, H. Dong, W. Mirihanage, R. Atwood, A. Kidess, S. Gao, S. Wen, J. Marsden, S. Feng, M. Tong, Revealing internal flow behaviour in arc welding and additive manufacturing of metals, *Nat. Commun.* 9 (1) (2018) 5414.
- [233] B.J. Simonds, J. Sowards, J. Hadler, E. Pfeif, B. Wilthan, J. Tanner, C. Harris, P. Williams, J. Lehman, Time-resolved absorptance and melt pool dynamics during intense laser irradiation of a metal, *Phys. Rev. Appl.* 10 (4) (2018), 044061.
- [234] L. Levine, M. Stoudt, B. Lane, A Preview of the NIST/TMS Additive Manufacturing Benchmark Test and Conference Series, *JOM* (Warrendale, Pa., 2018, p. 70, 1989).
- [235] Q. Bian, X. Tang, R. Dai, M. Zeng, Evolution phenomena and surface shrink of the melt pool in an additive manufacturing process under magnetic field, *Int. J. Heat Mass Tran.* 123 (2018) 760–775.
- [236] C. Wang, Y. Sun, G. Chen, X. Chen, J. Ding, W. Suder, C. Diao, S. Williams, A simplified modelling approach for thermal behaviour analysis in hybrid plasma arc-laser additive manufacturing, *Int. J. Heat Mass Tran.* 195 (2022).
- [237] M. Tang, P.C. Pistorius, J.L. Beuth, Prediction of lack-of-fusion porosity for powder bed fusion, *Addit. Manuf.* 14 (2017) 39–48.
- [238] T. Mukherjee, H.L. Wei, A. De, T. DebRoy, Heat and fluid flow in additive manufacturing—Part I: modeling of powder bed fusion, *Comput. Mater. Sci.* 150 (2018) 304–313.

- [239] T. Mukherjee, H.L. Wei, A. De, T. DebRoy, Heat and fluid flow in additive manufacturing – Part II: powder bed fusion of stainless steel, and titanium, nickel and aluminum base alloys, *Comput. Mater. Sci.* 150 (2018) 369–380.
- [240] H.L. Wei, J.W. Elmer, T. DebRoy, Origin of grain orientation during solidification of an aluminum alloy, *Acta Mater.* 115 (2016) 123–131.
- [241] Q. Wu, T. Mukherjee, A. De, T. DebRoy, Residual stresses in wire-arc additive manufacturing – hierarchy of influential variables, *Addit. Manuf.* 35 (2020).
- [242] Q. Wu, T. Mukherjee, C. Liu, J. Lu, T. DebRoy, Residual stresses and distortion in the patterned printing of titanium and nickel alloys, *Addit. Manuf.* 29 (2019).
- [243] C. Li, Z.Y. Liu, X.Y. Fang, Y.B. Guo, Residual stress in metal additive manufacturing, *Procedia CIRP* 71 (2018) 348–353.
- [244] J. Zhou, H.L. Tsai, Modeling of transport phenomena in hybrid laser-MIG keyhole welding, *Int. J. Heat Mass Tran.* 51 (17–18) (2008) 4353–4366.
- [245] L. Singh, R.A. Khan, M.L. Aggarwal, Empirical modeling of shot peening parameters for welded austenitic stainless steel using grey relational analysis, *J. Mech. Sci. Technol.* 26 (6) (2012) 1731–1739.
- [246] G. Singh, R.V. Grandhi, D.S. Stargel, Modeling and parameter design of a laser shock peening process, *Int. J. Comput. Methods Eng. Sci. Mech.* 12 (5) (2011) 233–253.
- [247] X.W. Fang, H. Xiao, K. Marthinsen, A. Belyakov, X.Y. Fang, K. Huang, Tailoring microstructure and texture of annealed Al-Mn alloy through the variation of homogenization and prior cold deformation strain, *Mater. Char.* 166 (2020).
- [248] T.N. Lamichhane, L. Sethuraman, A. Dalagan, H. Wang, J. Keller, M. P. Paranthaman, Additive manufacturing of soft magnets for electrical machines—a review, *Mater. Today Phys.* 15 (2020).
- [249] C. Tan, Y. Liu, F. Weng, F.L. Ng, J. Su, Z. Xu, X.D. Ngai, Y. Chew, Additive manufacturing of voxelized heterostructured materials with hierarchical phases, *Addit. Manuf.* 54 (2022).
- [250] C. Tan, Q. Li, X. Yao, L. Chen, J. Su, F.L. Ng, Y. Liu, T. Yang, Y. Chew, C.T. Liu, T. DebRoy, Machine learning customized novel material for energy-efficient 4D printing, *Adv. Sci.* 10 (10) (2023), 2206607.
- [251] C. Panwisawas, Y.T. Tang, R.C. Reed, Metal 3D printing as a disruptive technology for superalloys, *Nat. Commun.* 11 (1) (2020) 1–4.
- [252] A. Bandyopadhyay, K.D. Traxel, M. Lang, M. Juhasz, N. Eliaz, S. Bose, Alloy design via additive manufacturing: advantages, challenges, applications and perspectives, *Mater. Today* (2022).
- [253] C. Tan, Y. Chew, F. Weng, S. Sui, Z. Du, F.L. Ng, G. Bi, Superior strength-ductility in laser aided additive manufactured high-strength steel by combination of intrinsic tempering and heat treatment, *Virtual Phys. Prototyp.* 16 (4) (2021) 460–480.
- [254] P. Kürnsteiner, M.B. Wilms, A. Weisheit, B. Gault, E.A. Jägle, D. Raabe, High-strength Damascus steel by additive manufacturing, *Nature* 582 (7813) (2020) 515–519.
- [255] A. Yadollahi, N. Shamsaei, S.M. Thompson, A. Elwany, L. Bian, Effects of building orientation and heat treatment on fatigue behavior of selective laser melted 17-4 PH stainless steel, *Int. J. Fatig.* 94 (2017) 218–235.
- [256] C. Tan, K. Zhou, W. Ma, P. Zhang, M. Liu, T. Kuang, Microstructural evolution, nanoprecipitation behavior and mechanical properties of selective laser melted high-performance grade 300 maraging steel, *Mater. Des.* 134 (2017) 23–34.